GUIDED MODE RESONANCE BASED SPECTROSCOPY FOR SENSING APPLICATIONS

GUIDED MODE RESONANCE BASED SPECTROSCOPY FOR SENSING APPLICATIONS

A Dissertation Presented to
The Graduate School of Bangkok University

In Partial Fulfilment
of the Requirements for the Degree
Doctor of Engineering in Electrical and Computer Engineering

by
Hironmay Deb
2021

This thesis has been approved by

School of Engineering

Bangkok University

Title: Guided Mode Resonance Based Spectroscopy for Sensing Applications

Author: Hironmay Deb

Thesis Committee:

Thesis Advisor _____

(Dr. Waleed Soliman Mohammed)

Thesis Co-advisor _____

(Dr. Sakoolkan Boonruang)

Graduate Program Director _____

(Asst.Prof.Dr.Chakkaphong Suthaputchakun)

External Representative _____

(Dr. Tanujjal Bora)

_____

(Asst.Prof.Dr. Wisarn Patchoo)

Dean of the School of Engineering

(____/____/____)

Deb, H., Doctoral in Engineering, in Electrical and Computer Engineering, December, 2021, Graduate School, Bangkok University

Guided Mode Resonance Based Spectroscopy for Sensing Applications

Advisor of Dissertation: Waleed Soliman Mohammed, Ph.D.

ABSTRACT

This thesis focuses on design and demonstration of read-out systems based on guided mode resonance for sensing applications. The work is divided into two main parts. The first study, theoretically and experimentally, demonstrates sensitivity enhancement in dielectric guided-mode resonance (GMR) sensor via controlling a super-mode resonance at nearly cut-off diffraction (or at Rayleigh wavelength). A bulk refractive index sensitivity can reach the upper limit at a value linearly proportional to the grating's periodicity. Super-mode excitation in the multilayer configuration of the 2D GMR sensor (a high index refractive index film coated on a low refractive index imprinted grating) is presented. This concept is verified using Rigorous Coupled Wave Analysis (RCWA). Modal allocation for each resonance in the GMR structure is performed using the four-layer waveguide. The measured super-mode resonance has shown sensitivity enhancement almost three folds of that of the traditional guide mode resonance. Also, this realization occurs in a broad dynamic range through optimization of the structure's parameters guarantees usage in multiple sensing applications.

In the second part, the study demonstrates design and development of an open-

source platform-based reflection spectroscopy readout system for guided mode resonance sensing applications. The GMR dimensions, reflection grating period, imaging system and components orientation are optimized to enhance the angular resolution while sustaining resonance excitation within the visible range. To achieve the needed arrangement of the multiple components, 3D printing is utilized to build the mechanical mounting. The reflection spectra are extracted from the webcam images and processed using software written on raspberry-pi computational unit. This ensures the compactness and portability of the system. The system performance of the transducer is tested by measuring the changes in the refractive index of the environment at the GMR chip interface.

Keywords: Guided mode resonance, Optical sensor, Refractive-index sensor, 3D printing, Open-source platform.

Keywords: Guided mode resonance, Optical sensor, Refractive-index sensor, 3D printing, Open-source platform.

Approved: _____

Signature of Advisor

ACKNOWLEDGEMENT

Foremost, I would like to express my sincere gratitude to my advisor, Dr. Waleed S. Mohammed and my co-advisor Dr. Sakoolkan Boonruang for their guidance and support during my studies in Bangkok University. I would like to thank, Dr. Romuald Jolivot for his suggestions and constant encouragement. I would also like to thank Dr. Chamras Promptmas for providing his support and guidance in performing my research work.

I would like to express my gratitude to NECTEC for providing me the facilities to perform research. I would also like to thank Nantarat Srisuai and Boonrasri Seeleang for teaching me the fabrication techniques and helping me with work at NECTEC.

I want to thank my family back in India for their never-ending emotional support which provided me courage and patience for doing work. I specially want to thank my wife, Nabanita Bhowmick Deb, who always encouraged me to follow my heart.

Finally, I would like to thank Bangkok University for providing me with fellowship and supporting me in completing my thesis.

TABLE OF CONTENTS vii

TABLE OF CONTENTS (Continued) viii

TABLE OF CONTENTS (Continued) ix

LIST OF TABLES x

LIST OF FIGURES xi

LIST OF FIGURES (Continued) xii

LIST OF FIGURES (Continued) xv

LIST OF FIGURES (Continued) xvi

CHAPTER 1

INTRODUCTION

With the developments in micro and nanofabrication methods along with economization and readily accessibility of such techniques, guided mode resonance (GMR) filters have established several applications. The resonance response in a GMR structure is extremely sensitive to refractive index (RI) variations in the proximity of the high index waveguide structure. This makes it a good candidate for sensing applications.

In literature, GMR structures have been demonstrated in many applications such as Strain sensors (Babu & Lee, 2019), biosensors (Magnusson et al., 2018), gas sensors (L. Wang et al., 2018), humidity sensors (Gryga et al., 2020) and displacement sensors (Y.-C. Wang & Huang, 2018). In all of these applications, the grating parameters has a significant role in setting the spectrum range of the GMR sensor operation. This varies from ultraviolet region, visible region (Dang et al., 2019), infrared region (J.-N. Liu et al., 2011) to Terahertz region (Bark & Jeon, 2018).

Resonance anomaly in a grating waveguide structure was first investigated by R. M Wood in 1902 (Wood, 1902). In an experiment, Wood noticed that when the grating was illuminated by a perpendicular polarized (P-polarized) light, relative to the grating grooves, the diffracted spectrum displayed swift intensity increase by many factors. The anomaly was referred to as Wood's anomaly as they did not follow the theory of diffraction. Many researchers attempted to explain Wood's anomaly.

In 1907, Lord Rayleigh analyzed Wood's anomalies in the grating structure and noticed that the appearance of a higher diffracted order outcomes in the reorganization of the total power in various diffraction orders (Strutt, 1907). The wavelengths at which such transition occurs are known as Rayleigh wavelengths. However, Fano in 1941, was able to differentiate between the two types of anomalies: a Rayleigh Type which showed a sharp anomaly or "edge" occurring at frequencies calculated by Rayleigh, and "diffuse" type that extended at lower frequencies from Rayleigh and consisted generally of a minimum and maximum intensity (Fano, 1941). This was the first phase in better understanding the resonant phenomena. Wood performed more research work and found the anomalies to exist when the electric field polarization was oriented perpendicular to the grating grooves (S-polarization) (Wood, 1912). In 1952, Palmer found that these anomalies would also occur when the field is oriented in parallel to the grooves (P-polarization). He found that the P anomalies disappear when the depth of the grating is much less than the wavelength (Palmer, 1952). Many of the theoretical research work between 1950 and 1960 focused on clarifying the anomalies. It was in 1965 when Hessel and Oliner presented a proper understanding of the Wood's anomalies based on guided wave approach rather than the scattering approach that had stood until then (Hessel & Oliner, 1965). They identified two mechanisms. The first is the well-recognized Rayleigh wavelength type and the second was a resonance phenomenon due to guided waves supported by the grating structure called "guided mode resonance." The anomaly was produced when the fields leaking from the grating structure interfered constructively due to phase matching.

In 1973, Nievere further extended Hessel and Oliner's work and investigated the resonance effect in non-metallic grating structures (Neviere et al., 1973a). He observed that the assemblies were able to display a resonance response for the angle of incidence into the grating structure for both S-polarized and P-polarized light (Neviere et al., 1973b). Several works as well were done to understand the efficiency of these guided mode resonances. Popov and Mastev in 1986 studied the diffraction efficiency of guided mode resonant waves (Popov et al., 1986). In 1990, Wang and Magnusson's studied the diffraction efficiency of subwavelength planar all-dielectric grating waveguides using rigorous coupled wave analysis (RCWA) (S. S. Wang et al., 1990). Wang and Magnusson's study was based on earlier analysis by Gaylord and Moharram (Gaylord & Moharam, 1985). It was their study that suggested the potential use of these structures for optical filtering applications. In the successive years, several research works were done on the application of guided mode resonance filters as sensors, tunable filters, and electro-optic switches (S. S. Wang & Magnusson, 1993a). The study of GMR was not only confined to the one-dimensional structure but it also extended to two dimensional (Peng & Morris, 1996) and three-dimensional structures (Fan & Joannopoulos, 2002).

A GMR assembly consists of a grating having subwavelength dimension and a waveguide, which may be parted or ingrained into one film. Resonance phenomenon happens when there is phase matching between diffracted waves and guided modes propagating inside the structure. The guided mode that is coupled by the subwavelength grating is re-radiated back through a constructive interference of the leakage from the

diffraction. A total reflection with highly spectral and angular selectively is obtained at resonance which is depicted as a peak reflection or dip transmission at the resonant wavelength.

The need for medical point-of-care instruments has demanded increased research for GMR biosensors towards lab-on-chip technology. Magnusson et. al first investigated the application of GMR principle in potential biosensing (Wawro et al., 2000) after which many groups such as Cunningham et al. (B. Cunningham et al., 2002), Sharon et al. (Sharon et al., 1997), and Liu at al. (Z. S. Liu et al., 1998) demonstrated the same concept. The successful transformation of lab-on-chip mechanization to point of care requires certain criteria to be fulfilled such as the good response of the sensor in real-time, compact size, minimal requirement of technical expertise, and low cost to be affordable for application in third world countries. For the compact device to be implemented in field application, sufficient sensitivity is required for practical use.

The wavelength at which resonance occurs depends on the optical properties of the material, structural dimensions, and angle of incidence. The sensitivity of the GMR sensor relies strongly on the resonance mode's confinement. Field enhancement in the sensing region of the GMR device has been much researched upon for increasing the sensitivity. However, the maximum normalized sensitivity attained till now is still lower than the theoretically calculated sensitivity limit. Also, the structures implemented to achieve higher sensitivity require complex and expensive fabrication techniques which may limit the usage of such devices. In this thesis, the structural parameters of GMR device are investigated for achieving high sensitivity close to the

theoretical limit and the application of GMR spectroscopy is implemented for designing and developing an in-house built read-out system based on open-source platform for application towards biomedical and environmental sensing.

1.1 Rationale and Problem Statement

Theoretically, the highest normalized sensitivity of GMR for solution-based sensing is equivalent to the period of the grating. Practically, such sensitivity has not been achieved for normal symmetry GMR structures. Also, the tools reported for fabricating structures that result in enhanced sensitivity require complex fabrication techniques that increases the overall cost of the device. The realization of a portable, user-friendly technological biosensing device based on an open-source platform has not been commonly reported.

1.2 Objectives of the Study

The objective of this thesis is divided into two parts. The first part of the thesis aims to deliver a comprehensive study of the exclusive nature of the Rayleigh resonance anomaly in the guided mode resonant structure having one dimensional (1-D) and two-dimensional (2-D) periodic grating. The investigation of the resonance principle is established for 1-D and 2-D structures for super mode excitation at Rayleigh wavelength. This focuses on the study of the effect of the structural specifications such as the grating period, the fill factor, the grating depth, and the film thickness on the resonance response for Transverse Electric (TE) and Transverse Magnetic (TM) polarizations. The normalized sensitivity for each structure is calculated from bulk

sensitivity. The resonance response for guided mode resonance is compared to near cut off resonance. Based on these findings, several GMR devices are proposed and practically tested.

The second part of the thesis aims to design and develop a portable guided mode resonance spectroscopy-based read-out system utilizing 3D printing technology. The application of the read-out system for biomedical and environmental sensing is realized using off-the-shelf components and open-source software. Here, 1D GMR structure is used as a transducer and studied for resonance response. Ray tracing approach is used for designing the read-out arrangement. The design of the spectrometer built on optical parameters is explained and design optimization is illustrated. The optimal design is packaged using 3D printing technology and tested with solutions to check the response of the system.

1.3 Scope of study

The sensitivity of GMR can be manipulated based on the structural parameters of the device. In this study, the optimization of grating parameters like the thickness of the waveguiding film, fill factor, grating depth is essential to confine the field in the grating sensing region. A higher field overall with the sensing parameters results in better sensitivity. To realize a portable and user-friendly read-out system, low-cost packaging techniques, off-the-shelf components and an open-source platform for making user-friendly interface feasible for updating from time to time for monitoring and displaying the real-time data for biomedical and environmental applications is needed.

1.4 Research Questions

-The possibility of exciting a mode near cut-off such as the maximum overlap of the field at resonance within the sensing region results in a sensitivity that is comparable to theoretical limit.

-Practicalities of designing a webcam-based spectroscopy setup using off-the-shelf imaging systems to develop portable and compact open-source embedded systems that can be used for biomedical and environmental sensing.

1.5 Significance of the study

In the first part of the study, the findings will result in an alternative approach for enhancing the sensitivity in a dielectric multilayer GMR structure. The structure would comprise of film having high RI coated on top of a film having low RI. Such an assembly can be fabricated using simpler and compatible techniques such as imprinting, hot-embossing technique, or plastic injection molding.

In the second part of the study, a platform for designing a GMR spectroscopy-based read-out system is proposed which can be used for threshold detection in biomedical and environmental sensing applications.

In the next chapter literature review on various approaches for enhancing GMR sensitivity is covered. The concept of GMR is explained. The details and concepts on the approaches are described and the challenges in the application of such methods are explained. Maxwell's equations, Diffraction phenomenon, and waveguiding will be elaborated to provide background for the analysis of GMR devices. For the second part

of the study, a literature review on designing and application of read out systems based on spectrometers is explained. The use of smartphones as a potential device for micro-spectrometry is illustrated. The application of open-source embedded systems as an alternative to the smartphone for next-generation Point-of-Care applications is explained. Finally, the hypothesis and theoretical framework for the study is presented.

In chapter three, the first part of the methodology covers the description of the Rigorous Coupled Wave Analysis (RCWA) which is the numerical method used to calculate the field magnitude of the diffraction waves. The Scattering Matrix Method and Transmission matrix approach (TMM) are explained. In the second part of the methodology, the realization of the webcam spectrometer-based readout system is explained. The dependency the of object distance, imaging distance, and the number of pixels enclosed by the camera is explained in relation to the diffraction grating period. The effect of the focal length of the lens of the webcam on the design of the spectrometer is also described. Raspberry Pi and image processing techniques used for spectrum captured by the spectrometer and calculation of peak resonant value are elaborated.

Chapter four illustrates the findings of the first part of the study. That includes the optimization of 1D and 2D GMR structure by varying different structural parameters. The optimal structure with the highest diffraction efficiency is selected for fabrication. The characterization of the structure is performed to study the profile and sensitivity. The fabrication process is explained in detail and the device is tested for bulk sensitivity using solutions of different refractive indices. The sensitivity is

calculated from the experimental results and compared with the theory.

In chapter five, the second part of the study is explained. Development of the read-out system is explained and the response of the system is proved using solutions of glycerol mixed with de-ionized (DI) water having different refractive indices. The system performance is reported.

The last chapter discusses the current findings and future applications and recommended research. The possibility of improving the system is also discussed and the scopes for future developments are suggested.

CHAPTER 2

LITERATURE REVIEW

2.1 Sensitivity Enhancement in GMR structures

The GMR wavelength depends upon the device's structural dimensions and refractive indices of the surrounding medium (Zheng et al., 2014), (H.-A. Lin & Huang, 2016), (Qian et al., 2016). Varying the RI of the medium surrounding the GMR device will result in a shift of the resonant wavelength (L. Liu et al., 2016), (Magnusson et al., 2010). This characteristic of GMR encourages its use for label-free biosensing applications.

The performance of any GMR biosensor depends on the sensitivity which is defined as the shift in the peak wavelength value (PWV) at resonance condition divided by the variation in the RI of the analyte (B. T. Cunningham et al., 2004). The sensitivity of the biosensor is determined by three key parameters, as modeled by Ian D. Block et. al.: device grating period, the effective index of the device and the interaction of the electric field intensity with the detection zone (Block et al., 2008). The group predicted that the sensitivity of any photonic crystal biosensor was dependent on the mentioned three factors. The modeling of the device is based on the reverse symmetry structure proposed by R. Horvath et. al. (Horváth et al., 2002) where the RI of the layer under the grating is lower than the RI of the cover medium. Figure 2.1 shows a reverse symmetry structure where $n_g < n_{sup}$. For water as a superstrate ($n_{sup} = 1.33$) and for the layer below the grating having a low index ($n_g = 1.17$),

the tail of the electric field at resonance extends further in the superstrate region compared to the region below the grating. This is in contrary to the case of normal symmetry structure. Such an electric field results in higher interaction with the analyte region and gives better bulk sensitivity as compared to normal symmetry structures.

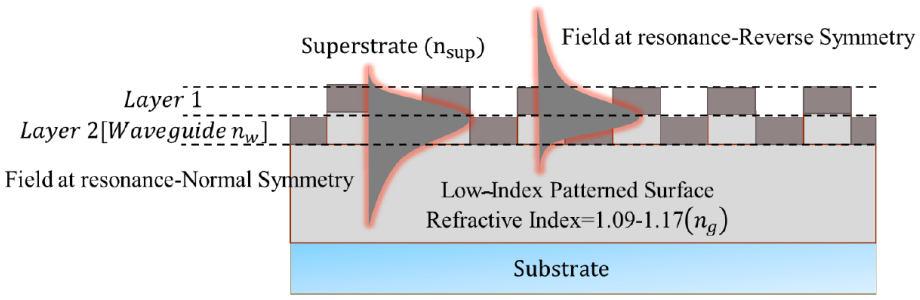

Figure 2.1: Reserve symmetry structure

1-D resonant waveguide grating structures have distinct reflectance peaks for Transverse Electric (TE) and Transverse Magnetic (TM) mode of the field which have a different distribution of strength in the grating structure (S. S. Wang & Magnusson, 1993b), (Magnusson & Wang, 1992). The influence of Transverse Electric (TE) and Transverse Magnetic mode on the distribution of electric field was studied by Qi Wang et. al. (Q. Wang et al., 2012). They concluded that TM mode is more sensitive than TE mode of polarization and hence the TM polarization of incident light was studied more for sensitivity calculations in biosensors (Wei et al., 2006).

Numerous strategies have been projected in literature, to improve the sensitivity of the device through field enhancement in the area overlying the sensing film. The electric field enhancement has been achieved by numerous methods such as manipulating the geometry of the GMR structure, inserting buffer layers, using low-

index substrate and oblique incidence techniques. These methods are explained below. A thin grating waveguide structure was proposed by David Fattal et. al (Fattal et al., 2007) that can contribute to less modal confinement and hence higher sensitivity. The suggested structure of the grating design is shown in figure 2.2.

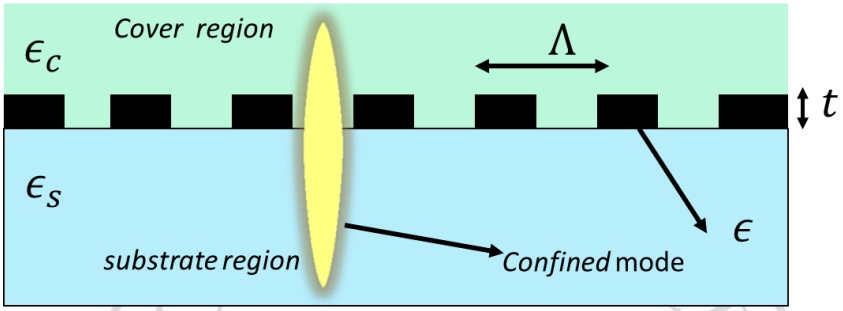

Figure 2.2: Thin grating waveguide structure

A grating with a minimum sub-wavelength thickness and asymmetrical grating is proposed to extend the modal distribution into the sensing region. This results in a sensitivity that is almost equal to the theoretical limit (Yariv & Yeh, 1984). Such sensor structure showed a good potential for gas or liquid sensing applications. Guilian Lan et. al. (Lan et al., 2019) and Yi Zhou et. al (Zhou et al., 2019) worked on optimizing the grating parameters to increase the evanescence wave on the sensing surface with asymmetrical mode distribution. They control several factors such as the depth of the grating, duty cycle, and the film properties such as porous silicon dioxide (SiO2). The sensing was performed by varying refractive indices from 1.4 to 1.41 and the bulk sensitivity achieved in this case was equal to the period of the grating.

In another work, a gold layer (RI,n_m) is inserted between the grating (RI,n_g) and the substrate layer (RI,n_s). This presented a spectral response with inverted profile

that resulted in a strong field extension on the surface (S.-F. Lin et al., 2012). The device is called metal layer assisted GMR (MaGMR) as shown in figure 2.3. The metal layer removes the issue of low sensitivity due to higher second critical angle $\theta_{critical\,2}$. The sensitivity was tested for oblique incident angle in the near-infrared region.

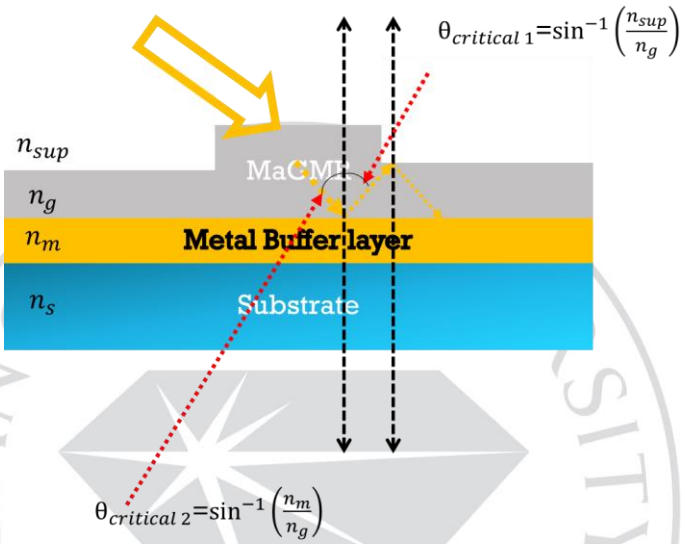

Figure 2.3: MaGMR structure with addition of a metal buffer layer between the grating layer and the substrate layer.

Another approach was given by Jiayong et. al (Ma & Zhang, 2012) for biosensing where a sensitivity close to the grating period was calculated when used for sensing different liquids and gases. The proposed GMR structure is called as self-suspended-membrane-type gratings (SSG) as shown in figure 2.4. In this structure, the cover, the substrate and the grating layer (high and low) refractive indices are labeled as n_c, n_s, n_h, n_l respectively. f, T, d_g are the fill factor, grating period, and the grating depth respectively.

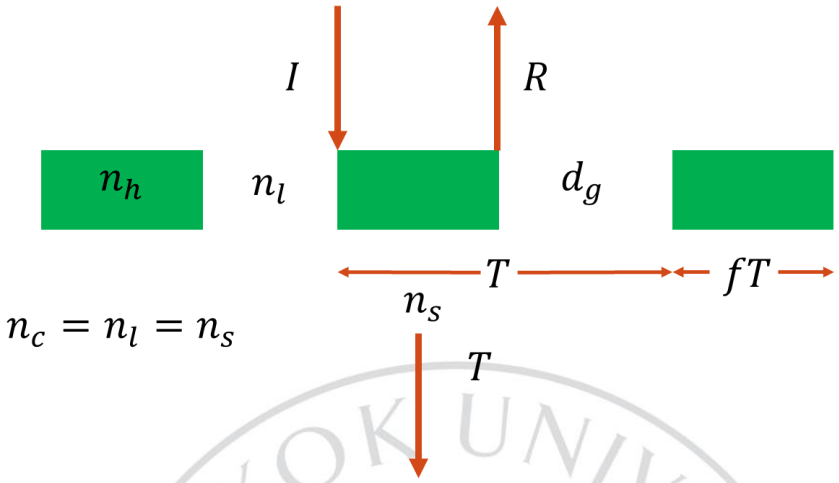

Figure 2.4: Self-suspended-membrane-type-gratings (SSGs)

In the calculations for a first diffracted order coupling with a waveguide mode, the normalized sensitivity can reach the maximum theoretical limit. The sensitivity of the device was calculated using RCWA for liquids such as water, chloroform, benzene and carbon disulfide. It was found to be 1450 nm/RIU. For gas detection such as ammonia, methane and methyl alcohol, the resonance wavelength was found to be in the mid-IR range. A similar suspended structure was proposed by Mohamed El Beheiry et. al (El Beheiry et al., 2010). In that work, two-dimensional periodical lattice holes are inserted in the slab resulting in a guided mode resonances and symmetrical structure. The obtained resonant modes showed increase in bulk sensitivity that may be applied for sensing large analytes such as bacteria and cells.

In another approach by Sakoolkan Boonruang et. al. (Boonruang & Mohammed, 2011) sensitivity enhancement was achieved by inserting a cladding film as a sensing layer in multilayer GMR structure as shown in figure 2.5 (a). The

sensitivity of the device can be enhanced by increasing the thickness of the cladding layer. Figure 2.5 (b) shows the mode profiles of a guided mode, a super mode, a grating mode and a cladding mode which are excited in the structure at different wavelengths. The mode profile of the cladding mode clearly shows greater strength in the sensing region which results in higher sensitivity as compared to other modes. For high index sensing, the cladding mode sensitivity increases up to 32 times as compared to traditional guided mode.

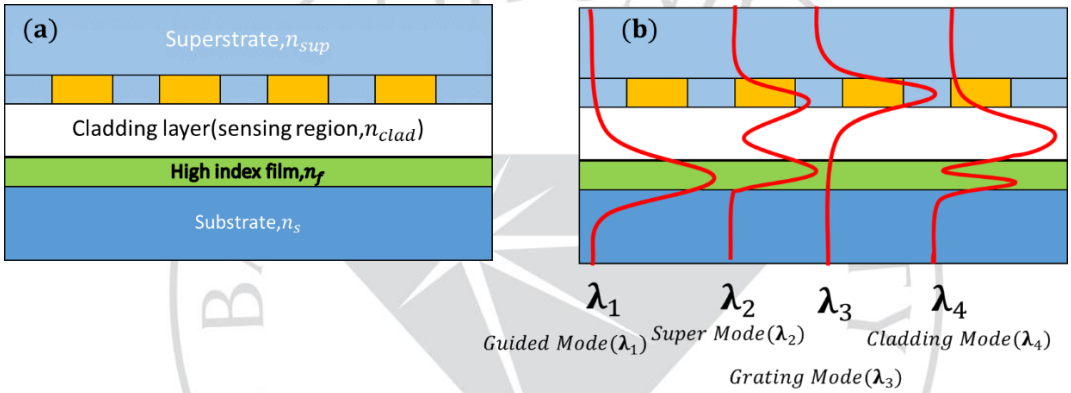

Figure 2.5: (a) Cladding layer between grating and high-index film (b) mode profile for guided mode (λ_1), super mode (λ_2), grating mode (λ_3) and cladding mode (λ_4).

Amalgamation of a porous TiO_2 layer in the form of nanorods was done by Wei Zhang et. al to (W. Zhang et al., 2008) to improve the surface area of the sensing region. The structure of the photonic crystal biosensor with nanorods on the surface is displayed conceptually in figure 2.6.

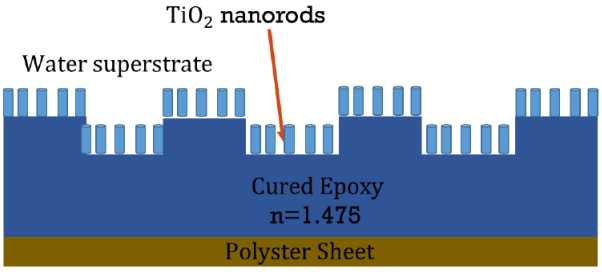

Figure 2.6: Titanium Dioxide (TiO_2) deposited PC biosensor structure

The nanorods film was deposited on top of the grating layer by glancing angle deposition method in an e-beam evaporation arrangement. A larger surface area would result in increased sensitivity due to a larger density of the capture ligand on the surface of the sensor. This approach, and others that are based on increasing ligand surface area, may not be appropriate for forming plastic-based sensor structures. The sensitivity of the biosensor was compared with and without the nanorods coating. It was found experimentally that the sensitivity increased by four times through the incorporation of a high surface area nanorods layer. The idea of fabricating porous film by deposition of a uniform sheet of tilted nanorods and its application to function in an aqueous medium as a biosensor was later tested by Qinglan Huang et. al (Huang et al., 2016). The research work explained that the porous film enhanced the sensitivity by increasing the area of integration and adjusting the intensity of the electric field profile. The calculated bulk sensitivity of the sensor having a porous layer was reported to be 316 nm/RIU as compared to a non-porous layer which had a bulk sensitivity of 212 nm/RIU. This clearly indicated an increase of the sensitivity by 1.5 times. Similar structure was

fabricated based on a plastic substrate as in figure 2.7.

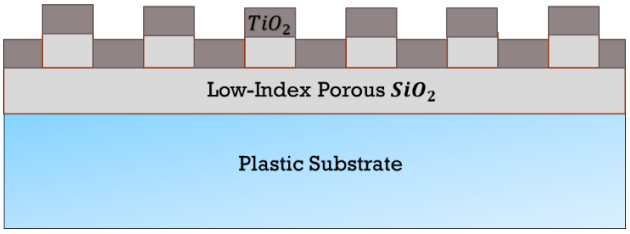

Figure 2.7: Photonic Crystal biosensor with plastic substrate

Another type of structural modification in the GMR device was demonstrated by Seyyed Abbas Jazayeri et. al (Moghaddas et al., 2013). Coupled cross stacked grating GMR (ccs-GMR) structure is proposed for RI sensing. The unit cell ccg-GMR structure is displayed in figure 2.8 (a) and the complete GMR devices is shown in figure 2.8 (b). The structure comprises of three layers, with first and third layer is a silicon nitride grating having an equal thickness of d_w with its the grating vector along the x-direction and the middle layer of the same material but lesser thickness d_g than d_w.

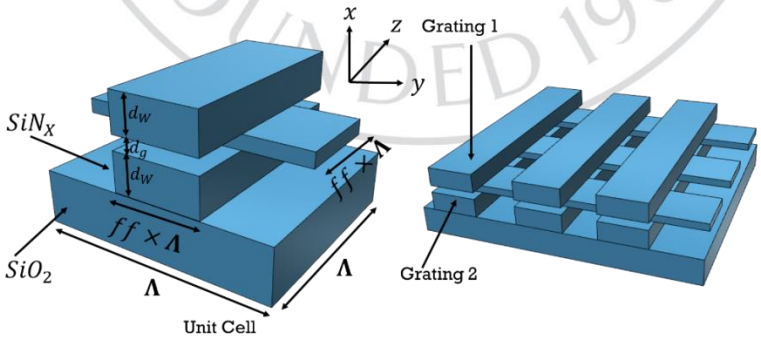

Figure 2.8: (a) ccs-GMR unit cell structure (b) ccs-GMR periodic structure

When the structure is surrounded by a solution such as an analyte it behaves as

two structures: first one with SiO_2 substrate and another with H_2O as substrate. By controlling the thickness of the middle layer with thickness d_g, the coupling of the modes in the asymmetric structure result in formation of supermodes at longer wavelengths. Higher bulk sensitivity is obtained as compared to a conventional single grating structure.

GMR devices are sensitive to the angle of incidence (Piper & Fan, 2014). Though, most of the research work focuses on normal incidence at a structure in the sub-wavelength region, which signify that the grating period is lesser than the resonance wavelength. Smaller grating periods have structural deviations and challenging fabrication techniques. Hence, Linyong Qian et. al. (Qian et al., 2015) projected a model for increasing the bulk sensitivity of GMR sensor device by operating at larger periods by controlling the angle of incidence. The resonant wavelength can then be shifted closer to the grating period and the bulk sensitivity is enhanced by many folds. This form of excitation causes a reduction in the resonance efficiency due to coupling between leaky modes and high evanescent diffraction orders. Despite the reduced diffraction efficiency, it is still sufficient enough for biosensing applications (Ku et al., 2015).

2.2 Rayleigh anomaly in biosensing applications

Rayleigh anomaly (RA) has been used in concentric and linear metallic gratings for bulk sensing applications (Savoia et al., 2013), (Maystre, 2012). RA is observed as a sharp dip in the reflection spectrum for a scattered wave that is tangential to the grating surface. The dip wavelengths are commonly attributed as Rayleigh wavelengths or cut-

off wavelengths. The advantages of RA for RI sensing are (1) the bulk sensitivity is entirely reliant on the period of the grating (2) the location of PWV is linearly dependent on the environment RI (3) broad spectral range of operation by oblique incident angle. All these factors make RA based biosensing a good candidate for bulk sensing applications (Eitan et al., 2015), (F. Liu & Zhang, 2016), (Steele et al., 2003).

The surface sensing capability of RA was not however as good as bulk sensing. To improve surface sensing capacity coupling of RA with SPP or LSPR was done to achieve high field confinement near the grating region. In another work, 1-D metal/dielectric multilayer grating biosensor based on RA was proposed for surface sensing (Su et al., 2019). This biosensor had the feasibility of changing the wavelength of RA by varying the angle of incidence, and the period of the grating.

2.3 Spectroscopy for sensing applications

GMR Spectroscopy has remained a capable stage for application towards environmental and biomedical sensing (Sader & Sayyed-Ahmad,2013), (Tabassum et al., 2017). The read-out systems based on GMR that have been used for detecting analytes mostly rely on commercial spectrometers (Deb et al., 2020). As alternative much research is done towards integrating GMR based transducers with compact spectrometers for point of care, real time, and easy to use detections (Choi et al., 2016). The introduction of smartphones as a platform for building portable, economical optical spectroscopic devices has shown ability for point of care diagnostics (Kwon et al., 2016), (D. Zhang & Liu, 2016), (Roda et al., 2016). Considerable work has been completed in using smartphones as an imaging tool meant for spectroscopic

applications. A spectrometer based on smartphone was designed and applied towards remote sensing of atmospheric Sulphur dioxide by Thomas C. Wilkes et. all (Wilkes et al., 2017). In another work, a spectrometer built using a smartphone was considered and applied for double recognition of fluorescence and absorption of metal ions in water (Hossain et al., 2015). Their idea of sensing metal ions is grounded on the measurement of fluorescence in the visible spectrum and absorption in the UV spectrum. Another work established the application of a smartphone-based spectrometer by utilizing bundled optical fiber for assessing the quality of fruit samples (Hossain et al., 2016). The absorbance from the samples was recorded in the visible-near infrared spectrum. However, in literature, there have been limited read-out systems based on GMR transducer which can be worked for lab-on-chip technology targeting for possible integration with a smartphone or an imaging and processing device. A chirped GMR-based biosensor was projected for parallel detection of multiple protein biomarkers in human urine (Kenaan et al., 2020). The collective analyte recognition and imaging ability of the chirped GMR biosensor substitute the need for a bulky and costly spectrometer. In another work, a gradient grating period type GMR filter was proposed for integration with a smartphone (H.-A. Lin et al., 2016).

The advantages of using the built-in sensors of a smartphone as an analytical tool are convincing however it also brings numerous challenges. With smartphone corporations engineering a variety of smartphones having diverse specifications, building a biosensor based on smartphone is challenging and it is more appropriate to concentrate on a single design. As a substitute, open-source microcontrollers such as

Raspberry Pi and Arduino can provide an alternate diagnostic platform for environmental and biomedical sensing applications in contrast to outmoded arrangements (Wilkes et al., 2016), (Bougot-Robin et al., 2016). The small-sized microcontroller chips with higher competencies for computation, networking, and communication united with accessible interface could be the succeeding opportunity of scheming readout systems (Nguyen et al., 2018), (Somarapalli et al., 2018).

CHAPTER 3

THEORY AND DESIGN

This chapter covers the needed theoretical background for the two parts of the thesis work. This includes the diffraction by the gratings, guided mode resonance, modal analysis, scattering matrix, transfer matrix analysis and imaging.

3.1 Diffraction by gratings

Gratings are periodic structures that can modulate the amplitude or the phase of the incident light through attenuation, permittivity, or topography. In either case, the incident light is diffracted into multiple directions outside the grating based on the grating period. Each order of diffraction is specified by the direction in which the diffracted light waves constructively interfere (Hecht, 1998).

In terms of light propagation, the grating is set to affect the component tangential to the wave vector of the output field. The tangential component of the wave vector of the n^{th} diffraction order $(\vec{k}_{n,tan})$ is given as

$$\vec{k}_{n,tan} = \vec{k}_{inc,tan} - n\vec{K}_{G,tan} \quad 3.1$$

In equation 3.1, $\vec{K}_{tan}$ is the tangential component of the wave vector of the incident light. The term $\vec{K}_{G,tan}$ is the tangential component of the grating vector. The grating vector is defined as $\vec{K}_G = \frac{2\pi}{\lambda}\hat{e}_G$, where $\hat{e}_G$ is a unit vector normal to the grating periodicity. Figure 3.1 shows a grating diffracting the incident light into different orders $(n = 0, \pm 1, \pm 2)$ where the waves diffracted in different directions have the tangential

wave vectors $\vec{k}_{n,\,tan} < \vec{k}_0 n_{1,2}$. Here, n_1 and n_2 are considered as the refractive indices of the surrounding regions. k_0 is the free space wave vector defined as $k_o = \frac{2\pi}{\lambda}$.

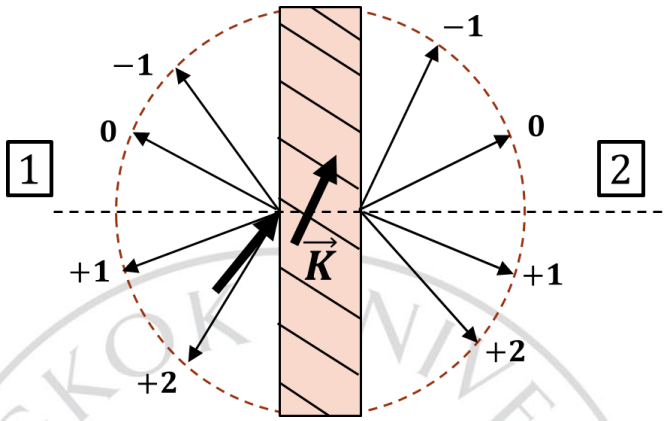

Figure 3.1: 1-D grating and diffraction directions

3.1.1 One-dimensional (1-D) grating

One-dimensional grating is periodic only in one direction as shown in Figure 3.2. The grating is periodic in x-axis with a grating period Λ_a.

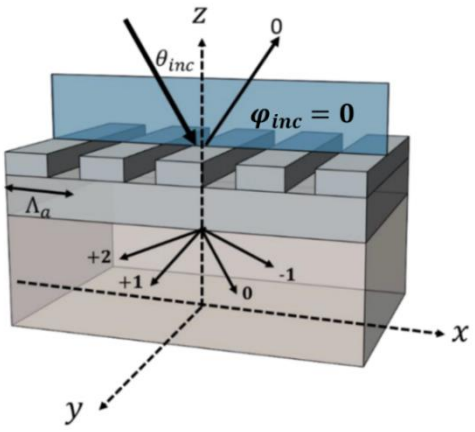

Figure 3.2: Diffraction in 1-D grating

The grating vector $(\vec{K})$ in this case has a magnitude of $2\pi/\Lambda_a$.The grating equation is written as

$$k_{x,p} = k_0 n_{inc} \sin\theta_{inc} \cos\varphi - p\frac{2\pi}{\Lambda_a} \quad 3.2a$$

$$k_{y,p} = k_0 n_{inc} \sin\theta_{inc} \sin\varphi, \quad 3.2b$$

Where $k_{x,p}$ and $k_{y,p}$ are the components of wave vector that are in tangential direction to the boundary of the p^{th}, diffracted order. The angles θ_{inc} and φ_{inc} are the radical incident angles. The constant n_{inc} is the incident medium's RI. The directions of the diffracted waves can be given as

$$\theta_p = \tan^{-1}\left\{\frac{\sqrt{k_{x,p}^2 + k_{y,p}^2}}{k_{z,p}}\right\}, \quad 3.3a$$

$$\varphi_p = \tan^{-1}\left\{\frac{k_{y,p}}{k_{z,p}}\right\}, \quad 3.3b$$

$$k_{z,p} = \sqrt{(k_0 n_{out})^2 - k_{x,p}^2 - k_{y,p}^2} \quad 3.3c$$

The term $k_{z,p}$ is the wave vector of the p-th order of diffracted where z direction is set to be normal to the grating surface. The grating-medium interface is set to be in the x-y plane.

3.1.2 Two-dimensional (2-D) grating

The structure of a 2-D cross grating that is periodic in two directions with periods Λ_a and Λ_b as represented in figure 3.3. The diffraction pattern is shown in Figure 3.2 with two-unit cells C_a and C_b.In such a 2-D pattern, the grating vectors are inscribed as

$$\vec{K} = C_a\vec{a} + C_b\vec{b} \qquad 3.4$$

Here, p and q diffraction orders are the harmonics along grating vectors $\vec{C}_a$ and $\vec{C}_b$ respectively.

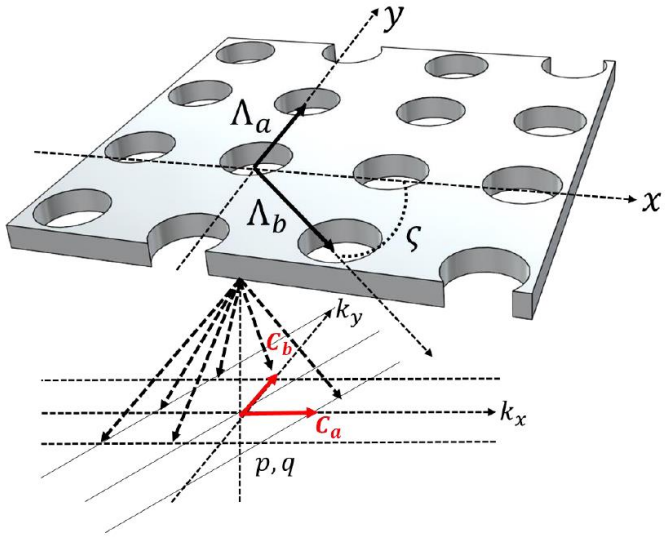

Figure 3.3: Two-dimensional crossed diffraction grating

For the generalized case, the grating vectors are rotated along $\vec{k}_x$ and $\vec{k}_y$ direction as follows

$$\vec{C}_{a,p} = p\frac{2\pi}{\Lambda_b \cos(\varsigma)}\vec{k}_x, \qquad 3.5a$$

$$\vec{C}_{b,p} = q\frac{2\pi}{\Lambda_a}\tan(\varsigma)\,\vec{k}_x + q\frac{2\pi}{\Lambda_a}\vec{k}_y \qquad 3.5b$$

The grating vectors in the new co-ordinates are

$$\vec{K}_{pq} = K_{x,pq}\vec{k}_x + K_{y,pq}\vec{k}_y$$

$$= \left\{p\frac{2\pi}{\Lambda_b \cos(\varsigma)} + q\frac{2\pi}{\Lambda_a}\tan(\varsigma)\right\}\vec{k}_x + q\frac{2\pi}{\Lambda_a}\vec{k}_y \quad 3.6$$

The diffracted wave vectors are found from the 2-D grating equations as follows

$$k_{x,pq} = k_{x,inc} - \left(p\frac{2\pi}{\Lambda_b \cos(\varsigma)} + q\frac{2\pi}{\Lambda_a}\tan(\varsigma)\right) \quad 3.7$$

$$k_{x,pq} = k_{y,inc} - q\frac{2\pi}{\Lambda_a} \quad 3.8$$

Here, $k_{x,pq}$ is the wave vector component that is tangential to the boundary of a diffracted order designated by p in a-direction and q in b-direction. In 2-D grating structure, the diffracted orders position in several planes of diffraction and multiple waves can propagate in the common plane. Equations (3.7) and (3.8) show that there can be multiple values of p ranging from $-\infty < p < \infty$ for a given value of q (Boonruang, 2007).

3.2 Rigorous Coupled Wave Analysis

The rigorous coupled wave analysis (RCWA) (Moharam, Grann, et al., 1995), (Moharam, 1988), (Lalanne, 1997) technique is implemented to calculate the field magnitude of each diffracted wave from the grating structure. This method is grounded on the plane wave expansion method and provides the exact solution of Maxwell's equations in the frequency domain. The exactness of the technique is based on the convergence of the solutions which depends entirely on the number of harmonics under computation. The spatial harmonics of the tangential electric and magnetic field Eigen modes are computed within the grating layer derived from the coupled wave equations.

Then proper boundary conditions are implemented through the transmission matrix approach (Moharam, Pommet, et al., 1995) to compute the field outside the structure.

The normalized incident electric field is given as

$$\vec{E}_{inc} = \vec{u}\, e^{[-j(k_{x,inc}x + k_{y,inc}y + k_{z,inc}z)]}, \qquad \vec{u}.\vec{k} = 0 \tag{3.9}$$

In equation 3.9, the normalized incident electric field vector is specified by the vector $\vec{u}$. The electromagnetic fields in the interior of the periodic structure are denoted by the summation of the space-harmonic components (p,q).

$$\vec{E}_g = \sum_p \sum_q \vec{S}_{pq}(z) e^{[-j(k_{x,pq}x + k_{y,pq}y)]} \tag{3.10}$$

$$\vec{H}_g = -j\eta_0^{-1} \sum_p \sum_q \vec{U}_{pq}(z) e^{[-j(k_{x,pq}x + k_{y,pq}y)]} \tag{3.11}$$

where $\vec{S}_{pq}(z)$ and $\vec{U}_{pq}(z)$ are the z-spatial components of the normalized electric and magnetic fields respectively, and $\eta_0 = \sqrt{\mu_0/\varepsilon_0}$ where $\mu_0 = 4\pi \times 10^{-7}\, H/m$ is the permeability of free space and $\varepsilon_0 = 8.854 \times 10^{-12}$F/m is the permittivity of free space.

The reflected electric fields $(\vec{E}_R)$ and transmitted electric fields $(\vec{E}_T)$ outside the structure can also be expressed as summations of the space harmonics,

$$\vec{E}_R = \sum_p \sum_q \vec{E}_{r,pq}\, e^{[-j(k_{x,pq}x + k_{y,pq}y - k_{1,z,p,q}z)]} \tag{3.12}$$

$$\vec{E}_T = \sum_p \sum_q \vec{E}_{t,pq}\, e^{[-j(k_{x,pq}x + k_{y,pq}y + k_{2,z,p,q}z)]} \tag{3.13}$$

Where $k_{1,z,pq}$ and $k_{2,z,pq}$ are the normal components of the wave vectors for the diffracted

orders in the incident region and the substrate region respectively. $\vec{E}_{r,pq}$ and $\vec{E}_{t,pq}$ represent the electric fields of the reflected and transmitted waves.

3.2.1 Coupled Wave Equations (CWE)

CWE deals with calculating the Eigen modes inside the grating structure for the transmitted and reflected fields. The CWE reserve the continuousness of the EM fields along the different layers of the structure with different values of permittivity/permeability. Hence, they can be formulated for non-magnetic materials (Lalanne, 1997) as

$$\begin{bmatrix} \frac{\partial S_y}{\partial(k_0 z)} \\ \frac{\partial S_y}{\partial(k_0 z)} \end{bmatrix} = \begin{bmatrix} K_y E^{-1} K_x & I - K_y E^{-1} K_y \\ -I + K_x E^{-1} K_x & -K_x E^{-1} K_y \end{bmatrix} \begin{bmatrix} U_y \\ U_x \end{bmatrix} \quad 3.14a$$

$$\begin{bmatrix} \frac{\partial U_y}{\partial(k_0 z)} \\ \frac{\partial U_x}{\partial(k_0 z)} \end{bmatrix} = \begin{bmatrix} K_y K_x & E_x - K_y^2 \\ K_x^2 - E_y & K_x K_y \end{bmatrix} \begin{bmatrix} S_y \\ S_x \end{bmatrix} \quad 3.14b$$

Here the matrices $E_y = \alpha_1 E + (1 - \alpha_1) A^{-1}$ and $E_x = \alpha_2 A^{-1} + (1 - \alpha_2) E$ describe the consistency of the electric field tangential component tangential at the grating groove surface. The features α_1 and α_2 indicate the relative strengths between the matrices E and A. Their values are in the positive interval [0,1]. With proper selection of the values for α_1 and α_2, the convergence rate can be maximized which in turn can reduce the total number of space harmonics, M, required for getting precise results. $I_{M \times M}$ is an identity matrix. K_x and K_y are diagonal matrices containing the tangential wave vectors components, $k_{x,pq}$ and $k_{y,pq}$, respectively.

In many cases it is more appropriate to write the equations above in terms of components that are parallel (∥) and perpendicular (⊥) to the plane of diffraction.

$$\begin{bmatrix} \frac{\partial S_{\perp}}{\partial(k_0 z)} \\ \frac{\partial S_{\parallel}}{\partial(k_0 z)} \end{bmatrix} = \begin{bmatrix} A_{\perp,\perp} & A_{\perp,\parallel} \\ A_{\parallel,\perp} & A_{\parallel,\parallel} \end{bmatrix} \begin{bmatrix} U_{\perp} \\ U_{\parallel} \end{bmatrix}, \tag{3.15a}$$

Where $A_{\perp,\perp} = 0,\ A_{\perp,\parallel} = I, A_{\parallel,\perp} = K_n E^{-1} K_n - I,$ and $A_{\parallel,\parallel} = 0$

$$\begin{bmatrix} \frac{\partial U_{\perp}}{\partial(k_0 z)} \\ \frac{\partial U_{\parallel}}{\partial(k_0 z)} \end{bmatrix} = \begin{bmatrix} B_{\perp,\perp} & B_{\perp,\parallel} \\ B_{\parallel,\perp} & B_{\parallel,\parallel} \end{bmatrix} \begin{bmatrix} S_{\perp} \\ S_{\parallel} \end{bmatrix}, \tag{3.15b}$$

Where $B_{\perp,\perp} = K'_y E_y K'_x - K'_x E_x K'_{y,}$, $B_{\perp,\parallel} = K'_y E_y K'_y - K'_x E_x K'_{x,}$

$B_{\parallel,\perp} = K_y^2 - K'_x E_y K'_x - K'_y E_x K'_{y,}$ and $B_{\perp,\parallel} = -K'_x E_y K'_y + K'_y E_x K'_{x.}$

In (3.15a) and (3.15b), K'_x, K'_y, K'_n are the diagonal matrices:

$$K'_x = \left[\frac{k_{x,pq}}{\sqrt{k_{x,pq}^2 + k_{y,pq}^2}} \right]_{M \times M}, \quad K'_y = \left[\frac{k_{y,pq}}{\sqrt{k_{x,pq}^2 + k_{y,pq}^2}} \right]_{M \times M}, \text{ and } K_n = \left[\frac{\sqrt{k_{x,pq}^2 + k_{y,pq}^2}}{k_0} \right]_{M \times M}$$

Merging the two coupled wave equations of (3.15a) and (3.15b), differential matrix equations of the second order is written as

$$\begin{pmatrix} \frac{\partial^2 S_{\perp}}{\partial(k_0 z)^2} \\ \frac{\partial^2 S_{\parallel}}{\partial(k_0 z)^2} \end{pmatrix} = \begin{bmatrix} A_{\perp,\perp} & A_{\perp,\parallel} \\ A_{\parallel,\perp} & A_{\parallel,\parallel} \end{bmatrix} \begin{bmatrix} B_{\perp,\perp} & B_{\perp,\parallel} \\ B_{\parallel,\perp} & B_{\parallel,\parallel} \end{bmatrix} \begin{bmatrix} S_{\perp} \\ S_{\parallel} \end{bmatrix} = [A][B] \begin{bmatrix} S_{\perp} \\ S_{\parallel} \end{bmatrix} \tag{3.16}$$

Eq. 3.16 can be written in the form of an Eigen-value problem as

$$\mu^2 \begin{bmatrix} S_{\perp} \\ S_{\parallel} \end{bmatrix} = [A][B] \begin{bmatrix} S_{\perp} \\ S_{\parallel} \end{bmatrix} \tag{3.17}$$

The solution of the Eigen-value problem in eq. 3.17 can be written in relation to the space harmonics of the electric fields $\vec{S}(z)$ as

$$\begin{bmatrix} S_{\perp} \\ S_{\parallel} \end{bmatrix} = \begin{bmatrix} W_1 e^{-k_0 \mu z} & W_1 e^{k_0 \mu (z-d)} \\ W_2 e^{-k_0 \mu z} & W_2 e^{k_0 \mu (z-d)} \end{bmatrix} \begin{bmatrix} C^+ \\ C^- \end{bmatrix} \quad 3.18$$

Where $[\mu^2]_{2M \times 2M}$ is the Eigen value matrix and [W] = $\begin{bmatrix} W_1 \\ W_2 \end{bmatrix}_{2M \times 2M}$ is the Eigen vector matrix. The space harmonics of the magnetic fields $\vec{U}(z)$ are

$$\begin{bmatrix} U_{\perp} \\ U_{\parallel} \end{bmatrix} = \begin{bmatrix} -V_1 e^{-k_0 \mu z} & V_1 e^{k_0 \mu (z-d)} \\ -V_2 e^{-k_0 \mu z} & V_2 e^{k_0 \mu (z-d)} \end{bmatrix} \begin{bmatrix} C^+ \\ C^- \end{bmatrix} \quad 3.19a$$

$$[V] = \begin{bmatrix} V_1 \\ V_2 \end{bmatrix}_{2M \times 2M} = [A]^{-1}[\mu][W] \quad 3.19b$$

The terms C^+ and C^- in equations (3.18) and (3.19) denote the magnitude coefficients of the electric fields when propagating in the forward and backward directions in the interior of the periodic medium with thickness *d*. The coefficients $\mu_{pq} = k_{z,pq,grating}/k_0$ indicate the propagating waves inside the grating region. The effective indices of the subwavelength grating normal and parallel polarizations, $n_{\perp}$ and $n_{\parallel}$, are directly assessed by μ_{00} (Grann et al., 1994). Here, C^+ and C^- are unknown parameters that will get subtracted when the boundary conditions are implemented to compute the diffracted fields exterior to the grating region.

3.2.2 Boundary condition: transmission matrix approach (TMA)

For a single layer grating having a thickness d, the electric and magnetic field tangential components at the interfaces z = 0 and z = d can be written as

z = 0

$$\begin{bmatrix} E_{inc,\perp}\delta_{00} \\ Z_{1,00}\eta_0 H_{inc,\perp}\delta_{00} \\ j\eta_0 H_{inc,\perp}\delta_{00} \\ Y_{1,00}\eta_0 E_{inc.\perp}\delta_{00} \end{bmatrix} + \begin{bmatrix} I & 0 \\ 0 & jZ_{1,pq} \\ 0 & I \\ jY_{1,pq} & 0 \end{bmatrix} \begin{bmatrix} E_{r,pq,\perp} \\ j\eta_0 H_{r,pq,\perp} \end{bmatrix} = \begin{bmatrix} W_1 & W_1X \\ W_2 & W_2X \\ -V_1 & V_1X \\ -V_2 & V_2X \end{bmatrix} \begin{bmatrix} C^+ \\ C^- \end{bmatrix}$$

3.20a

z = d

$$\begin{bmatrix} W_1 & W_1X \\ W_2 & W_2X \\ -V_1 & V_1X \\ -V_2 & V_2X \end{bmatrix} \begin{bmatrix} C^+ \\ C^- \end{bmatrix} = \begin{bmatrix} I & 0 \\ 0 & jZ_{1,pq} \\ 0 & I \\ jY_{1,pq} & 0 \end{bmatrix} \begin{bmatrix} E_{t,pq,\perp} \\ j\eta_0 H_{t,pq,\perp} \end{bmatrix} \qquad 3.20b$$

Where $X, Z_{l,00}\, and\, Y_{l,00}$ are the diagonal matrices: $X = [e^{-k_0\mu d}]_{2M\times 2M}, Z_{l,pq} = [k_{l,z,pq}/k_0 n_l^2]_{M\times M}$ and $Y_{l,pq} = [k_{l,z,pq}/k_0]_{M\times M}$ ($l = 1$ and 2 represent the reflected and transmitted side.$[\delta_{00}]_{M\times M}$ is Kronecker delta function matrix.

There is a drawback in calculating the diffracted fields $\vec{E}_{pq}$ and $\vec{H}_{pq}$ for deep gratings. With small exponential value of X, the inverse matrix causes numerical stability in the calculation. This instability can be averted by applying the transmission matrix approach. For the N level grating, the calculations primarily separate X_N^{-1} from the main inverse matrix $[[A]_N^{-1}$.The modified matrix equations can be written as follows

$$\begin{bmatrix} I & 0 & I & 0 \\ 0 & -jZ_{1,0} & 0 & jZ_{1,0} \\ 0 & I & 0 & I \\ -jY_{1,0} & 0 & jY_{1,pq} & 0 \end{bmatrix} \begin{bmatrix} E_{inc,\perp}\delta_{00} \\ j\eta_0 H_{inc,\perp}\delta_{00} \\ E_{r,pq,\perp} \\ j\eta_0 H_{r,pq,\perp} \end{bmatrix} =$$

$$\begin{bmatrix} W_1 & W_1X \\ W_2 & W_2X \\ -V_1 & V_1X \\ -V_2 & V_2X \end{bmatrix} \begin{bmatrix} X & 0 \\ 0 & II \end{bmatrix}_1^{-1} \begin{bmatrix} W_1 & W_1X \\ W_2 & W_2X \\ -V_1 & V_1X \\ -V_2 & V_2X \end{bmatrix}_N \begin{bmatrix} X & 0 \\ 0 & II \end{bmatrix}_1^{-1} \begin{bmatrix} W_1 & W_1 \\ W_2 & W_2 \\ -V_1 & V_1 \\ -V_2 & V_2 \end{bmatrix}_N^{-1} *$$

$$\begin{bmatrix} I & 0 \\ 0 & -jZ_{2,pq} \\ 0 & I \\ -jY_{2,pq} & 0 \end{bmatrix} \begin{bmatrix} E_{t,pq,\perp} \\ j\eta_0 H_{t,pq,\perp} \end{bmatrix} \quad 3.21$$

Where, II is an identity matrix with dimensions $2M \times 2M$. With these modifications, the right side of eq. 3.21 is reduced to $\begin{bmatrix} f \\ g \end{bmatrix}[T]_1$. The matrices $[f]_1$ and $[g]_1$ can be written as

$$\begin{bmatrix} f \\ g \end{bmatrix}_N [T]_N = \begin{bmatrix} W_1 & W_1X \\ W_2 & W_2X \\ -V_1 & V_1X \\ -V_2 & V_2X \end{bmatrix}_N \begin{bmatrix} X & 0 \\ 0 & II \end{bmatrix}_N^{-1} \begin{bmatrix} a \\ b \end{bmatrix}_N T_{N+1}$$

$$= \begin{bmatrix} W_1 & W_1X \\ W_2 & W_2X \\ -V_1 & V_1X \\ -V_2 & V_2X \end{bmatrix}_N \begin{bmatrix} I \\ b_N a_N^{-1} X_N \end{bmatrix} T_N, \quad 3.22a$$

$$\text{And } \begin{bmatrix} a \\ b \end{bmatrix}_N = \begin{bmatrix} W_1 & W_1 \\ W_2 & W_2 \\ -V_1 & V_1 \\ -V_2 & V_2 \end{bmatrix}_N^{-1} \begin{bmatrix} f \\ g \end{bmatrix}_{N+1} \quad 3.22b$$

Substituting $[f]_1 = \begin{bmatrix} f_{1,1} & f_{1,2} \\ f_{1,3} & f_{1,4} \end{bmatrix}$ and $[g]_1 = \begin{bmatrix} g_{1,1} & g_{1,2} \\ g_{1,3} & g_{1,4} \end{bmatrix}$ in Eq. (2.21) the matrix T_1 is written as

$$T_1 = \begin{bmatrix} E_{t,1,\perp} \\ j\eta_0 H_{t,1,\perp} \end{bmatrix} = \begin{bmatrix} g_{1,2} - jY_{1,pq} f_{1,1} & g_{1,4} - jY_{1,pq} f_{1,3} \\ f_{1,2} - jZ_{1,pq} g_{1,1} & f_{1,4} - jZ_{1,pq} g_{1,3} \end{bmatrix} \begin{bmatrix} -2jY_{1,pq} E_{inc,\perp} \delta_{00} \\ 2jZ_{1,pq} \eta_0 H_{inc,\perp} \delta_{00} \end{bmatrix}$$

3.23

Hence, the reflected and transmitted fields can be evaluated as

$$T_{N+1} = \begin{bmatrix} E_{t,pq,\perp} \\ j\eta_0 H_{t,pq,\perp} \end{bmatrix} = a_N^{-1} X_N a_{N-1}^{-1} X_{N-1} a_{N-2}^{-1} X_{N-2} \cdots a_1^{-1} X_1 T_1, \text{ and}$$

$$\begin{bmatrix} E_{r,pq,\perp} \\ j\eta_0 H_{r,pq,\perp} \end{bmatrix} = \begin{bmatrix} f_{1,1}E_{t,1,\perp} + f_{1,3}j\eta_0 H_{t,1,\perp} - E_{inc,\perp}\delta_{00} \\ g_{1,1}E_{t,1,\perp} + g_{1,3}j\eta_0 H_{t,1,\perp} - H'_{inc,\perp}\delta_{00} \end{bmatrix}. \quad 3.24$$

If the power is normalized to $E_{inc,\perp} = \cos\psi$ and $j\eta_0 H_{inc,\perp} = jn_{inc}\sin\psi$, where ψ is the polarization of the incident field into the grating with respect to an axis normal to the plane of incident. The diffraction efficiencies of the reflected waves and transmitted waves can be therefore calculated as

$$DER = \left|E_{r,pq,\perp}\right|^2 Re\left\{\frac{k_{1,z,pq}}{k_{1,z,00}}\right\} + \left|j\eta_0 H_{r,pq,\perp}\right|^2 Re\left\{\frac{k_{1,z,pq}}{n_1^2 k_{1,z,00}}\right\} \quad 3.25$$

$$DET = \left|E_{t,pq,\perp}\right|^2 Re\left\{\frac{k_{2,z,pq}}{k_{1,z,00}}\right\} + \left|j\eta_0 H_{t,pq,\perp}\right|^2 Re\left\{\frac{k_{2,z,pq}}{n_2^2 k_{1,z,00}}\right\} \quad 3.26$$

3.3 Dielectric slab waveguide

Light propagating inside a planar slab waveguide is governed by two conditions: 1) Total Internal Reflection (TIR), and 2) Constructive Interference. TIR happens when the RI of the waveguide is greater than the nearby medium. Light confinement in the guiding region happens when each angle at the interface is greater than the critical angle ($\theta_C = \sin^{-1}(n_2/n_1)$, where n_1 and n_2 are the refractive indices of the neighboring (cover, substrate) and guiding media respectively. Figure 3.4 shows a three-layer structure. The other necessary condition is that the light wave needs to be continuous after bouncing from the two interfaces. That requires that the light wave reflected from the upper film interface to the lower film interface and reflected back to the upper film, accumulates a total phase shift of $2\pi m$, where m is an integer value.

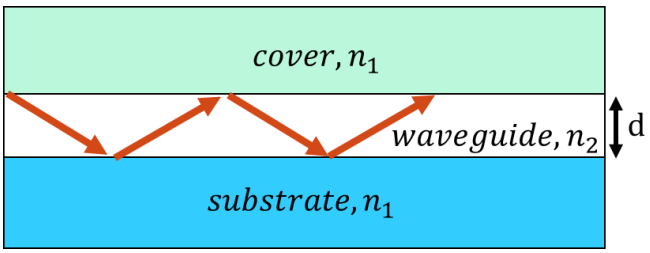

Figure 3.4: Three-layer slab waveguide structure

The constructive interference condition includes discrete values of m for which light is guided inside the dielectric film. Each wave that satisfies this condition is stated as a mode. These discrete modes are called guided modes or bounded modes as they remain bounded inside the film structure. Here, m is the order of the mode. The propagation constant of each mode can be attained by solving the boundary condition inside the structure. Combing the boundary results in what is commonly denoted to as the characteristic equation. The characteristic equation of the slab waveguide is given as (Yariv, 1997)

$$2\kappa_m d - 2\emptyset_s - 2\emptyset_c = 2\pi m \ \ where\ m = 0,1,2, \ldots \qquad 3.27$$

where

$\kappa_m = \sqrt{(k_0 n_f)^2 - \beta_m^2}$ is the transverse propagation constant

$\beta_m = k_0 n_{eff}$, is the modal propagation constant inside the film

n_{eff} is the effective RI of the mode

$2\emptyset_s$ is the phase shift due to the total internal reflection at the film-substrate interface

$2\emptyset_s$ is the phase shift due to the total internal reflection at the film-cover interface

3.3.1 Dielectric grating-waveguide structures

In dielectric grating-based waveguide structures, the permittivity of the waveguide is not uniform as in the case of the slab waveguide as shown in figure 3.5. This causes the guided modes to leak outside the grating structure. Hence, such modes are called leaky modes. Due to this leakage, the power restricted in the guiding region is gradually reduced along the direction of propagation. The leaky mode out of the waveguide layer has a complex propagation constant given by $\beta = \beta' - j\beta''$. The real part, β', indicates light propagation. β'' is the imaginary part that indicates the leakage outside the bounded region. The value $1/\beta'$ is defined as the distance which the leaky mode propagates inside the structure before it becomes strongly attenuated. The value $1/\beta'$ is the minimum size of the GMR structure required for the modes to propagate inside the waveguiding film.

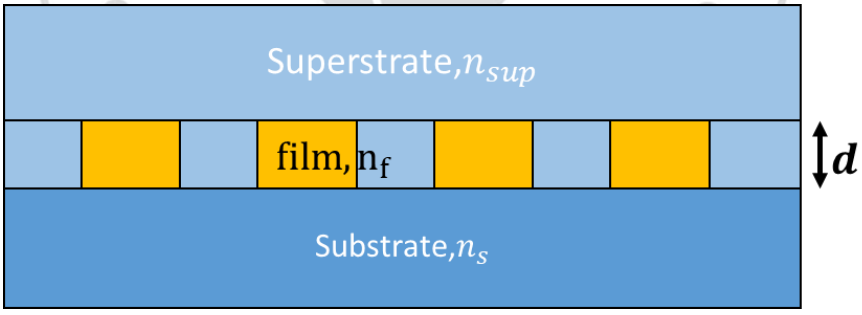

Figure 3.5: Grating waveguide structure

To solve the leaky modes in this form of dielectric grating structure involves taking into consideration the scattered waves along with the guided waves. For such analysis scattering matrix approach is presented which is discussed in the next section.

3.3.2 Scattering matrix approach

The scattering matrix approach is grounded on applying the boundary conditions at the individual boundary of the layer (Cotter et al., 1995). By applying continuity condition of the electric and magnetic fields along the tangential direction from the first (0/1) to the last (N/N+1) layers one can form a resultant scattering matrix. The field equation for the N layers as shown in figure 3.6 can be written as

$$\begin{bmatrix} C_0^- \\ C_{N+1}^+ \end{bmatrix} = [S(\beta)] \begin{bmatrix} C_{N+1}^- \\ C_0^+ \end{bmatrix} \rightarrow [S(\beta)]^{-1} \begin{bmatrix} C_0^- \\ C_{N+1}^+ \end{bmatrix} = \begin{bmatrix} C_{N+1}^- \\ C_0^+ \end{bmatrix} \quad 3.28$$

If there is no external excitation then the array at the right side of equation 3.28 has all zero elements $\left(\begin{bmatrix} C_{N+1}^- \\ C_0^+ \end{bmatrix} = 0\right)$. The solution of the equation then gives us the allowed modes inside the structure.

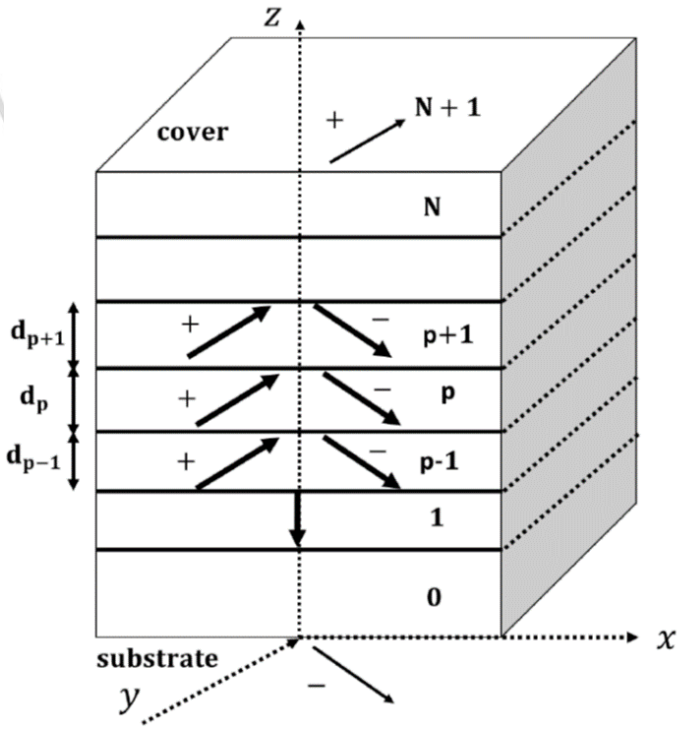

Figure 3.6: Multilayer slab waveguide

$$|S(\beta)^{-1}| = 0 \tag{3.29}$$

In Eq. (3.28), C^- and C^+ are the amplitudes coefficients of the backward propagating waves and forward propagating waves along individual layer, where -0 and $-N+1$ denote the substrate and cover layers respectively.$|S^{-1}|$ represent the determinant of the inverse of the S-matrix.

Formulation of the S-matrix is performed by determining scattered fields along individual layer by solving the coupled-wave equations (3.14) to (3.19). For the interference of layers -a and -b, the S-matrix is arranged as

$$\begin{bmatrix} C_a^- \\ C_b^+ \end{bmatrix} = [S_{ab}] \begin{bmatrix} A_{ab} & B_{ab} \\ C_{ab} & D_{ab} \end{bmatrix} \tag{3.30a}$$

$$A_{ab} = [(V_b^{-1}V_a + W_b^{-1}W_a)^{-1}(2X_b)] \tag{3.30b}$$

$$B_{ab} = [(V_b^{-1}V_a + W_b^{-1}W_a)^{-1}(V_b^{-1}V_aX_a + W_b^{-1}W_aX_a)] \tag{3.30c}$$

$$C_{ab} = [(V_b^{-1}V_a + W_b^{-1}W_a)^{-1}(V_b^{-1}V_bX_b - W_a^{-1}W_bX_b)] \tag{3.30d}$$

$$D_{ab} = [(V_b^{-1}V_a + W_b^{-1}W_a)^{-1}(2X_a)] \tag{3.30e}$$

Where, the matrices $[W], [V], [X]$ are defined in Section 3.1.3. The final S-matrix is shown below which is a product of all the sub-S matrices of respective layers

$$[S] = [S_{0,1}] * [S_{1,2}] * \dots * [S_{N,N+1}] \tag{3.31}$$

The S-matrix multiplication is defined as

$$[S] = [S_{ab}] * [S_{bc}] = \begin{bmatrix} A & B \\ C & D \end{bmatrix} \tag{3.32a}$$

$$A = \{(A_{ab}A_{bc}) - (A_{ab}B_{bc})(C_{ab}B_{bc} - I)^{-1}(C_{ab}A_{bc})\} \quad 3.32b$$

$$B = \{(B_{ab}) - (A_{ab}B_{bc})(C_{ab}B_{bc} - I)^{-1}(D_{ab})\} \quad 3.32c$$

$$C = \{(C_{ab}) - (D_{bc}C_{ab})(B_{bc}C_{ab} - I)^{-1}(A_{ab})\} \quad 3.32d$$

$$D = \{(D_{bc}D_{ab}) - (D_{bc}C_{ab})(B_{bc}C_{ab} - I)^{-1}(B_{bc}D_{ab})\} \quad 3.32e$$

The S-matrix is solved for complex solutions of β_p, where $\beta_p = \left(\beta' - p\frac{2\pi}{\Lambda}\right) - j\beta''$ with a grating period Λ.The guided modes are considered to be the ones that have the real part of propagation constant within the range $\max\left[k_0 n_{superstrate}, k_0 n_{substrate} < |\beta'| < k_0 n_{high\ index\ film}\right)$.If the mode has zero imaginary part then it is a bound mode inside the waveguide otherwise it is a leaky mode.

3.4 Principle of GMR

A GMR structure typically consists of a diffraction grating ($effective\ index = n_g$) and a waveguide (n_f) in close proximity to each other. The high index layer (n_f) is the main guiding region as shown in figure 3.7. At resonance condition, the waves diffracted by the grating layer are phase matched to a waveguide mode. The mode is bounded inside the waveguide, however, due to the grating it is leaky in nature and transforms into a leaky mode. At a specific wavelength, the leakage in the incident region constructively interferes with the zero-order resulting in a peak at the reflected side. This wavelength value is called peak wavelength value (PWV,λ_0) as illustrated in figure 3.8(a). To achieve 100% diffraction efficiency at the resonance condition, the period of the grating must be in the subwavelength range and should mainly diffract first-order waves inside the grating.

Figure 3.7: Coated dielectric grating GMR structure

The phase matching condition between the waveguide mode and the first order diffracted wave is given as

$$\beta' \approx k_{diff,1^{st}} \tag{3.33}$$

where $k_{diff,1^{st}}$ is the wave vector of the tangential component for the first-order diffracted wave, which relies on the direction of the incident beam and on the grating vector as explained in Section 3.1.The position of the resonance can be calculated when the modal propagation constant (β') is identified from the 1-D grating equation (3.3) or from the 2-D grating equations (3.4)-(3.8).The modal propagation constant is dependent on the modal effective index that is a function of the RI on the GMR cover region (superstrate, n_{sup}). The variation in the superstrate RI from n_{sup_1} to n_{sup_2} outcomes in a variation in the PWV as shown in figure 3.8 (b).

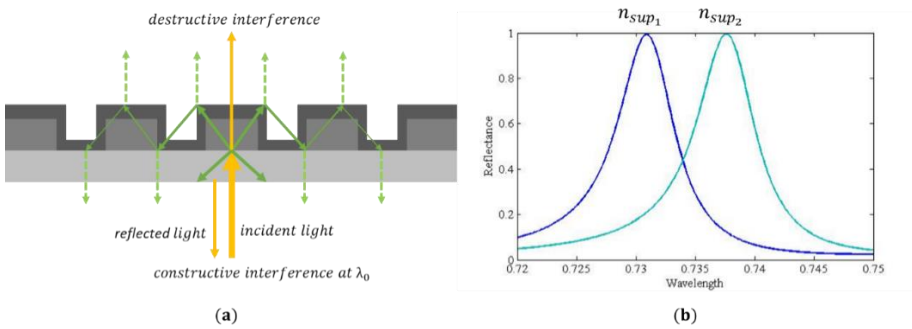

Figure 3.8: (a) Constructive interference at the reflection side in GMR structure

(b) PWV change due to variation in superstrate RI from n_{sup_1} to n_{sup_2}

The exact location of the resonant wavelength and the diffraction efficiency can be calculated using RCWA.

3.5 Spectrometer Design Approach

The design of the in-house spectrometer starts by the calculation of the diffraction angle that is defined by the grating period. The diffraction angle varies with the wavelength. Hence, it is important to evaluate the angular width for a desired spectrum range. The spectrum range for visible light is 450 nm to 650 nm, which is considered in this thesis for calculating the angular width. Figure 3.9 displays the ray drawing of the spectrometer design.

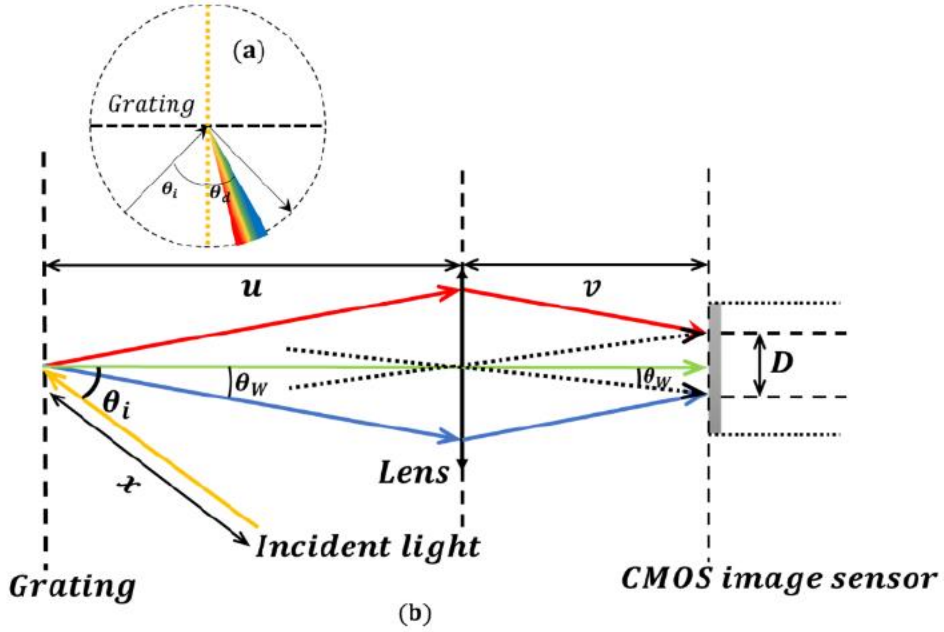

Figure 3.9: (a) Diffraction of light into angle θ_d from the grating layer (b) Ray tracing approach for spectrometer design

Figure 3.9 shows light, incident at an angle θ_i to a reflective grating with a period Λ. The number of diffraction orders can be controlled by the period of the grating. The number of diffraction order increases with the period. The grating diffracts light with an angle θ_d as shown in figure 3.9a. The relationship between θ_i and θ_d for a particular grating period Λ and a wavelength λ is given by

$$\theta_d = \sin^{-1}\left[m\left(\frac{\lambda}{\Lambda}\right) - \sin\theta_i\right] \qquad 3.34$$

where m is the order of diffraction, θ_d is relying on λ and inversely reliant on the period Λ. For a spectral range such as visible spectrum the angular width of diffraction is given as θ_w. θ_w is the variance between diffraction angles of $\theta_{d,r}(blue)$ and $\theta_{d,b}(red)$ given in equation 3.35.

$$\theta_w = \theta_{d,r} - \theta_{d,b} \quad 3.35$$

The object image is established for individual wavelength and the convolution of the object image and the spectrum of light is the resultant image which is recorded by the CMOS image sensor. The distance from the object to the lens is called object distance u and from lens to CMOS image sensor is called imaging distance v.The relation between v and θ_w is given by

$$v = \left(\frac{1}{\tan\theta_w}\right) \times D/2 \quad 3.36$$

Here, D is the CMOS image sensor width. The value of $d = (x + u)$ can be computed by means of the thin lens equation $1/f = 1/v + 1/d$, for a lens of focal length f. The magnification m can be computed as

$$m = \frac{D/2 - (\tan\theta_w \mathrm{x} f)}{(\tan\theta_w \mathrm{x} f)} \quad 3.37$$

CHAPTER 4

GUIDED MODE RESONANCE NEAR CUT OFF CONDITION

In this chapter the super mode excitation in 1D and 2D GMR structures is analyzed. Various multilayer GMR structures are proposed and the structural parameters are varied in order to achieving super mode excitation at cut off wavelengths (Rayleigh wavelengths).

4.1 Rayleigh anomaly in dielectric waveguide structure

Plasmonic resonances at Rayleigh wavelength are applied for bulk RI sensing where the sensitivity achieved equals to the theoretical limit. However, GMR structure such as a dielectric grating waveguide has not utilized the Rayleigh anomaly before to increase the structure sensitivity.

RA corresponds to a distributed wave tangential (illustrated by the red arrow in figure 4.1) to the grating surface. By properly selecting a multilayer GMR structure excitation of resonance at super-mode for the first diffraction order at Rayleigh wavelength is possible. Such a super-mode has an extended field towards the sensing region resulting in enhanced sensitivity close to the theoretical limit. Advantages of RA are that the sensitivity solely relies on the grating period and the PWV at resonance is linearly proportional to the superstrate's RI.

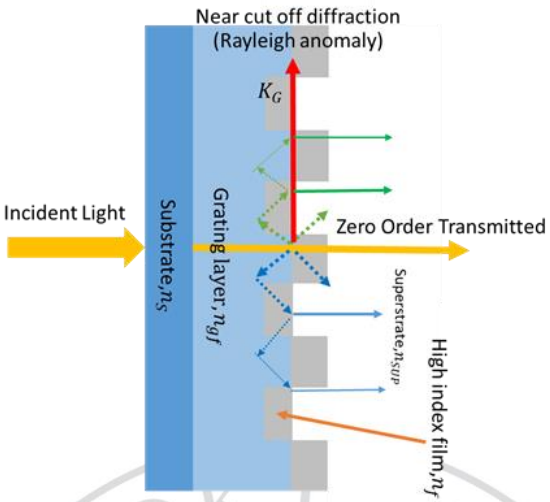

Figure 4.1: Concept of super-mode excitation at Rayleigh wavelength (cut-off wavelength)

4.2 Analysis of Super-mode excitation in 1-D GMR structure

For the analysis of super mode excitation in 1D GMR three structures are proposed as shown in figure 4.2. The design of the structure is such that a film of RI n_g is coated on top of a substrate with RI n_s.The unit cell of the structure has a period of Λ. A high RI film (n_f) is deposited on the grating layer. Structure 1 is divided into four uniform layers having thicknesses $t_f, t_{sgf}(t_g - t_f), t_f and\ t_C$ with effective refractive indices of these layers as n_{sf}, n_{sgf}, n_{gf} and n_g respectively as shown in Fig.4.2. Here n_{sf} is calculated as a combination of the superstrate RI n_{sup} and the film RI, n_f, reliant on the grating's filling factor. n_{sgf} is a combination of $n_{sup,}n_f$ and n_g.Lastly n_{gf} relies only on n_g and n_f.When the superstrate is presented with an aquatic solution $(n_{sup} \approx 1.33)$, the RI values of n_{sf} and n_{gf} can be comparatively close to each other which makes both layers form a guiding regions. Structure 2 has three layers with

thickness $t_f, t_g \; and \; t_C$ and effective refractive indices n_{sf}, n_{gf}, n_g as shown in the figure .Structure 3 has four layers $t_{sf}, t_f, t_g, and \; t_c$ and effective refractive indices n_{sf}, n_f, n_{gf}, n_g. Each of the structure is formulated with three conditions (1) $t_f < t_g \; and \; t_f < W/2$ (2) $t_f < t_g \; and \; t_f > W/2$ (3) $t_f > t_g \; and \; t_f < W/2$ where W = *fill factor (ff) × grating period (Λ).*

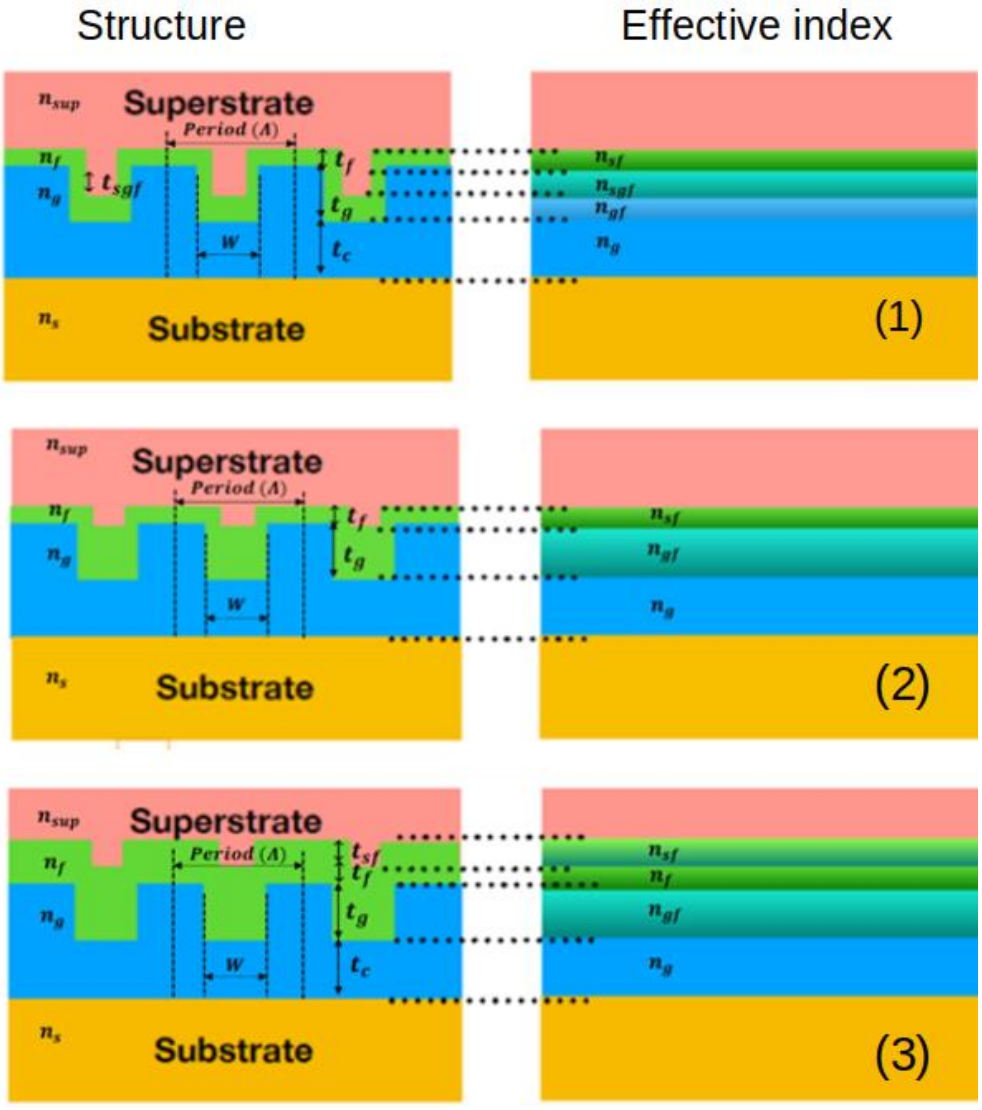

Figure 4.2: The three GMR configurations.

4.3 Super-mode excitation at near cut-off diffraction

In the proposed structure, the existence of two guiding layers close to each other causes the modes excited in each individual layer to possibly couple. The mode coupling between the two guiding regions with refractive indices n_{sf} and n_{gf} makes the super-mode excitation possible. Nevertheless, traditional guided mode is mostly confined in the region with highest RI (i.e n_{gf}), one of the excited super-modes at resonance can have more power confinement in the film with lower RI (n_{sf}).The presence of such super mode at resonance, with longitudinal wave number β having values between $k_0 n_{sup}$ and $k_0 n_{sf}$, permits high leakage of power into the superstrate region. Such a super mode at resonance can result in high sensitivity with the variations in the superstrate region. Here, k_0 is the free-space wave number.

$$\beta \approx m\frac{2\pi}{\Lambda} \approx k_0 n_{sup} + \delta \qquad 4.1$$

Where β is the longitudinal propagation constant, Λ is the grating period of the GMR structure, k_0 is a wave number in vacuum, n_{sup} is the RI of the superstrate region, and δ is the slight discrepancy in the condition of phase matching. At cut-off diffraction when $m_{c.o}K_G = k_0 n_{sup}$ where $K_G = \frac{2\pi}{\Lambda}$ and $m_{c.o}$ is the order of diffraction in the region of superstrate at cut-off condition. The Rayleigh wavelength or cut-off value of wavelength $\lambda_{c.o}$, is attained as follows

$$\lambda_{c.o} \approx n_{sup}\frac{\Lambda}{m_{c.o}} \qquad 4.2$$

4.4 Sensitivity enhancement at near cut-off diffraction

According to equation 4.2, if the super-mode at resonance is excited at a wavelength $\lambda_{c.o}$, the attained sensitivity due to variations of n_{sup} in relations of nanometre per refractive index unit (RIU) is

$$\frac{\partial \lambda_{c.o}}{\partial n_{sup}} \approx \frac{\Lambda}{m_{c.o}} \qquad 4.3$$

This gives the maximum normalized sensitivity, $S = \left(\frac{\partial \lambda_{c.o}}{\partial n_{sup}}\right)\left(\frac{\lambda_{c.o}}{n_{sup}}\right) = 1$.In order to reach such upper limit, the structure's parameters need to be designed for the resonance to be satisfied at the cut-off wavelength or very close to the cut-off wavelength, $\lambda_{c.o}$ for the first diffraction order $m_{c.o} = 1$. Equations 4.2 and 4.3 illustrates that the resonance wavelength at cut-off is linearly proportional to the period of the grating and RI of the superstrate region. This assures that the device sensitivity can nearly be equivalent to the period of the grating at the first order diffraction.

4.4.1 1-D GMR device optimization

To achieve maximum reflectance at $\lambda_{c.o}$, the dimensions of the device such as the filling factor of the grating, the grating thickness, and the film thickness are required to be optimized in order to excite a super mode near to the cut-off condition at $m_{c.o} = 1$. The resonance mode under such a condition has a modal effective index that is equivalent to the superstrate's RI. The variations in the superstrate index, n_{sup}, directly alter the modal properties and hence the resonance condition.

4.4.2 Super-mode excitation at near cut-off diffraction in 1-D structure

The spectra for super-mode resonance are visualized and calculated in structures 1, 2, and 3 at conditions of near cut-off for various superstrate indices and field distributions using RCWA. The light is considered to be incident normally from the substrate side in all the calculations. The device structure is designed in such a way that the diffraction of first order phase matches with the excited super-mode at resonance at near cut-off state in the superstrate region that is formed by a solution with RI close to water. For that, the structure dimensions are selected such that Λ is set to 440 nm and the other structural parameters t_g, t_f, and t_c and ff are varied. The structure under consideration for the design has refractive indices of $n_g = 1.4$, $n_{gf} = 1.4$ and $n_f = 2.1$ and $n_s = 1.5$. The RCWA simulations of the resonance spectra obtained by changing the refractive indices for the different structures are explained in the sections below. The device response when varying the RI of the superstrate region from 1.33 to 1.35 is shown in figure 4.3(a). The resonance response has two categories: traditional mode $(TM_{0,guided})$ and super mode ($TM_{0,super}$ at near cut-off wavelength). The GMR due to matching of $TM_{0,guided}$ to the first diffraction orders in the case of water superstrate, is referred to as traditional mode, occurs at longer wavelengths (λ_1, λ_2 and λ_3 in figure 4.3(a) for $n_{sup} = 1.33$). The field distribution in the figure 4.3 (b) for TM_0 guided mode at λ_1 displays clearly that the light is restricted in the layer with the highest RI (n_{gf}) with a very small extension into the superstrate, which is the sensing region. The resonance peaks due to the matching of the phase between the guided modes and the diffraction order has a Lorentzian shape. This is shown in figure 4.3(a) by the peaks

labeled $\lambda_1, \lambda_2$and λ_3. At shorter wavelengths other resonances seem to present as shown in the figure. Two peaks (λ_1 and λ_2) appear to experience nominal variation with the modification of the superstrate index n_{sup}.These two peaks are the result of matching $TM_{0,guided}$ to higher diffraction orders. However, the graph displays the existence of a low confinement mode in figure 4.3 (c) that appear to follow $\lambda_{c.o}$, i.e., the first diffraction order cut-off wavelength, when $m_{c.o}$=1 in equation (4.2).

Resonance occurring at higher RI values at the superstrate region (n_{sup}=1.33-1.35), is the outcome of phase match between the super mode ($TM_{0,super}$) and the first order of diffraction. The PWV at resonance shifts toward the cut-off condition in Eq. (4.2) resulting in an upper limit of sensitivity, S=1. Figure 4.3 (a) clearly shows the larger shift in the peak wavelength value ($\lambda_{c.o_1}$ for $n_{sup} = 1.33$ and $\lambda_{c.o_2}$ for $n_{sup} = 1.35$) as compared to traditional modes ($\lambda_1, \lambda_2$and λ_3). At high n_{sup} values, the sensitivity of the structure at cut-off wavelength increases considerably as related to guided mode. This is due to the low confinement of the mode at near cut-off wavelength ($\lambda_{C.O}$) as displayed in figure 4.3 (c). This is related to the traditional guided mode, where light is mostly confined in the film (n_{gf}) with highest RI. The PWV at cut-off condition from the reflection spectrum is at 585.2 nm for $n_{sup} = 1.33$ which is shifted to 594nm when n_{sup} increases to 1.35 $\left(\Delta\lambda/\Delta n = \frac{4.4}{0.01} = 440\ nm/RIU\right)$.This corresponds to equation (4.3) for the first order ($m_{c.o} = 1$).The sensitivity attained is proportional linearly to the grating period, and it equals the grating period for the first order of diffraction. The grating period and film thickness still need to be adjusted to

guarantee modal excitation in the immediacy of the condition at cut-off wavelength.

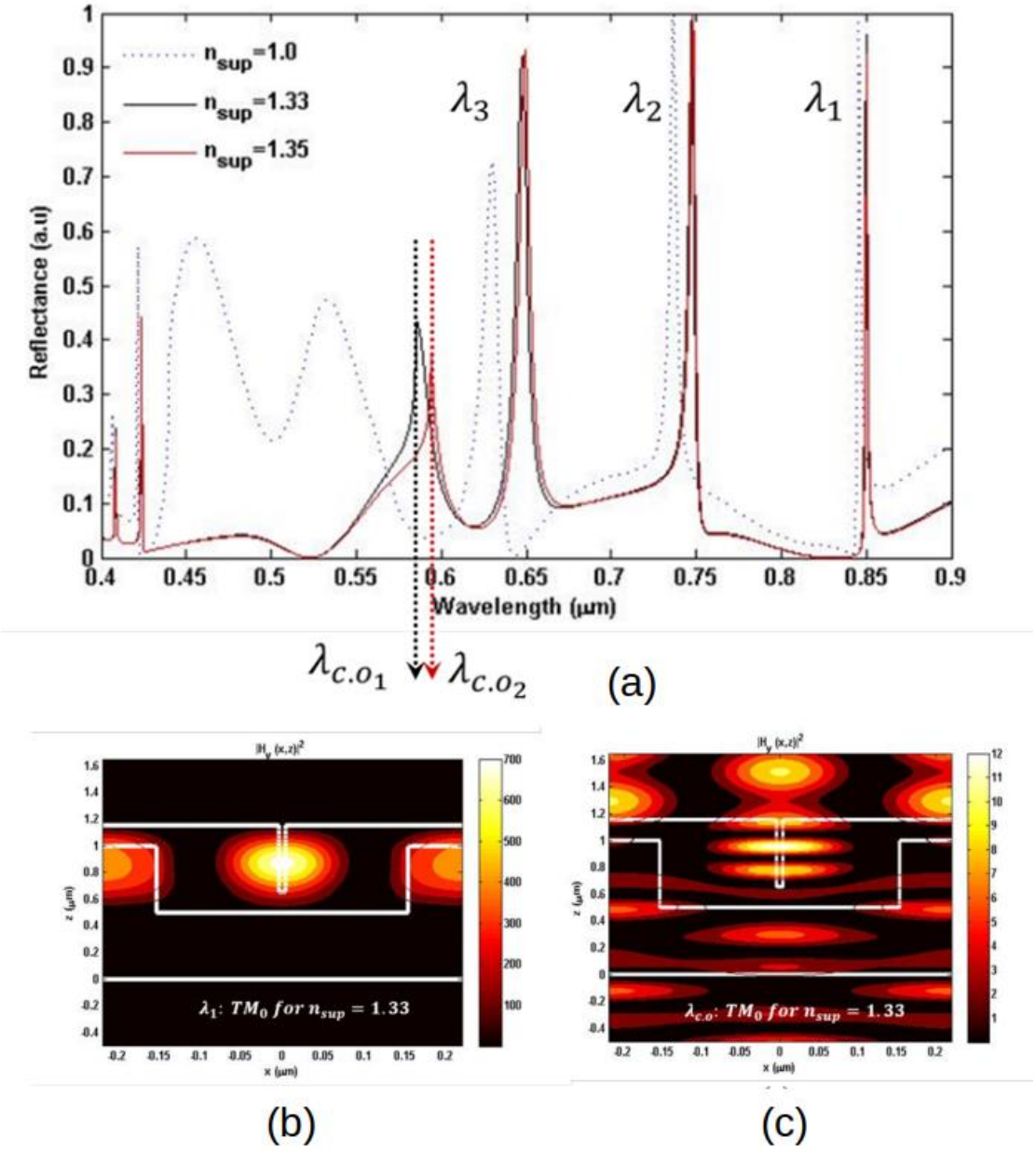

Figure 4.3: (a) Calculated reflectance spectrum for three superstrate values (b) Field distribution of traditional mode and (c) super mode matching at near cut-off wavelength for n_{sup}=1.33.

4.4.3 Maximization of reflectivity at cut-off diffraction

The reflectivity at the cut-off wavelength for the device is increased by selecting the optimal grating period and film thickness using water $(n_{sup} = 1.33)$ as superstrate. Different combinations of t_g, t_f, ff for structure 1,2 and 3 is done and the reflectivity at cut-off resonance is studied. At phase matching condition in Eq. (4.1) maximum reflectance occurs at an optimum condition.

a) Optimization for structure 1 ($t_f < t_g$ and $t_f < W/2$):

The following table shows the parameters selection for optimization of the first structure in order to achieve maximum reflectivity near cut-off. In spite the fact that the reflection spectrum for all the parameters in table 4.1 is calculated, a selection of these results is visually demonstrated in this chapter for simplicity.

Table 4.1: Device parameters for structure 1.

	$filling\ factor\ (ff)$	$Thickness\ of\ film\ (t_f) nm$	$Thickness\ of\ grating\ (t_g) nm$
STRCTURE 1	0.35	70	250-650
	0.4	80	250-650
	0.45	69-99	250-650
	0.5	70-100	250-650
	0.55	80-120	250-650
	0.6	80-130	250-650
	0.65	70-140	250-650

Table 4.1(Continued): Device parameters for structure 1.

0.7	100-150	250-650
0.75	90-160	250-650

Figure 4.4 displays the calculated reflectance of structure 1 when varying the grating thickness from 250 nm to 650 nm while fixing the filling factor ff=0.35. The calculations were performed for several values of the film thickness: t_f = 70 nm, 80 nm, 90 nm, 100 nm ,110 nm and 120 nm.

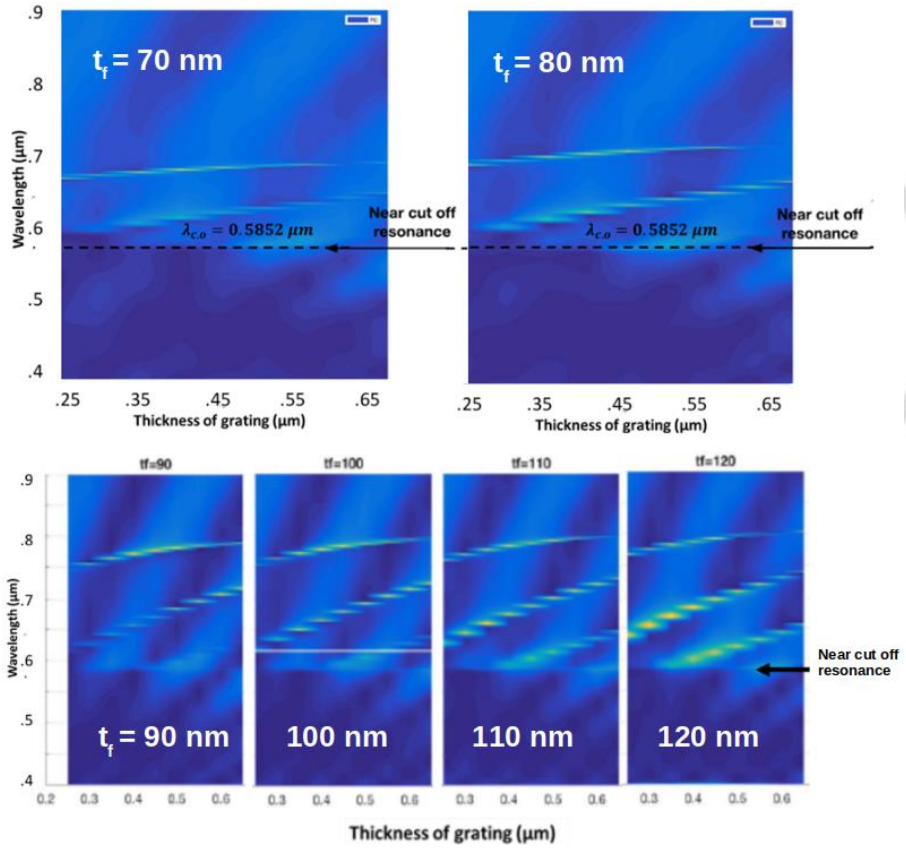

Figure 4.4: Calculated reflectance when varying t_g from 250 to 650 nm and fixing ff=0.35 for t_f values of 70 nm, 80 nm, 90 nm, 100 nm and 110 nm.

To examine the effect of volume fraction, figure 4.5 shows the contour plots when increasing ff to 0.55 for film thickness values of tf = 90, 100,110 and 120 nm.

The contour plots in figures 4.4 and 4.5 show an increase in the reflectance for the reflectance intensity at the cut-off wavelength ($\lambda_{c.o.} \cong$ 585 nm) as the film thickness increases particularly around the grating thickness of t_g = 500 nm.

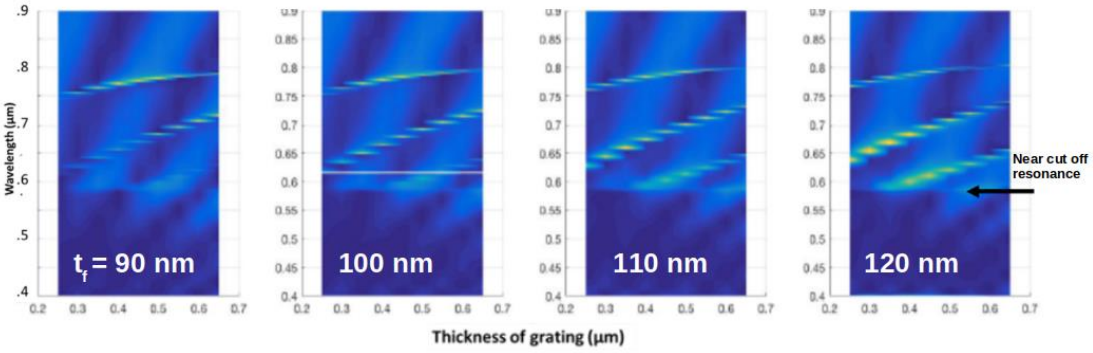

Figure 4.5: Calculated contour plot for reflectance of ff=0.55, t_f= 90,100,110 and 120 nm while varying t_g=250-650 nm.

In the following contour plots in figure 4.6, the film thickness rises from 120 nm to 150 nm at a higher ff of 0.7.

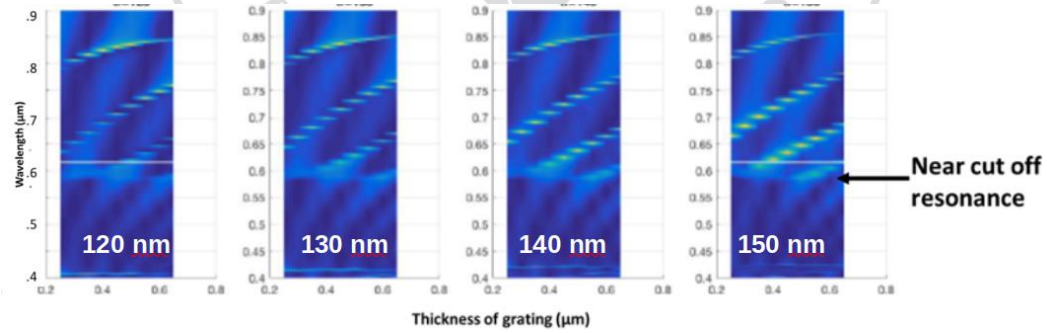

Figure 4.6: Calculated contour plot for reflectance of ff=0.7, t_f= 120,130,140 and 150 nm while varying t_g=250-650 nm.

Finally, the reflectance is calculated for film thickness up to 160 nm at ff of 0.75 as displayed in figure 4.7.

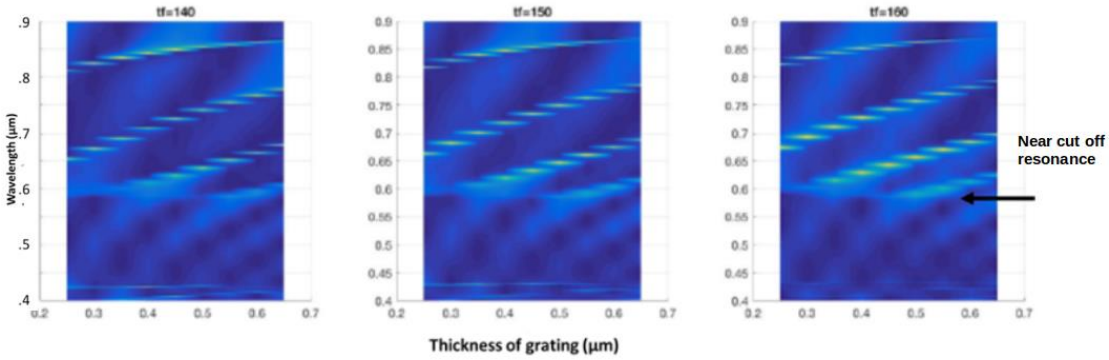

Figure 4.7: Calculated contour plot for reflectance of ff=0.75, t_f= 140,150 and 160 nm while varying t_g=250-650 nm.

From the optimization results it is found that the maximum reflectance intensity (43%) is achieved for the values of $ff = 0.7, t_g = 500\ nm, t_f = 150\ nm$.The normalized sensitivity is calculated by changing the RI of superstrate from 1.33-1.35 and it was found to be 440nm/RIU which is equal to the maximum theoretical limit. Figure 4.8 shows the resonance shift (red dotted line) at cut off wavelengths for different refractive indices.

The reflectance intensity for this structure reduces with the increase of the RI. Hence such a structure cannot be a proper choice for sensing in aqueous medium. Further, the second structure is optimized and the maximum reflectance and response is calculated as in the next subsection.

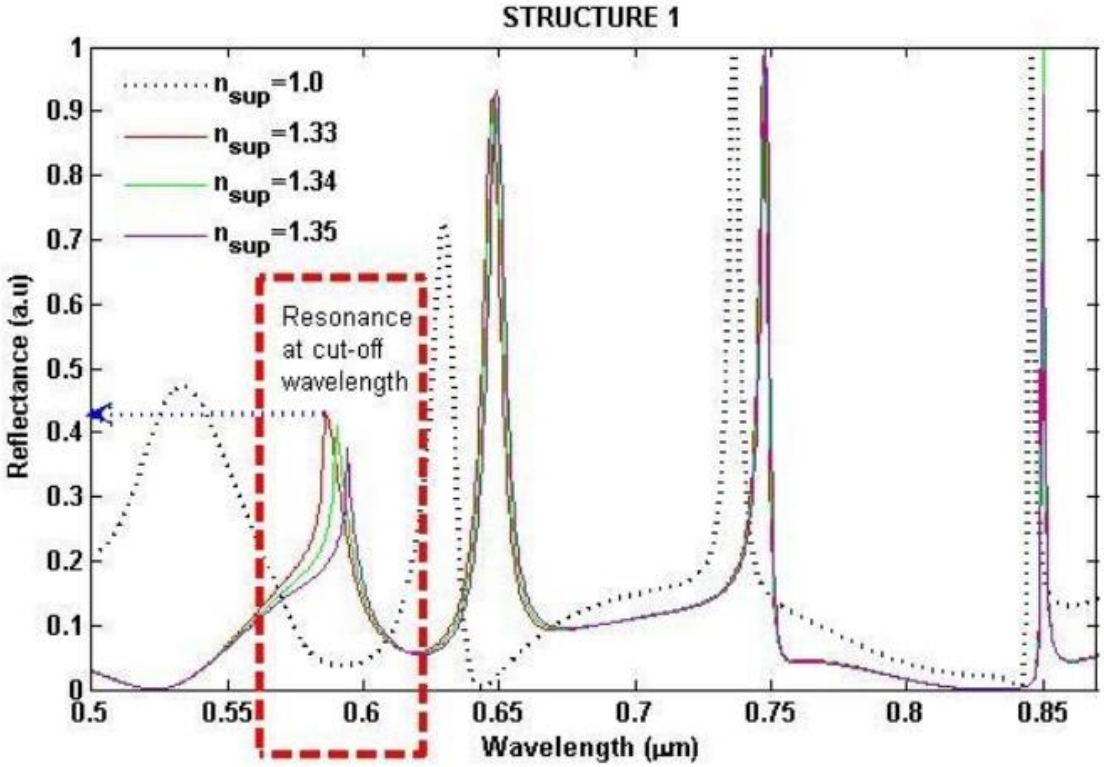

Figure 4.8: Shift of resonance at cut-off wavelength for superstrate refractive indices varied from 1.33 to 1.35. The maximum reflectance intensity achieved is 43 % (shown as blue dotted arrow).

b) Optimization for structure 2 ($t_f < t_g$ and $t_f > W/2$):

Table 4.2 displays the parameters selection for optimization of the second structure in order to achieve maximum reflectivity near cut-off. In spite the fact that the reflection spectrum for all the parameters in table 4.1 is calculated, a selection of these results is visually demonstrated in this chapter for simplicity.

Table 4.2: Device parameters for structure 2.

	$filling\ factor\ (ff)$	$Thickness\ of\ film\ (t_f)nm$	$Thickness\ of\ grating\ (t_g)nm$
STRCTURE 2	0.45	100-160	250-650
	0.5	100-240	250-650
	0.55	121-241	250-650
	0.6	132-242	250-650
	0.65	144-244	250-650
	0.7	154-244	250-650
	0.75	165-245	250-650

Figure 4.9 below shows the contour plots for the reflectance spectra for film thicknesses of 140 nm, 150 nm and 160 nm at a filling factor, ff = 0.45 when varying, t_g varying from 250-650 nm.

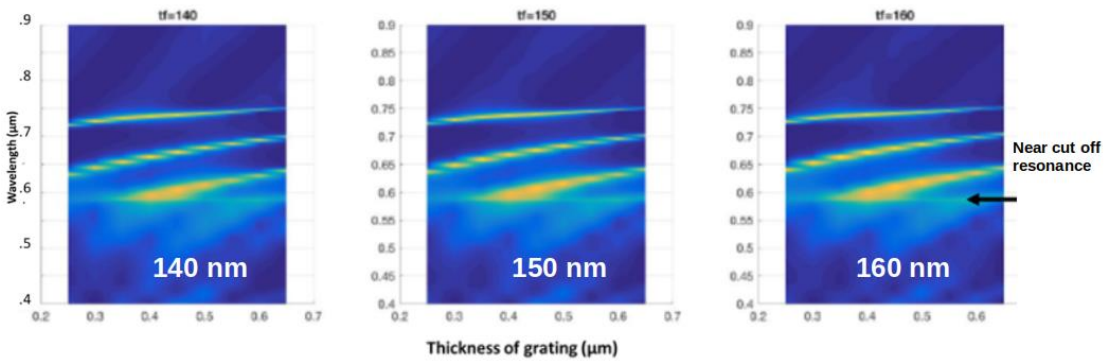

Figure 4.9: Calculated contour plot of reflectance for structure 2 at ff=0.45, t_f= 140,150 and 160 nm while varying t_g=250-650 nm.

The plots in figure 4.9 show that the near cut-off resonance occurs around the wavelength of 585.2 nm. Increasing the thickness and ff to 0.5 we obtain the following

contour plots in figure 4.10.

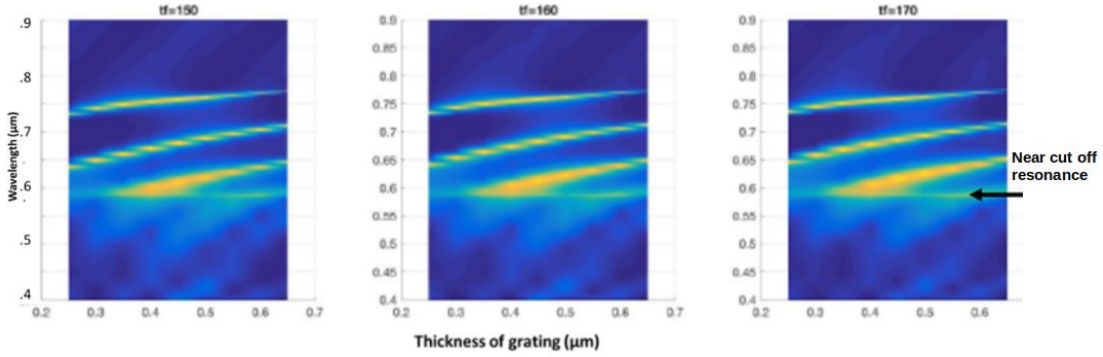

Figure 4.10: Calculated contour plot of reflectance for structure 2 at ff=0.5, t_f= 150,160 and 170 nm while varying t_g=250-650 nm.

The plots in figure 4.10 show the reflectance when varying the film thickness from 171 to 231 nm at ff =0.55 for the second structure.

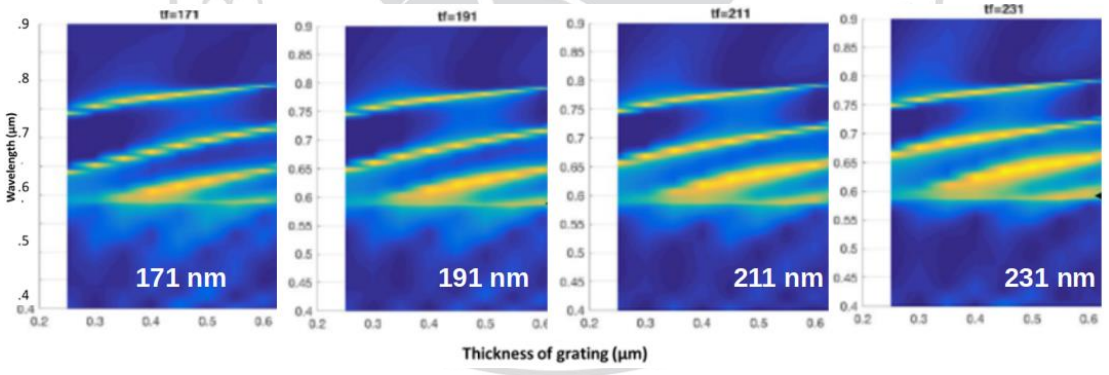

Figure 4.11: Calculated contour plot of reflectance for structure 2 at ff=0.55, t_f= 171,191, 211 and 231 nm while varying t_g=250-650 nm.

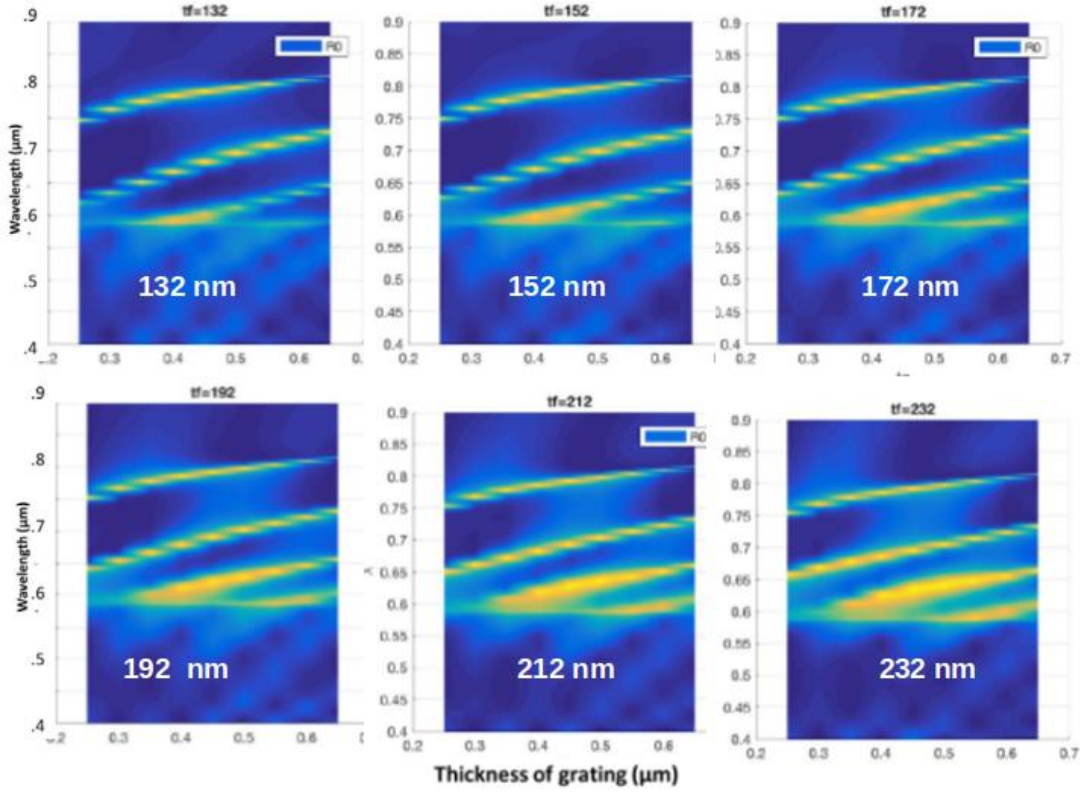

Figure 4.12: Calculated contour plot of reflectance for structure 2 at ff=0.6, t_f from 132 to 232 nm while varying t_g=250-650 nm.

For a high ff = 0.7 the following plots are generated.

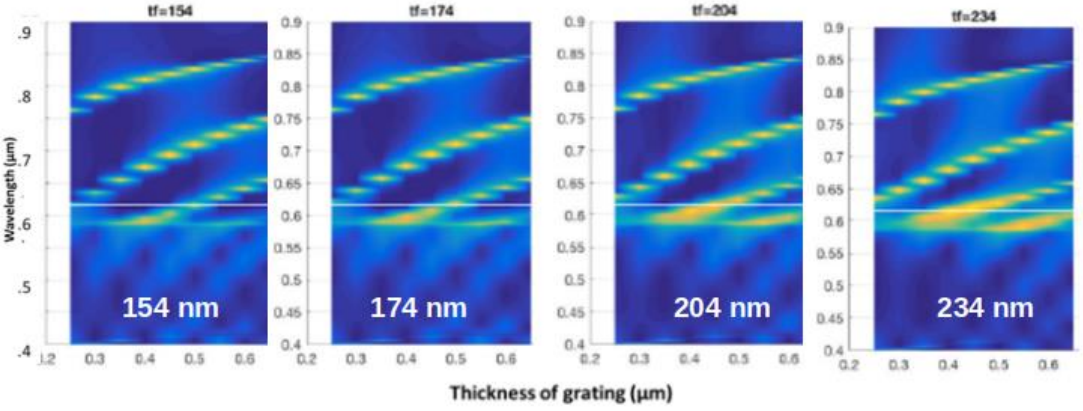

Figure 4.13: Calculated contour plot of reflectance for structure 2 at ff=0.7, t_f from 154 to 234 nm while varying t_g=250-650 nm.

From the optimization results it is found that the maximum reflectance intensity (81%) achieved for the values of $ff = 0.5, t_g = 400\ nm, t_f = 110\ nm$.The normalized sensitivity is calculated by changing the RI of superstrate from 1.33-1.35 and it was found to be 440nm/RIU which is equal to the maximum theoretical limit. Figure 4.14 shows the resonance shift (red dotted line) at cut off wavelengths for different refractive indices.

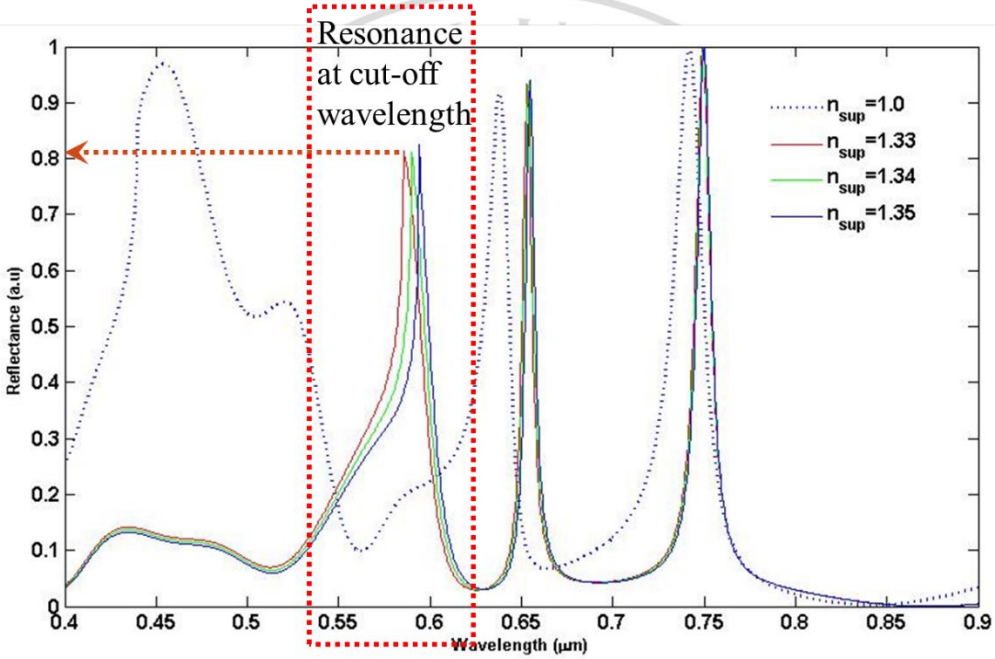

Figure 4.14: Shift of resonance at cut-off wavelength for superstrate refractive indices varied from 1.33 to 1.35. The maximum reflectance intensity achieved is 43 % (shown as blue dotted arrow).

The reflectance intensity for this structure remains almost the same with the increase of RI. This structure can then be a choice for sensing in aqueous medium. However, such deep grating requires sophisticated fabrication procedure. Hence,

structure 3 is optimized and the reflectance intensity is calculated.

c) Optimization for structure 3 ($t_f \geq t_g \; and \; t_f \geq W/2$):

Table 4.3 displays the parameters selection for optimization of the third structure in order to achieve maximum reflectivity near cut-off. In spite the fact that the reflection spectrum for all the parameters in table 4.3 is calculated, a selection of these results is visually demonstrated in this chapter for simplicity.

Table 4.3: Device parameters for structure 3.

	$filling\ factor\ (ff)$	$Thickness\ of\ film\ (t_f) nm$	$Thickness\ of\ grating\ (t_g) nm$
STRCTURE 3	0.45	150-600	250-650
	0.5	150-600	250-650
	0.55	150-600	250-650
	0.6	150-600	250-650
	0.65	150-600	250-650
	0.7	150-600	250-650
	0.75	150-600	250-650

For the structure 3, the calculation results showed that only one configuration of parameters seemed to excite the near cut-off resonance. The other optimizing parameters did not excite the near cut off mode. Hence, only one contour plot is revealed in figure 4.15

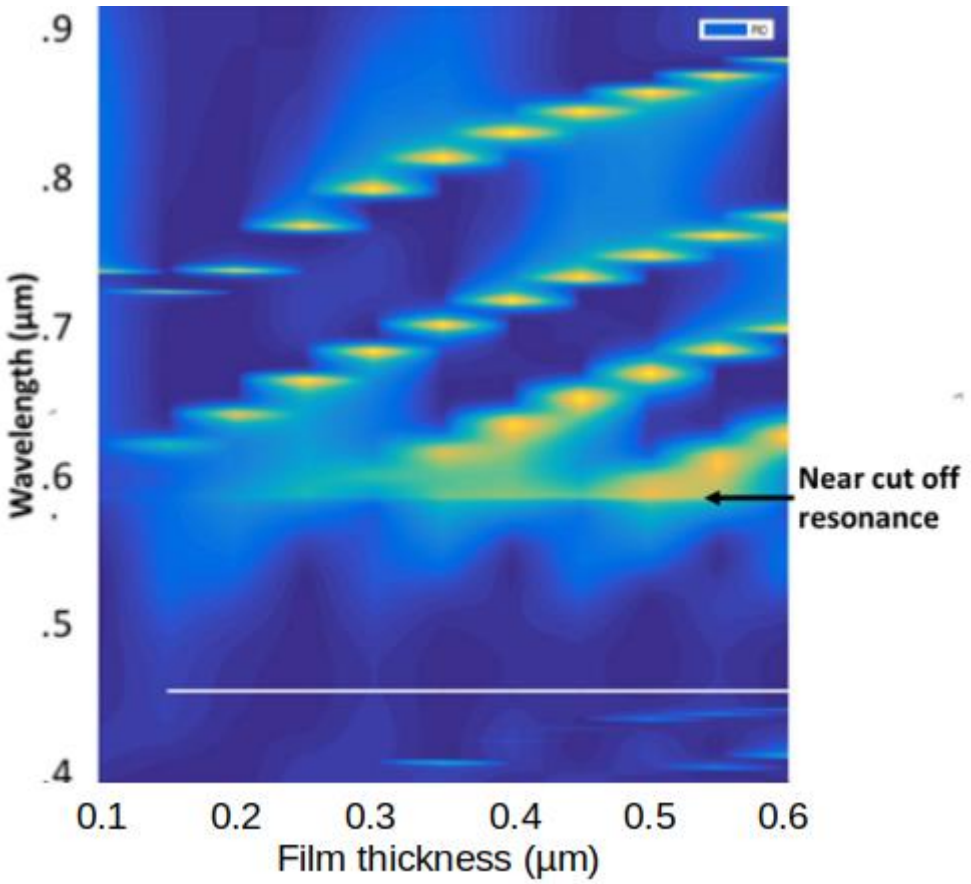

Figure 4.15: Calculated contour plot of reflectance for ff=0.5, t_g=200 nm, t_f varying from 150-200 nm, near cut-off super mode is shown at 585.2 nm.

From the optimization results it is found that the maximum reflectance intensity (81%) achieved for the values of $ff = 0.5, t_g = 200\ nm, t_f = 500\ nm$.The normalized sensitivity is calculated by changing the RI of superstrate from 1.33-1.35 and it was found to be 440nm/RIU which is equal to the maximum theoretical limit. Figure 4.16 shows the resonance shift (red dotted line) at cut off wavelengths for different refractive indices.

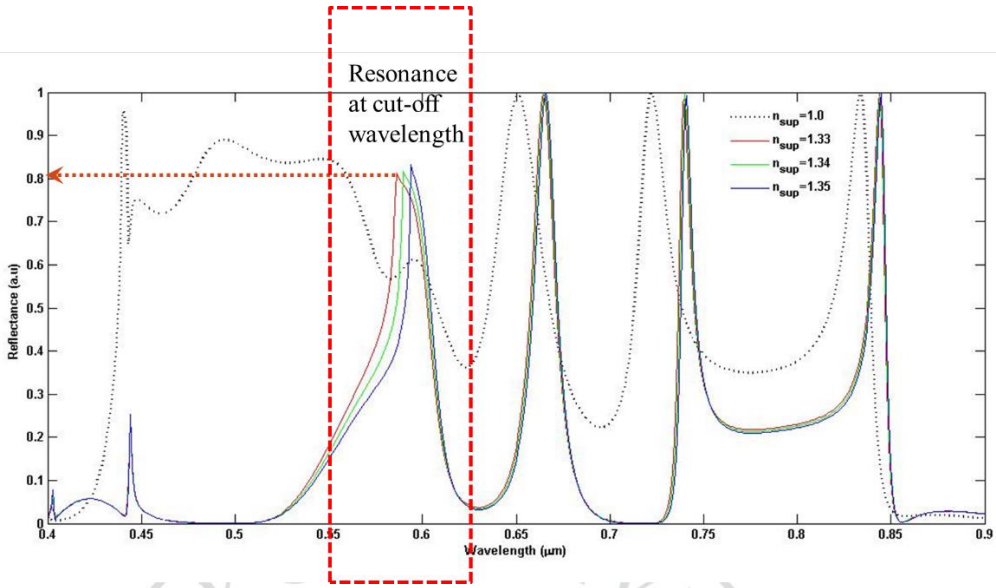

Figure 4.16: Shift of resonance at cut-off wavelength for superstrate refractive indices varied from 1.33 to 1.35. The maximum reflectance intensity achieved is 43 % (shown as blue dotted arrow).

4.5 Summary

Optimization of all the three structures depicted that the super mode excited at cut-off wavelength (Rayleigh wavelengths) had values of 585.2 nm, 589.6 nm and 594 nm for refractive indices of n_{sup}=1.33, 1.34, 1.35 irrespective of changing ff, t_g, t_f.This satisfied the condition of Rayleigh anomaly of excitation. Changing the values of fill factor, grating thickness and thickness of film only resulted in the increase of the reflectance intensity at cut-off wavelengths. Structure 2 and structure 3 showed the highest reflectance of around 80% whereas the structure 1 has a maximum of 40%. In structure 2, a deeper grating with a grating thickness of $t_g = 400\ nm$ results in super mode excitation at cut-off wavelength which gives a sensitivity equal to the theoretical

period. Practically, fabricating such a structure may not be economically feasible as it will require e-beam lithography or etching technique. In structure 3, deposition of high index film of thickness t_g=500 nm will result in additional optical losses in the dielectric film explained. Also, the non-Lorentzian shape of the resonance makes it difficult for sensing. Hence, as an alternative 2-D GMR structures are investigated further for super mode excitation at cut-off wavelength and the possible fabrication is studied which is explained in the next section.

4.6 Proposed 2D structure

Based on the analysis for the one-dimensional GMR, a two-dimensional grating is used based on structure 2 configuration. The proposed 2D GMR structure is shown in figure 4.17. Here, a film with a RI ng is deposited on top of a substrate with a RI n_s. The grating has a period of Λ (which is the dimension of the unit cell). The grating is formed by a two-dimensional lattice of pillars of radius r_g. A high RI film (n_f) is deposited on the grating. Similar to the 1D structure, the unit cell can be divided into four even layers with thicknesses $t_f, t_{sgf}, (t_g - t_{sgf}), and\ t_C$ as revealed in Fig.4.17(b). The effective refractive indices of these layers are n_{sf}, n_{sgf}, n_{gf} and n_g respectively. The layer labeled *sf* has an effective index, n_{sf}, that is a composition of the superstrate n_{sup} and n_f. The value of n_{sf} depends on the grating's fill factor. The lower index layer between the two higher indices (labeled n_{sgf}) depends on $n_{sup,}n_f$ and n_g. Finally, n_{gf} depends only on the RI n_g and n_f.When the superstrate is presented with an aquatic solution $(n_{sup} \approx 1.33)$, the RI values of n_{sf} and n_{gf} can

become comparatively close rendering both layers form effective guiding regions.

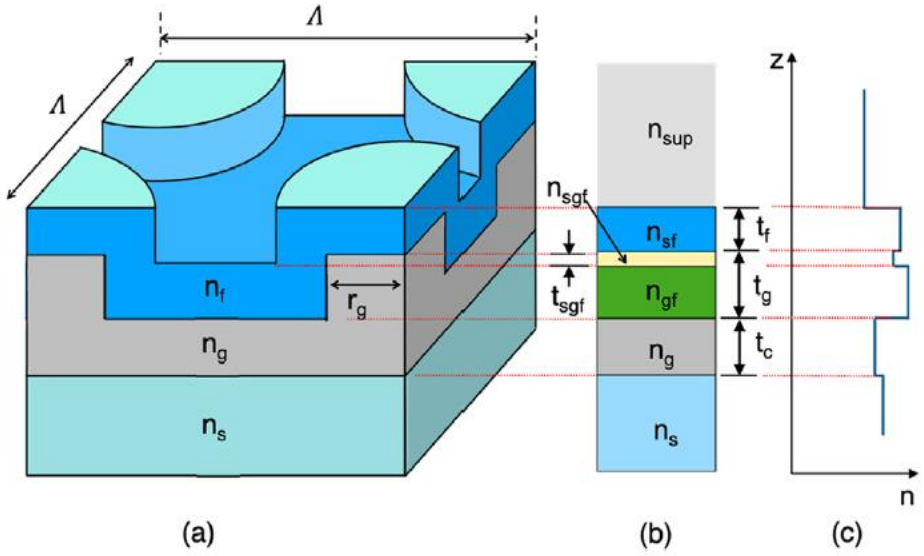

Figure 4.17: (a) The unit cell of the projected 2D GMR structure (b) the general four-layer waveguide representation and (c) visualization of the effective indices in case of water as superstrate.

4.6.1 Super-mode excitation at near cut-off diffraction in 2D structure

In the proposed 2D structure, the presence of two guiding regions close to each other can produce a coupling between the modes guided in each layer individually. This can by itself cause super-mode excitation in the two layers n_{sf} and n_{gf} as a one effective guiding region. Nevertheless, traditional guided mode is mostly confined in the region with highest RI (i.e., n_{gf}). In such a scenario, one of the super-modes excited at resonance can have more power confinement in the film with lower RI (n_{sf}). The presence of such super mode at resonance, having longitudinal wave number, β amid values of $k_0 n_{sup}$ and $k_0 n_{sf}$, permits high leakage of power into the superstrate region.

Such a super mode can result in high sensitivity to the variations of RI in the superstrate layer. Here, k_0 is the free-space wave number.

When the phase of excited super-mode matches to a diffraction order inside the superstrate close to the cut-off condition, enough reflectance can be detected at wavelength for cut-off condition. The condition of phase matching between the excited super-mode and an order of diffraction is defined in equation 4.1 when light is incident at zero incidence angle to the device with a square-grid periodicity. Here, δ is a small discrepancy in the condition of phase match. The orders of diffraction for the two-dimensional grating structures are defined as $m = \sqrt{(p^2 + q^2)}$ where (p, q) are the orders of diffraction in x and y axis, respectively. The diffraction cut-off condition is achieved once $m_{c.o}K_G = k_0 n_{sup}$ where $K_G = \frac{2\pi}{\Lambda}$ and $m_{c.o}$ is the diffraction order at cut-off diffraction in the superstrate region. The wavelength that satisfies this condition, $\lambda_{c.o}$, is commonly referred to as Rayleigh wavelength and it can be estimated from equation 4.2.

4.6.2 Optimization of the 2-D GMR structure

Maximization of the reflectance at the Rayleigh wavelength, $\lambda_{c.o}$, requires optimization of the structural parameters such as the film layer thickness, the grating thickness and grating's fill factor. This is needed to guarantee the excitation of a super mode with a wavelength that is sufficiently near to $\lambda_{c.o}$. The effective index of the resonant mode is almost equal to the superstrate's RI. Hence, variations in n_{sup} directly influence the mode and the resonance condition correspondingly.

4.6.2.1 Super-mode excitation at near cut-off diffraction

One way to tackle the optimization process is to visualize the resonance of super-mode at near cut-off condition. This is done by calculating the spectrum of the resonance for various superstrate indices and distribution of field at resonance condition using RCWA. Here, light is considered to be incident normally from the bottom of the structure i.e., the substrate side. The structure of GMR device is designed such that the excited super-mode resonance phase match to the first-order of diffraction at near cut-off condition in the superstrate region with an aqueous medium. The dimensions of the structure are $\Lambda = 500\,nm$, $_g = 50\,nm$, $t_g = 180\,nm$, $t_f = 115\,nm$, and $t_c = 500\,nm$. The structure taken into consideration has refractive indices of $n_g = 1.4$, $n_{gf} = 1.4$ and $n_f = 2.1$ and $n_s = 1.5$. A contour plot of the calculated resonance spectra versus change in the RI of the superstrate region is shown figure 4.17 (a). The graph shows that the resonances can be assembled into two categories: traditional modes $\left(TM_{0,guided(p,q)}/TE_{0,guided,(p,q)}\right)$ and supermodes $(TM_{0,super(p,q)}/$ $TE_{0,super(p,q)}$ at near cut-off wavelength). The indices p and q signify the diffraction orders where the first order (m=1) corresponds to p=1, q=0, or q=1 in the 2-D grating. The traditional GMR (due to matching of $TM_{0,guided}$ and $TE_{0,guided}$ to the first order of diffraction, *(p,q)*=(0,1), in the situation of water in the superstrate region) occurs at longer wavelengths (λ_2 and λ_3 as shown in figure 4.17 (b) for RI, $n_{sup} = 1.33$). The contour plot of the field in the figure 4.17 (d) shows that the light is highly concentrated in the highest RI region (n_{gf}). This gives only a small extension of the light into the sensing region, which is the superstrate. The peaks due to guided mode as well have

Lorentzian shape as depicted in figure 4.17 (b). Several resonances are present at shorter wavelengths as shown in 4.17 (a). Two peaks experience minimal change with n_{sup}. They are due to the matching between $TE_{0,guided}$ and $TM_{0,guided}$ to a higher order, (p,q)=(1,1).

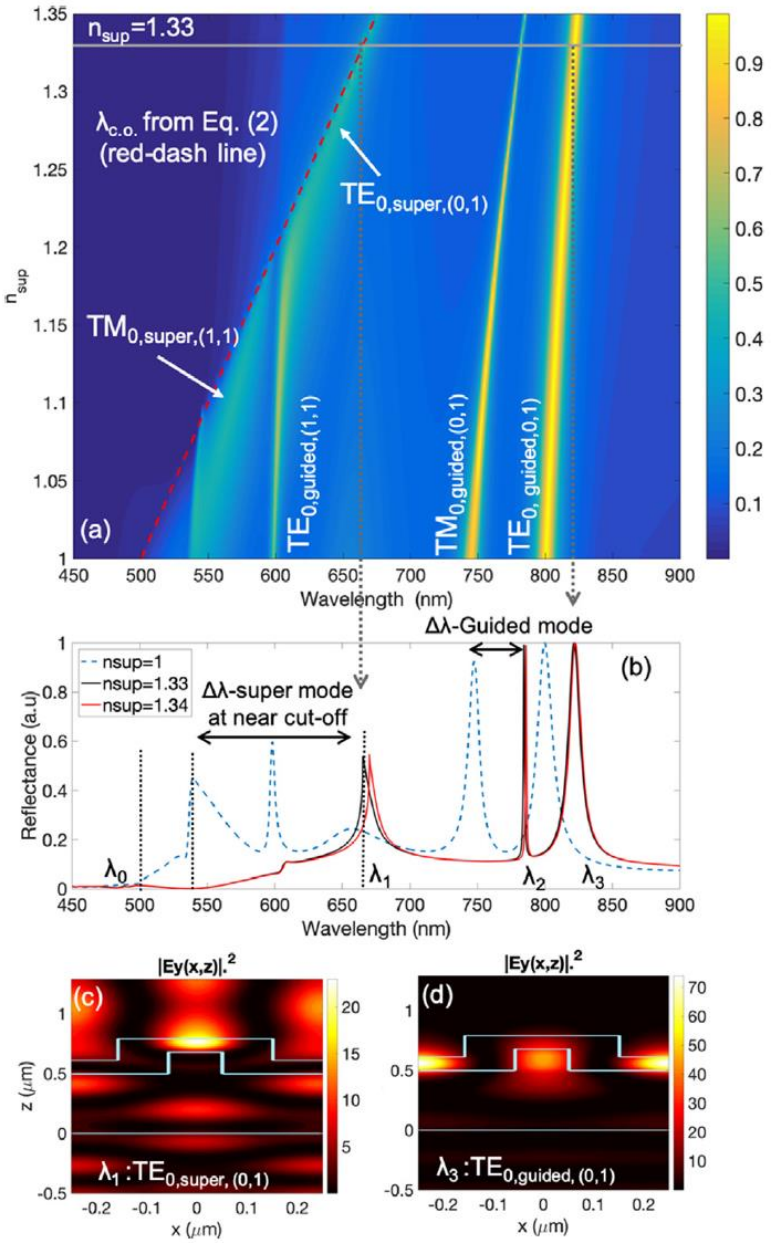

Figure 4.18: (a) Computed contour plot of reflection spectrum versus the change in the RI of the superstrate region (b) calculated spectrum for three values of n_{sup}: air (dashed), 1.33 (black line), and 1.34 (ref line). The calculated field distribution for (c) TE_0-super mode matching to (p,q)=(0,1) (at near cut-off) at λ_1 (c) TE_0-guided mode matching to (p,q)=(0,1) at λ_3.

The dispersion plot displays the existence of two modes having low confinement that appear to go along with the first diffraction order cut-off wavelength or $\lambda_{c.o}$, when $m_{c.o}$=1 in equation 4.2, as shown by the dashed line in red in figure 4.18 (a). The peaks due to traditional guided mode have a Lorentzian shape, which is labeled as guided-mode in figure 4.18 (b). At shorter wavelengths, numerous resonance peaks are present in figure 4.18(a). At higher values of the superstrate RI (n_{sup}=1.25-1.35), resonance is the outcome of matching the first order of diffraction, (p,q)=(0,1) to the odd super mode ($TE_{0,super}$) as labeled in figure 4.18 (a).PWV of resonance moves along with the cut-off condition according to equation 4.2 results in an upper limit sensitivity, S=1. At lower refractive indices (n_{sup}=1-1.2), the resonance occurring is the result of phase matching of the odd super-mode, $TM_{0,super}$ and the orders of diffraction, (p,q)=(1,1).

The contour plot in figure 4.18 (a) however shows that the super mode resonance occurring for superstrate RI, n_{sup}=1 is excited around the PWV of 550 nm. This is away from the cut-off wavelength at 500 nm, which decreases the sensitivity

(S<1) at low RI values of superstrate (e.g gas and vapor). As compared to guided mode there is rise in the sensitivity for the cut-off condition, at high n_{sup} values. This is due to lower confinement of mode near cut-off mode wavelength within the structure as shown in figure 4.18 (c). This is compared to the traditional guided mode where light is strongly concentrated in the region (n_{gf}). The location of the PWV at cut-off condition, from the reflection spectrum is shifted to 670 nm when n_{sup} changes to 1.34 from 1.33 $\left(\Delta\lambda/\Delta n = \frac{5}{0.01} = 500\ nm/RIU\right)$. This corresponds to equation 4.3 for the first order ($m_{c.o} = 1$). Here, the resultant sensitivity is proportional linearly to the period of the grating. For the first diffraction order, the sensitivity equals the period of the grating. Besides the grating period, other structure parameters such as the grating and film thickness should be adjusted in order to guarantee modal excitation near the cut-off condition.

4.6.2.2 Maximization of reflectivity at the cut-off diffraction

At the cut-off wavelength (Rayleigh wavelength) the reflectivity for the device is increased by selecting the best grating parameters (period and film thickness) using water $\left(n_{sup} = 1.33\right)$ as a superstrate. Figure 4.19 displays reflectance at Rayleigh wavelength under different combinations of t_g and t_f.

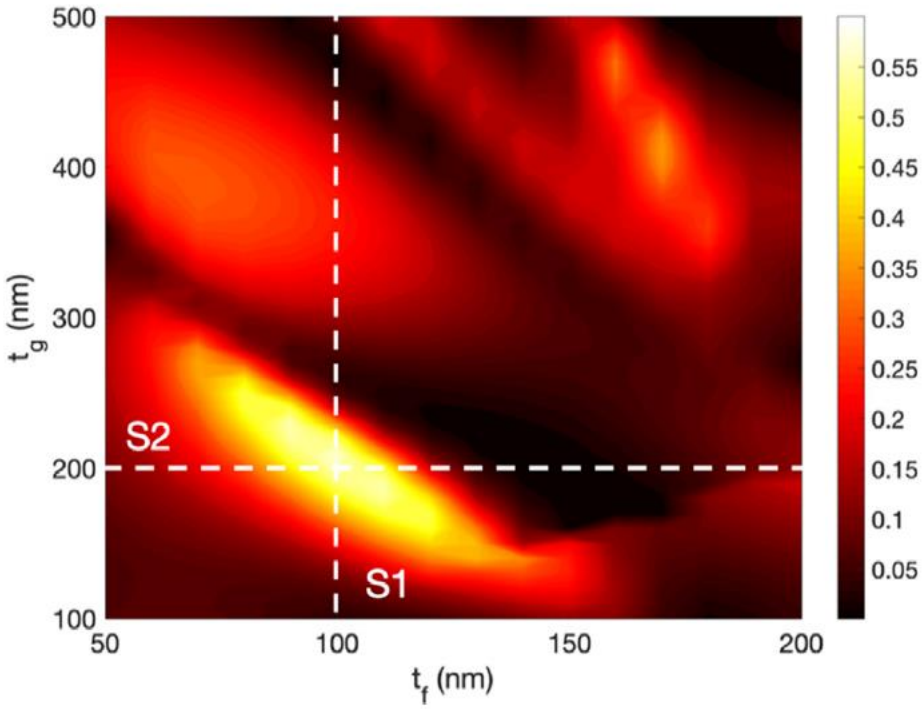

Figure 4.19: Contour plot of reflectance at $\lambda_{c.o}$ for n_{sup}=1.33 when varying film and grating thickness (t_f and t_g).

To analyze the evolution of mode in the structure of the device when varying both film and grating thickness, the reflection spectra are considered along the lines S1 (t_f=100 nm and changing t_g) and S2 (t_g=200 nm and changing t_f) as displayed in figure 4.20 (a) and figure 4.20 (b) respectively.

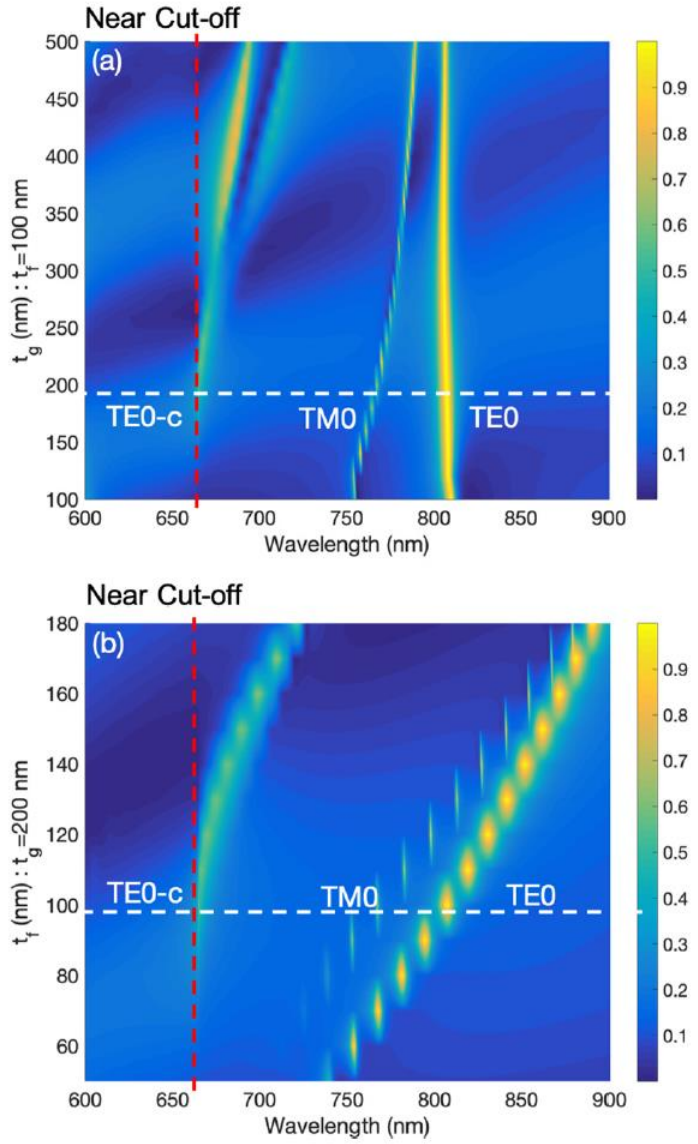

Figure 4.20: Reflection spectra from 2D GMR structure with Λ=500 nm,r_g=50 nm, t_c=500 nm, n_f=2.1, n_g=1.4, n_s=1.5, when (a) fixing t_f at 100 nm and varying t_g and (b) fixing t_g at 200 nm and varying t_f.

Figure 4.20 (a) shows that the resonance spectrum profile shifts from non-Lorentzian function to Lorentzian function when moving away from the cut-off wavelength (red-shifted peak for t_g larger than 200 nm). For the images in Fig. 4.20 (b), a non-

Lorentzian function peak arises around the film thickness, t_f=100 nm. A red-shift of the PWV at resonance happens on increasing the film thickness.

4.7 Experiments and characterization

In order to experimentally investigate the proper grating design, a set of gratings with targeted period of 500 nm are fabricated. In this set, the grating thickness (t_g) and film thickness (t_f) were varied. In the fabrication process, the grating was initially constructed in a photoresist film by the process of double exposure-two beams interference lithography. In the exposure process, the beams angles were aligned such that a 500 nm period grating is obtained. The resultant pattern was then shifted onto a film of spin on glass (SOG 400F having RI of 1.37 from Filmtronics Inc.) using soft mold imprinting technique. The SOG film is coated on top of a conventional glass slide. A mold was made by a casting process from the photoresist pattern at 60° curing temperature for five hours using Polydimethylsiloxane (PDMS) elastomer (Sylgard 184 Silicone Elastomer from Dow corning). Lastly, the imprinted grating on the SOG film on top of a glass slide, was coated with a slim layer of a high RI Tantalum Pentoxide film (Ta_2O_5 having RI of 2.16 at 633 nm) utilizing a commercial pulsed DC reactive magnetron sputtering arrangement and tantalum (Ta: 99.995 %) target (AJA International, Inc. ATC 2000-F).

Figure 4.20 displays the SEM images of the GMR structures fabricated with different profiles and grating depths. In the double exposure-two beams interference lithography process, three different doses of exposure were used to achieve grating structures with depths of t_g=150 nm, 179 nm, 255 nm respectively. The obtained gratings using this

method have a sinusoidal profile. These profiles tend to variation while increasing the depth of the grating at greater dose of exposure as represented in the figure. 4.21 The resonance mode excitation would be affected by variations in the profile. The obtained depth however covers the range of the calculated optimum value of t_g=200 nm. The Ta_2O_5 layer was coated for different values of thicknesses, t_f=90 nm, 112 nm, 126 nm, and 148 nm. These values have the ideal value of t_f=100 nm. These results in a total of 12 different structures from the combinations of t_f and t_g.

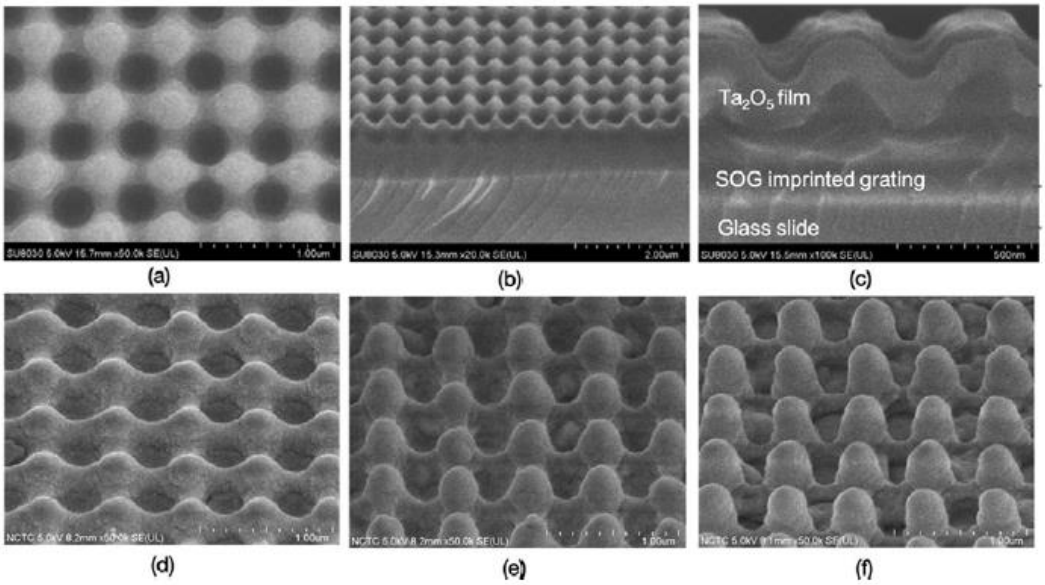

Figure 4.21: (a)-(c) SEM images of the fabricated GMRs having t_g=150 nm and t_f=140 nm (a) top view (b) bird eye view at low magnification (c) cross-section at high magnification. (d)-(f) bird eye view of the fabricated GMR structures having t_g=150 nm, t_g=179 nm and t_f=255 nm respectively, where t_f=98 nm.

The SEM images in figure 4.21 indicate that the grating period in the fabricated

GMR structures is approximately 520 nm. To confirm this crude estimation, measured spectrum response is compared to the calculations as shown in figure 4.22. This assures the previous estimation of a 520 nm period. This shift from the desired period of 500 nm is theoretically justified when associating the RCWA computation for two structures with dissimilar grating periods, 515 nm and 523 nm, as shown in figure 4.22, where the RCWA computations and experiment considered t_f=112 nm and t_g=150 nm for n_{sup}=1.33. In comparison to theory, the grating profile that was fabricated is not cylindrical. That results in a changed profile function for the unit cell. To incorporate this effect, the unit cell needs to be modified when formulating the RCWA calculations as proposed by the following equations.

$$t_1(r_1) = t_g exp\left[-4\left(\frac{r_1}{r_g}\right)^{\alpha_1}\right] \quad 4.4a$$

$$t_2(r_2) = t_g exp\left[-4\left(\frac{r_2}{r_g}\right)^{\alpha_2}\right] + t_f \quad 4.4b$$

Where $t_1(r_1)$ is the imprinted grating profile function with a radius r_g and depth t_g.$t_2(r_2)$ is the grating profile function after depositing a film having thickness t_f and α_1, α_2 are the profile coefficients.

In the RCWA computations, the GMR device is divided into N = int $[(t_g + t_f)/\delta]$ layers comprising concentric cylinders of radii r_1 and r_2 respectively. Using equations 4.4, the different values of r_1 and r_2 are found for layers of thickness $h\delta$, where $h = 1,2, \ldots . N$. Here the height step δ is set to 100 nm. Both α_1 and α_2 were adjusted to ideally match the results attained from the experiment, mainly for the guided modes. The radius of the grating, r_g is considered as half of the grating period. In the

calculations as shown in figure 22, α_1 and α_2 are set to 2 and 8.5 respectively. An improved match is displayed for the structure with grating period of 523 nm. The PWV of resonance is blue shifted for the structure with a smaller grating period. The PWV at Rayleigh (near-cut off) condition is governed by the period of the grating and the superstrate RI, n_{sup}. The grating profile affects the dispersal of the guided modes as well as the modal coupling efficiency.

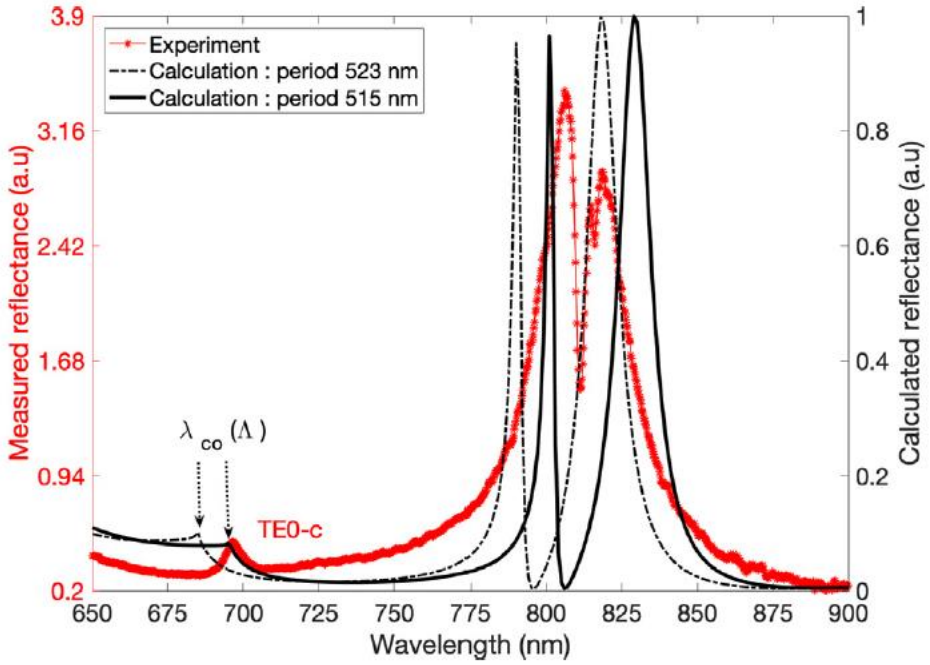

Figure 4.22: Comparison of reflection spectral between measurements and calculations of the fabricated GMR structure having t_g=150 nm and t_f=112 nm. In the calculations, r_g=Λ/2, α_1=2, α_2=8.5.

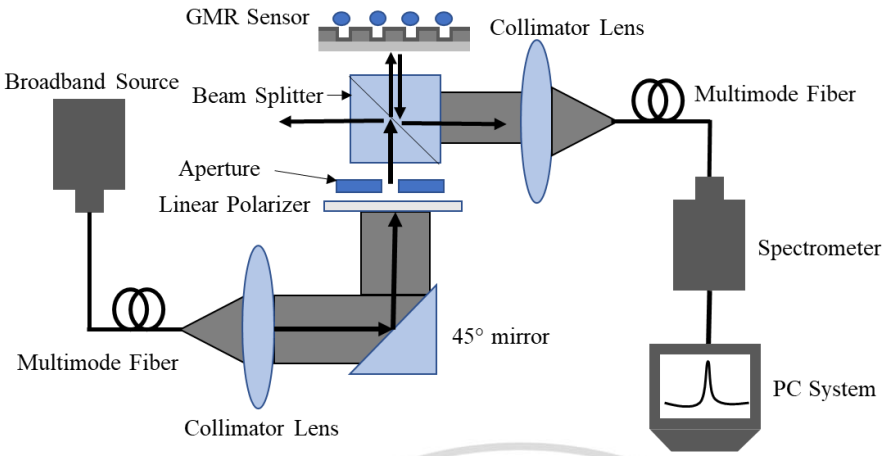

Figure 4.23: Schematic diagram of the experimental arrangement used to measure the reflectance spectrum of the GMR structure as well as the device sensitivity.

The resonance spectra of the fabricated GMR were measured using a tungsten-halogen light source (HL-2000, Ocean Optics) broadband light source, and a spectrometer (CCS200, Thorlabs) as shown in figure 4.23. The collimated beam is coupled to the system through a multimode fiber attached to a collimating lens. A linear polarizer is placed to allow only TM polarized light. The beam is incident normally on the bottom of the GMR. The reflected beam is collected and coupled to the spectrometer via a beam splitter and a multimode fiber. The bulk sensitivity of the GMR sensor were measured by dropping solutions of glycerol mixed with deionized water (DI) at different concentrations, where the RI is measured using a refractometer (ATAGO RX-5000-CX).

Figure 4.24 shows the reflection spectra of 12 numbers of square-grid 2D GMR structures which were measured experimentally. Here, individual GMR structure was

tested for sensitivity with air and six solutions having dissimilar refractive indices, as superstrate. The evaluation of the resonance spectra for three different combinations of t_g=150 nm, 179 nm, 255 nm, and the value of t_f fixed at 98 nm was plotted as displayed in figure 4.24 (a)-(c).

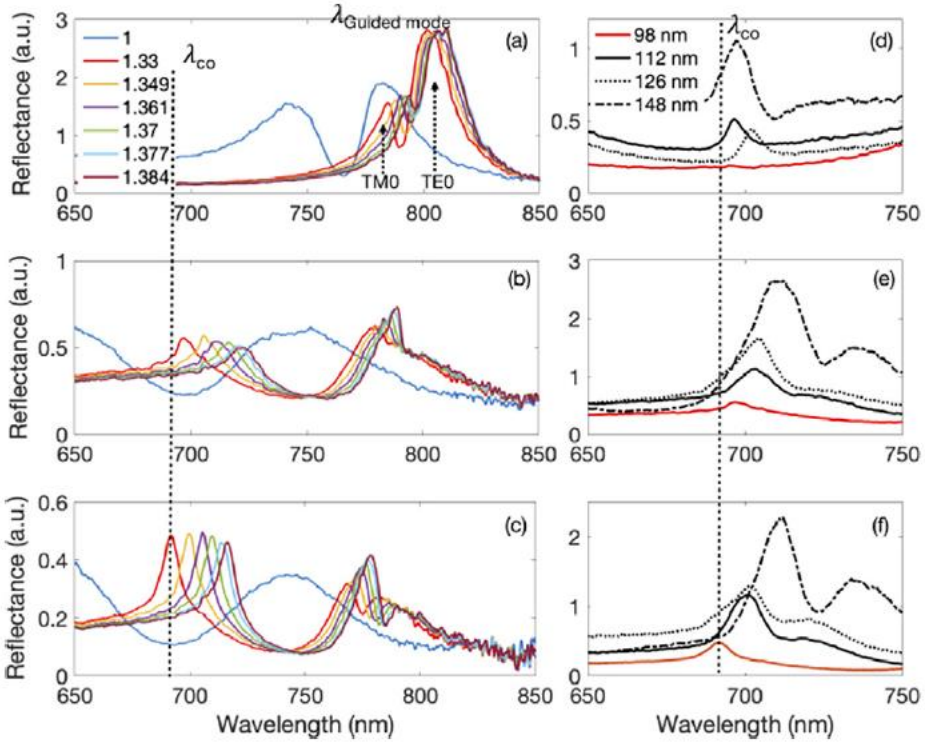

Figure 4.24: Measured reflectance spectra of the square-grid 2D GMR structures (a)-(c) comparison of reflectance spectra of the fabricated GMRs having (t_f, t_g)= (150 nm, 98 nm), (179 nm, 98 nm) and (255 nm, 98 nm), respectively, when measuring with different superstrate refractive indices.(d)-(f) Compared reflectance spectra at near cut-off resonance (measured in air-superstrate) respect to the values of t_f, where (d) t_g=150 nm (e) t_g=179 nm (f) t_g= 255 nm.

As seen in figure 4.24, the resonances acquired are assembled into two different parts:$\lambda_{c.o}$ and $\lambda_{guided\ mode}$.The plots display that the resonance at near cut-off excitation wavelength ($\lambda_{c.o}$) toughens when increasing the depth of the grating, which agrees with the prediction in figure 4.20 (a). The plots in the figure 4.24 (d)-(f) display the effect of the film thickness (t_f), for selected grating thickness$(\ t_g)$, on the near cut-off resonance wavelength. For the structure with t_g=150 nm, the resonance begins to become stronger at wavelengths of near-cut off excitation in films with thickness, t_f=112 nm and thicker. Structures having deeper grating period, specifically for t_g=255 nm display the desired results when the excitation is close to the cut-off wavelength as shown in the figure 4.24. Increasing the thickness of the film further moves the resonance peak away (red-shifted) as anticipated in figure 4.20 (b).

In figure 4.25, the calculated normalized sensitivities at near cut-off resonance and $TM_{0,guided\ mode}$ resonances from 12 different combinations of GMR structures with several measurements of t_g and t_f as shown in figure 4.25 are plotted versus the resonance wavelengths in nm. Individual data point having an identical symbol signifies the calculated normalized sensitivity of GMR structure having fixed t_g but changing t_f.The plots display that the calculated sensitivity of near cut-off resonance reached 517 nm/RIU, S=0.97. This sensitivity measured for resonance at near cut-off condition is two times greater as compared to the traditional GMR (200 nm/RIU, S=0.35). Further increasing the thickness of the film results in structural mode excitation and henceforth the sensitivity reduces as displayed in figure 4.25 (black dots

for t_g=150 nm and orange dots for t_g=255 nm).

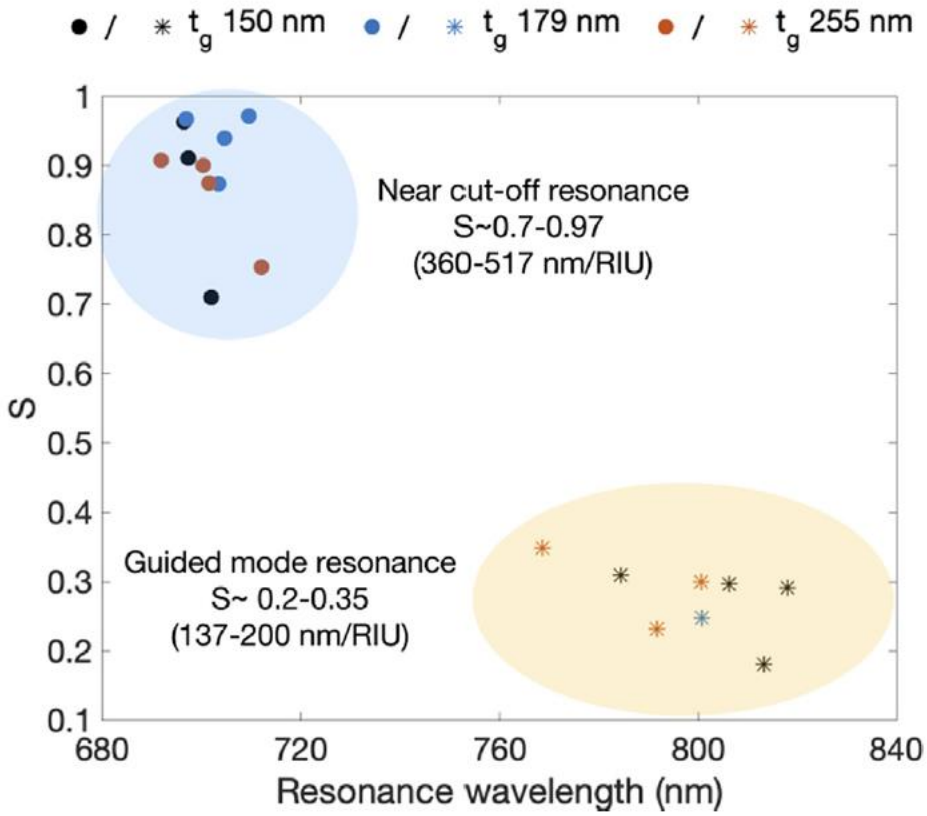

Figure 4.25: Measured sensitivities of near cut-off excitation compared to structure TM_0 mode resonance.

4.8 Summary

The proposed 2-D grating structure with grating thickness of 255 nm and high index film thickness of 98 nm showed high reflectance intensity close to 50% as compared to other structures. The desired structural parameters were fabricated using in-house fabrication techniques. The sensitivity of near cut-off resonance was calculated to be, S =0.97 which is very close to theoretical maximum sensitivity value of S =1.

CHAPTER 5

FINDING THE STUDY OF PART 2

This chapter addresses the second part of the objective of study, which includes the plan and development of a portable GMR-based read-out system. The developed system is then tested with different solutions in order to evaluate the system performance in term of sensitivity and detection limit.

5.1 Proposed GMR based Read-Out System

The GMR transducer integrated in shows in figure 5.1 The spectrometer read-out system is developed using off the shelf parts and a reflective grating shown. The proposed system is split into three sections: (a) light excitation and signal collection from the GMR transducer, (b) the integrated spectrometer based on web cam and (c) signal processing unit for peak point tracking based on image processing using Raspberry Pi computation system.

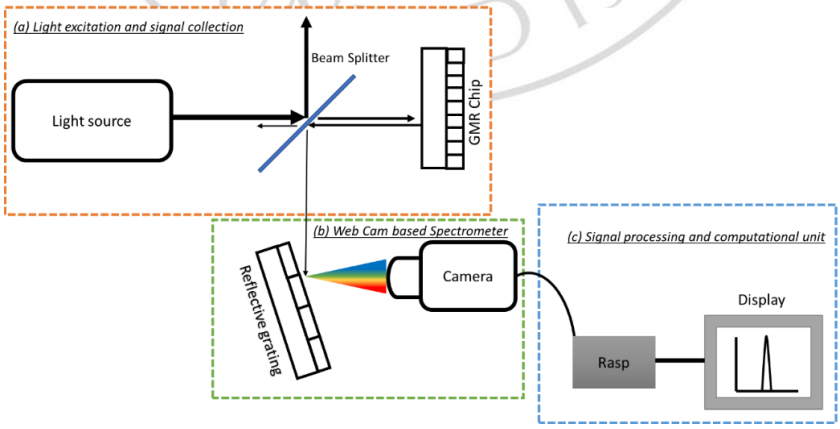

Figure 5.1: (a) Light excitation and signal collection (b) Web Cam based Spectrometer (c) Signal processing and computation unit using Raspberry Pi.

The system uses a warm white light as a source to irradiate the GMR transducer chip that is fabricated to reflect a definite frequency band based on the RI of the surrounding medium. The reflected light beam from the GMR chip is diffracted by another grating having different period, into different angular components based on the wavelength. These diffracted components are then captured by the imaging section of the system. The captured image of the reflection spectrum is processed by an in-house developed program using Python for spectrum extraction and peak location detection. In this system the spectrum is recorded versus pixel location instead of wavelength. This is due to the need for a calibration process. However, as the developed system is mainly intended for sensing application, wavelength calibration was not needed. The detected peak location is then measured in pixels. The location of the reflection peak shifts based on the RI of the solution on top of the GMR transducer chip. The performance of the system is then tested by putting on top of the GMR chip, a variety of solutions having different RI and measuring the peak shifts.

5.1.1 Light excitation and collection from GMR transducer

For the light excitation upon the GMR transducer chip, a warm white (300 K) source of light emitting diode (LED) (OSLON Square 3rd generation) with a driver for controlling the LED (LUMOTECH, LO5050,1-6.5 Watt, 700mA) is used. A linear polarizer filter is positioned after the light source in order to ensure TM polarized light

to be incident into the bottom of the GMR transducer chip incident at a normal angle. TM polarization is used here as it has a narrow resonant linewidth, which outcomes in a better Limit of Detection (LOD). The resonance peak spectral tunability can be analyzed by means of RCWA computations. The tunability of resonance spectra is obtained numerically by varying the grating period and the grating region thickness. The main aim of tunning these design parameters is to keep the PWV at resonance within the region of visible light (450nm to 650 nm). This is due to the fact that the sensitivity of the GMR is strongly dependent on the period as well as the film thickness. Increasing the period causes a red shift to the resonance (moving to a higher wavelength). To keep the location of the resonance peak within the visible range, structure optimization is performed using RCWA. These parameters are then used in fabricating the device using the laser interference lithography (LIL) technique. The simulated device is a one-dimensional grating with a rectangular slab profile. The structure is fabricated using nanoimprinting on SOG layer with RI, n_{gf}=1.37 and a period Λ. The depth of the grating is t_g . A Tantalum Pentoxide (Ta_2O_5) layer is coated on top of the grating to work as the guiding region. It has a thickness t_f and a refractive index n_f=2.1. Finally, the remaining SOG layer under the grating has a thickness of t_{gf}. Figure 5.2 shows the structure used in the RCWA simulations.TM polarization is considered for calculating the resonance response of the fundamental mode.

Figure 5.2: Structure of GMR simulated in RCWA

In order to keep the resonance peaks within the spectrum of visible light, three different grating periods having values, 330nm, 350nm, and 370nm were chosen. The depth of the grating layer was tuned from 100nm to 200nm.As a single resonance peak result in better detection, a thin waveguiding layer was used that permits only fundamental mode to propagate guided inside the waveguide. Figure 5.3 displays the contour plot of the shift in the PWV at resonance of the fundamental mode when changing the structural parameters. The tuning of the structure was done using RCWA.

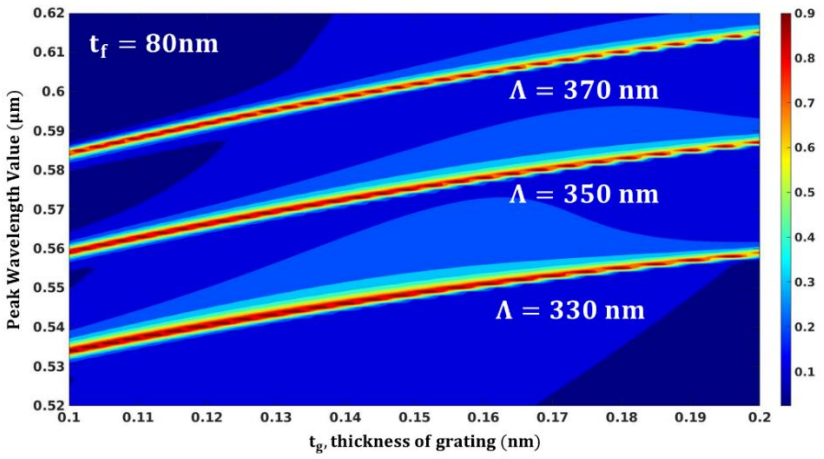

Figure 5.3: Contour plot of resonance peak for fundamental mode variation for period of grating, Λ=330nm, 350nm and 370 nm and thickness of grating, t_g varied from 100nm to 200nm

Considering a trade-off between the period of grating and PWV at resonance within visible range a period of value, Λ =350nm, t_{gf}=180nm and t_g=80nm with a fill factor of 0.5 was chosen as GMR structure parameters.

5.1.2 Design approach of the integrated spectrometer

The in-house built spectrometer is designed with reflective diffraction grating and a CMOS webcam (ELP-USB8MP02G-L75). The beam of light that is reflected from the GMR chip is incident upon the reflective diffraction grating at an incident angle θ_i. The reflective diffraction grating splits the light into different angular components depending on the wavelength of light. The diffracted light from the grating is then recorded by the camera.

The effect of the angular width of the diffracted light from the reflective grating on the design of the spectrometer is calculated using equation 3.35 which is already defined in chapter three of the thesis. Considering practical aspects, fabrication of larger period grating is easier than smaller grating. Hence, it is reasonable to target a grating with a period between 950 nm to 1250 nm. For this range of grating period, the diffraction angular width is compared for the first and second order of diffraction. It is clearly seen in figure 5.4 that the second order diffraction, m=2, has a higher angular width compared to the first order, m=1.

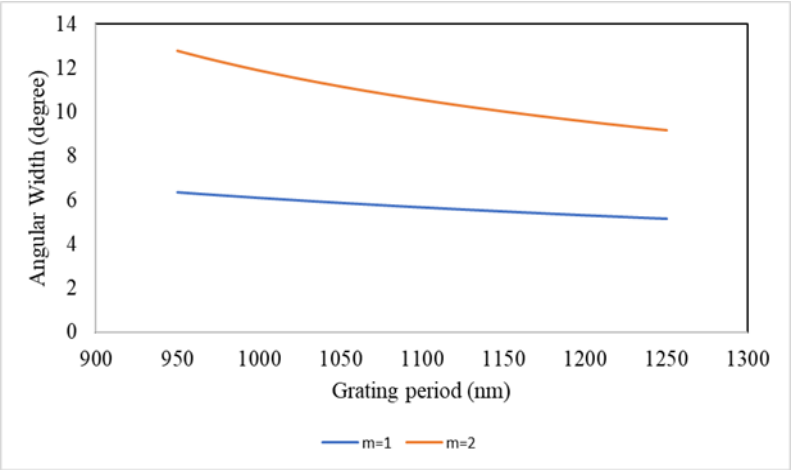

Figure 5.4: Angular width calculation for grating period from 950-1250 nm for m=1 and m=2 order of diffraction.

The imaging system used a CMOS image sensor array with a total width of 6.18 mm. Three different imaging lenses with focal lengths:6 mm, 8mm, and 12 mm are tried separately. The calculation of object distances for each focal length is performed and plotted as displayed in figure 5.5 (a). A larger focal length gives a better image resolution. A comparison of object distance, total number of pixels enclosed by the image, and magnification is shown in figure 5.5 (b).

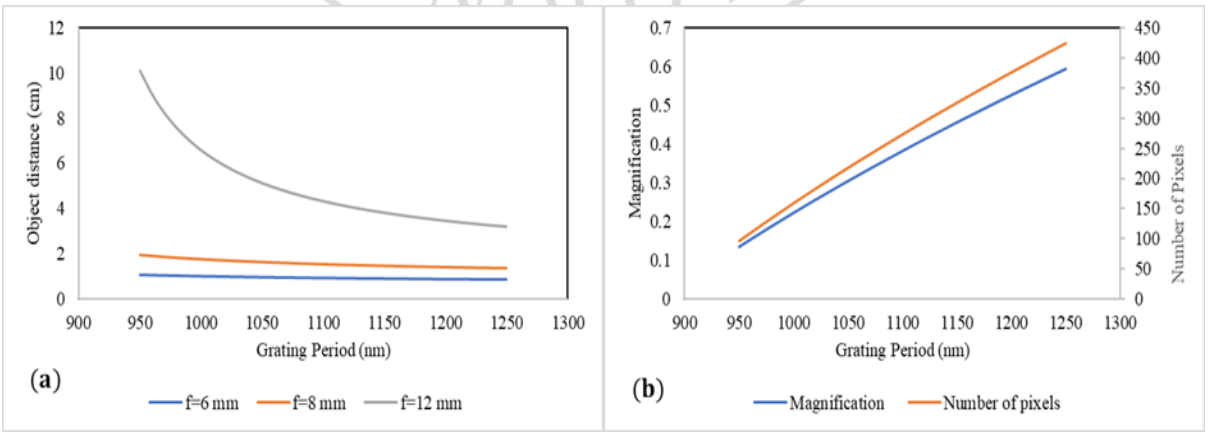

Figure 5.5: (a) Object distance variation for focal lengths f=6mm, 8 mm and 12 mm (b) Number of Pixels covered by the spectrum (450nm-650nm) for f=1.2 varying the grating period (950 nm- 1250 nm) with the incident angle of 70°.

Grounded on the study of design parameters performed, a grating period of Λ =1200 nm is selected towards the fabrication of the reflective diffraction grating. The mechanical arrangement of the read-out system is arranged utilizing 3D printed parts which provide rigidity and lightweight to the overall setup. Fused Deposition (FD) molding method is implemented for constructing a 3D printed mechanical support system for the spectrometer read-out system.

Figure 5.6 shows an image of the developed read out system with the (1) GMR transducer chip placed on top (2) Linear polarizer filter, (3) 1-D reflective diffraction grating, (4) LED source of light, (5) HD CMOS camera, (6) 1.2 mm focal length lens, (7) 50-50 beam splitter. To allow only TM polarized light, a linear polarizer sheet is placed. The distance between the 50-50 beam splitter and the reflective diffraction grating is set at 50 mm and the distance between the reflective diffraction grating and 1.2 mm focal length lens is set at 15 mm. The acquisition of signal is accomplished with a CMOS HD camera which is linked to the Raspberry Pi computational unit for detecting the resonant peak value.

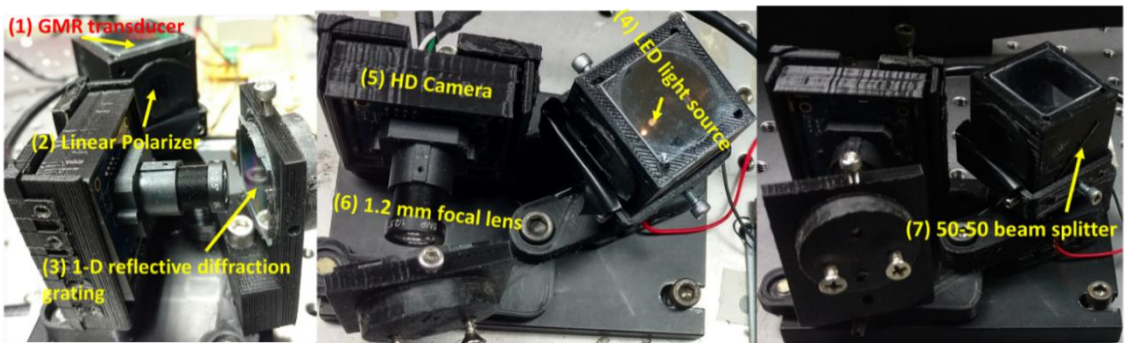

Figure 5.6: Realized GMR based system with spectrometer along with components assembles using 3D printed parts.

The design of the integrated spectrometer is grounded on the various parameters given in Table 5.1 and image acquisition is performed.

Table 5.1: Design parameters for spectrum to capture the 2nd order spectrum

Spectrum range	θ_w	d	v	m
450nm-650nm	20°	50 mm	15 mm	0.5

5.2 Image processing method for peak value tracking

Utilizing the design approach as explained in section 3.5 of the thesis, the spectrum of the signal obtained from the GMR transducer chip is captured by the camera. The captured image is cropped using the Track 1 and Track 2 tab as shown in figure 5.7 (b). The cropped region covers the spectrum from green to red color of light. The tracking of peak values is done by means of image processing with Python Programming on Raspberry Pi 3 computational unit.

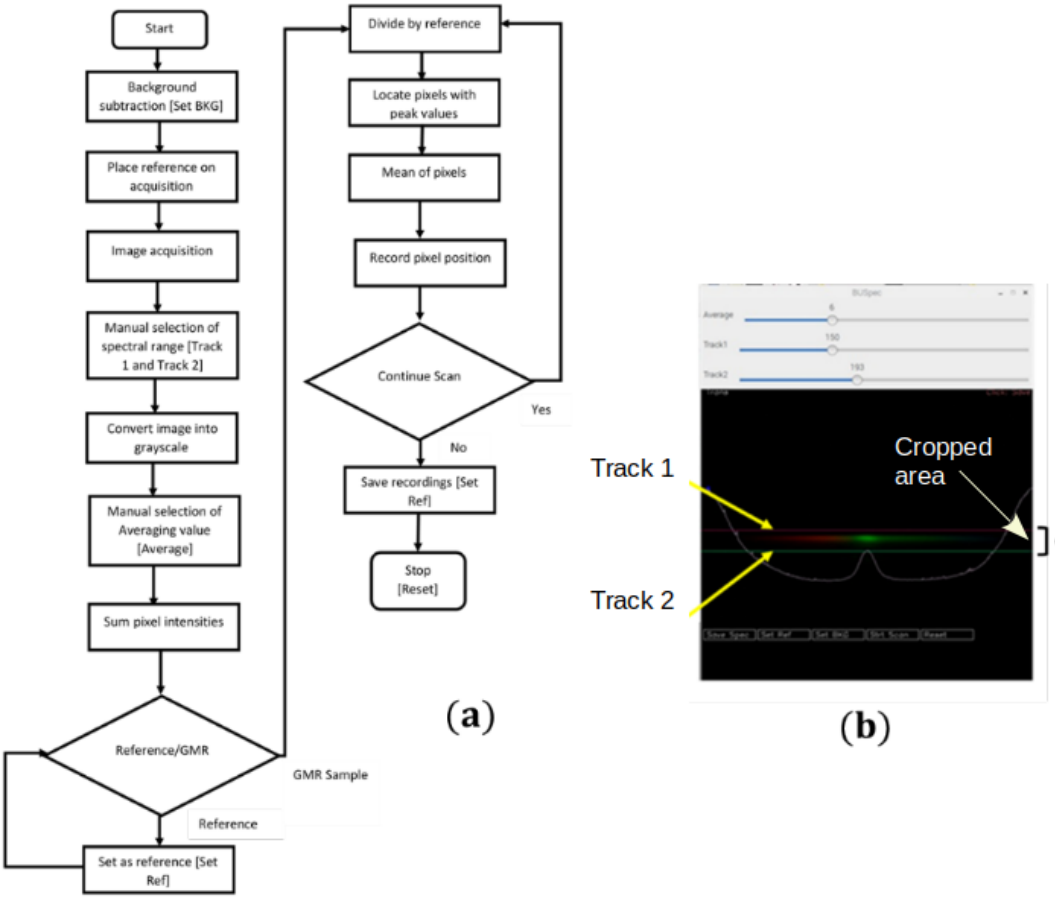

Figure 5.7: (a) Image processing flowchart of spectrum analysis for extraction of spectral data and finding peak position (b) Graphical User Interface (GUI) for peak tracking.

The flowchart in figure 5.7 (a) shows the protocol followed for image acquisition and processing to track the peak value of the spectrum. Firstly, a reference is established using a sample of glass side coated with Ta_2O_5. For attainment of the image from the HD CMOS camera, the region covering the spectrum is manually selected by cropping the image and averaging is done by the average tab to increase the signal-to-noise (SNR) ratio. The selected region is then transformed to grayscale after

which the intensity of recorded pixels is added horizontally. The average column is converter into spectrum and set as reference. Then the reference slide sample removed and the GMR transducer sample is placed on top. The same protocol is followed to obtain the GMR spectrum. The values logged from the GMR transducer sample is then divided by the values logged from the reference slide sample to acquire the peak position value. The Graphical User Interface (GUI) designed to detect and obtain the resonance peak value is displayed in figure 5.7 (b).

5.3 Response of GMR read-out system

The sensitivity response of the designed readout system was verified with samples of Glycerol having dissimilar RI, the RI values of which are shown in table 5.2. The testing of the readout system initializes with DI water. The surfaces of the sample are cleaned with alcohol before the next sample is positioned. This procedure is followed for all the other samples (Sample 2, Sample 3, Sample 4 and Sample 5). The change in the position of the peak value due to the variation in the RI of the samples is logged as delta pixel. The position at which, the peak occurs for DI water on the GMR transducer sensing surface is taken as the first pixel. The position of the peak is recorded for the RI ranging from the values 1.33248 to 1.35417, which cover the green to red spectrum of light.

Table 5.2: Superstrate solutions for GMR read-out system response testing

Sample 1	De-ionized water	Refractive index (n)=1.33248
Sample 2	5% Glycerol Solution	n=1.3389

Sample 3	10% Glycerol solution	n=1.3453
Sample 4	15% Glycerol solution	n=1.3510
Sample 5	20% Glycerol solution	n=1.35417

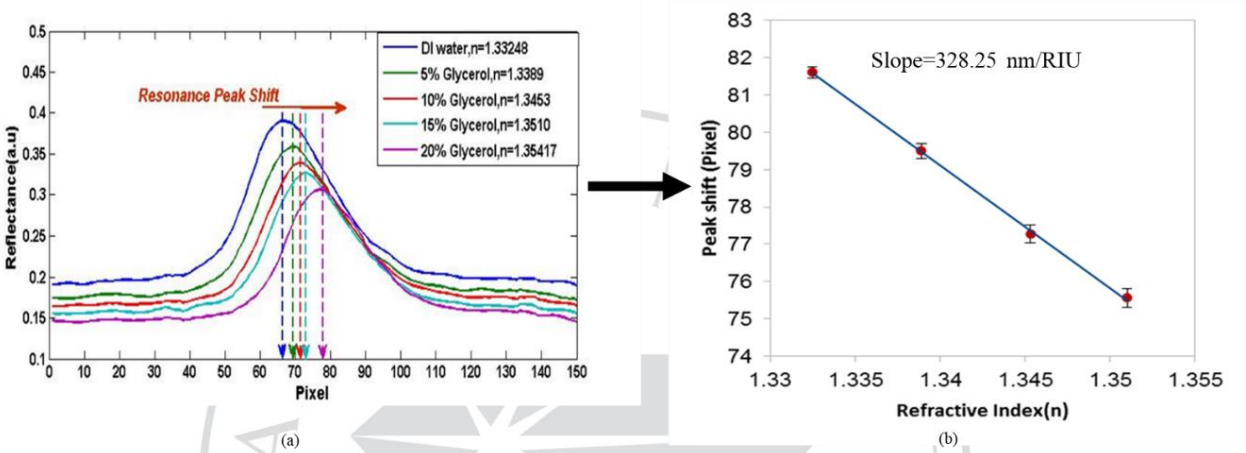

Figure 5.8: Resonance peak shift for different solutions from experiment. (b) Plot of peak position with change in superstrate refractive index from experiment.

A distinct shift in the peak pixel position with an increase of solution RI can be seen in the figure 5.8 (a). The spectrum is recorded 15 number of times for individual RI with a pause of 1 minute per recording. A distinct number of peak pixel position are recorded for each RI of the solution to compute the standard deviation of the peak pixel position. Figure 5.8 (b) displays the shift in the peak pixel position of different solutions and their standard deviation (std). The sensitivity of the GMR transducer is obtained from the slope of the linear fit as shown in figure 5.8 (b). The theoretical LOD was computed as the std divided by the GMR transducer bulk sensitivity (nm/RIU). The LOD as calculated from the obtained data is 6.093×10^{-4}.

5.4 Summary

The developed read-out system with a LOD of the order of 10^{-4} RIU in the visible spectrum opens many possibilities for application as a gas sensor, or as a biosensor for surface sensing with suitable surface functionalization, or for bulk sensing of solutions. The spectrometer established here using a diffraction grating, off-the-shelf optical components, and applying raspberry pi computation unit as a peak pixel tracking device offers a substitute to commercial spectrometers and smartphones as an imaging device. Optimal settings for the arrangement of components used in the spectrometer can be easily planned based upon the specifications of the webcam from the plot as stated in this section. The spectrum of the resonance peak value can be altered by varying the period of the grating. This opportunity makes it feasible for the end-user to choose the span of spectrum in the visible region for which the application of the GMR based read-out system is to be performed. The designed read-out system also has the flexibility of selecting 1-D GMR structure made up of diverse materials, having different structural profile, or 1-D GMR device utilizing higher order modes for sensing that have the resonance PWV in range of visible spectrum. Lastly, low-cost 3D printing tools offer strong support of alignment to the various optical components used for setting up the read-out system.

CHAPTER 6

CONCLUSIONS AND FUTURE WORK

In this dissertation, the first part of the study shows the strengthening of the RA via excitation of super mode resonance at wavelength near to the cut-off diffraction condition in a guided mode resonance (GMR) based sensor. Through such excitation at near cut-off diffraction, the sensor's bulk sensitivity can reach the upper limit at a value linearly proportional to the period of the grating. The configuration of the verified GMR sensor is such that it has a high RI film coated on a low RI grating layer. The study was done in one dimensional and two-dimensional grating structure which was configured as a four-layer waveguide structure. This permits the presence of the super mode in which the field at resonance is more confined on the lower RI layer than the high RI layer. This causes more leakage into the superstrate region resulting in higher sensitivity resonances. The spectra of resonance and distribution of field in the structure were computed using RCWA. Considering the ease of fabrication and non-dependent on the polarization of input optical signal, the GMR structures were fabricated utilizing laser interference lithography method, nanoimprint process, and sputtering technique. The resonance spectra of the fabricated GMR device were measured using an optical setup and correlated to the theoretically calculated results. The results obtained from the experiments displayed that the calculated sensitivity of super mode at near cut-off resonance condition attains as high as 517 nm/RIU, S=0.97, while the sensitivity of traditional TM_0 guided mode resonance is 200 nm/RIU, S=0.35.

The second part of the study established an arrangement utilizing 3D printing

tool that permits researchers to develop read-out systems for RI sensing applications. A detection limit of $6.093X10^{-4}$ RIU is obtained, which is well-suited for applications where threshold detection limit is adequate. Such read-out system offers an encouraging platform for implementing the readout system in numerous applications. The application of Raspberry Pi software in the readout system makes it open-source and user-friendly. This system can be a classical candidate for academic and research purposes. The LOD of the read-out system can be enhanced more by reducing the std by means of using a camera having better resolution. A lower std will result in a improved minimum RIU for detection. The application of such a read-out system can also be realized in the biomedical field by coating the GMR transducer chip, which is the sensing region, with a chemically active layer that can be used to attach the analyte under test. This read-out system can be further advanced for portable and on-site applications. For threshold detection, this system can be utilized and further improved for applications in real-time situations.

BIBLIOGRAPHY

Babu, S., & Lee, J.-B. (2019). Axially-anisotropic hierarchical grating 2D guided-mode resonance strain-sensor. *Sensors*, *19*(23), 5223.

Bark, H. S., & Jeon, T.-I. (2018). Tunable terahertz guided-mode resonance filter with a variable grating period. *Optics Express*, *26*(22), 29353–29362.

Block, I. D., Ganesh, N., Lu, M., & Cunningham, B. T. (2008). A sensitivity model for predicting photonic crystal biosensor performance. *IEEE Sensors Journal*, *8*(3), 274–280.

Boonruang, S. (2007). *Two-dimensional guided mode resonant structures for spectral filtering applications*. Florida, University of Central Florida.

Boonruang, S., & Mohammed, W. S. (2011). Effect of the cladding layer on resonance response in guided mode resonance structures and its sensing applications. *JOSA B*, *28*(4), 671–678.

Bougot-Robin, K., Paget, J., Atkins, S. C., & Edel, J. B. (2016). Optimization and design of an absorbance spectrometer controlled using a raspberry Pi to improve analytical skills. *Journal of Chemical Education*, *93*(7), 1232–1240.

Choi, J., Gani, A. W., Bechstein, D. J., Lee, J.-R., Utz, P. J., & Wang, S. X. (2016). Portable, one-step, and rapid GMR biosensor platform with smartphone interface. *Biosensors and Bioelectronics*, *85*, 1–7.

Cotter, N. P. K., Preist, T. W., & Sambles, J. R. (1995). Scattering-matrix approach to multilayer diffraction. *JOSA A*, *12*(5), 1097–1103.

Cunningham, B., Lin, B., Qiu, J., Li, P., Pepper, J., & Hugh, B. (2002). A plastic colorimetric resonant optical biosensor for multiparallel detection of label-free biochemical interactions. *Sensors and Actuators B: Chemical*, *85*(3), 219–226.

Cunningham, B. T., Li, P., Schulz, S., Lin, B., Baird, C., Gerstenmaier, J., Genick, C., Wang, F., Fine, E., & Laing, L. (2004). Label-free assays on the BIND system. *Journal of Biomolecular Screening*, *9*(6), 481–490.

Dang, P. T., Le, K. Q., Ngo, Q. M., Nguyen, H. P. T., & Nguyen, T. K. (2019). Guided-mode resonance filter with ultra-narrow bandwidth over the visible frequencies for label-free optical biosensor. *Journal of Advanced Engineering and Computation*, *3*(2), 406–414.

Deb, H., Srisuai, N., Jolivot, R., Promptmas, C., Mohammed, W. S., & Boonruang, S. (2020). Enhanced sensitivity of guided mode resonance sensor through super-mode excitation at near cut-off diffraction. *Optics & Laser Technology*, *132*, 106517.

Eitan, M., Iluz, Z., Yifat, Y., Boag, A., Hanein, Y., & Scheuer, J. (2015). Degeneracy breaking of Wood's anomaly for enhanced refractive index sensing. *Acs Photonics*, *2*(5), 615–621.

El Beheiry, M., Liu, V., Fan, S., & Levi, O. (2010). Sensitivity enhancement in photonic crystal slab biosensors. *Optics Express*, *18*(22), 22702–22714.

Fan, S., & Joannopoulos, J. D. (2002). Analysis of guided resonances in photonic crystal slabs. *Physical Review B*, *65*(23), 235112.

Fano, U. (1941). The theory of anomalous diffraction gratings and of quasi-stationary waves on metallic surfaces (Sommerfeld's waves). *JOSA*, *31*(3), 213–222.

Fattal, D., Sigalas, M., Pyayt, A., Li, Z., & Beausoleil, R. G. (2007). Guided-mode resonance sensor with extended spatial sensitivity. *Active Photonic Crystals*, *6640*, 66400M.

Gaylord, T. K., & Moharam, M. G. (1985). Analysis and applications of optical diffraction by gratings. *Proceedings of the IEEE*, *73*(5), 894–937.

Grann, E. B., Moharam, M. G., & Pommet, D. A. (1994). Artificial uniaxial and biaxial dielectrics with use of two-dimensional subwavelength binary gratings. *JOSA A*, *11*(10), 2695–2703.

Gryga, M., Ciprian, D., & Hlubina, P. (2020). Guided-mode resonance based humidity sensing using a multilayer dielectric structure. *Optics Express*, *28*(20), 28954–28960.

Hecht, E. (1998). *Optics*, New York: Longman.

Hessel, A., & Oliner, A. A. (1965). A new theory of Wood's anomalies on optical gratings. *Applied Optics*, *4*(10), 1275–1297.

Horváth, R., Lindvold, L. R., & Larsen, N. B. (2002). Reverse-symmetry waveguides: Theory and fabrication. *Applied Physics B*, *74*(4–5), 383–393.

Hossain, M. A., Canning, J., Ast, S., Cook, K., Rutledge, P. J., & Jamalipour, A. (2015). Combined "dual" absorption and fluorescence smartphone spectrometers. *Optics Letters*, *40*(8), 1737–1740.

Hossain, M. A., Canning, J., Cook, K., & Jamalipour, A. (2016). Optical fiber smartphone spectrometer. *Optics Letters*, *41*(10), 2237–2240.

Huang, Q., Peh, J., Hergenrother, P. J., & Cunningham, B. T. (2016). Porous photonic crystal external cavity laser biosensor. *Applied Physics Letters*, *109*(7), 071103.

Kenaan, A., Li, K., Barth, I., Johnson, S., Song, J., & Krauss, T. F. (2020). Guided mode resonance sensor for the parallel detection of multiple protein biomarkers in human urine with high sensitivity. *Biosensors and Bioelectronics*, *153*, 112047.

Ku, Y.-F., Li, H.-Y., Hsieh, W.-H., Chau, L.-K., & Chang, G.-E. (2015). Enhanced sensitivity in injection-molded guided-mode-resonance sensors via low-index cavity layers. *Optics Express*, *23*(11), 14850–14859.

Kwon, L., Long, K. D., Wan, Y., Yu, H., & Cunningham, B. T. (2016). Medical diagnostics with mobile devices: Comparison of intrinsic and extrinsic sensing. *Biotechnology Advances*, *34*(3), 291–304.

Lalanne, P. (1997). Improved formulation of the coupled-wave method for two-dimensional gratings. *JOSA A*, *14*(7), 1592–1598.

Lan, G., Zhang, S., Zhang, H., Zhu, Y., Qing, L., Li, D., Nong, J., Wang, W., Chen, L., & Wei, W. (2019). High-performance refractive index sensor based on guided-mode resonance in all-dielectric nano-silt array. *Physics Letters A*, *383*(13), 1478–1482.

Lin, H.-A., Hsu, H.-Y., Chang, C.-W., & Huang, C.-S. (2016). Compact spectrometer system based on a gradient grating period guided-mode resonance filter. *Optics Express*, *24*(10), 10972–10979.

Lin, H.-A., & Huang, C.-S. (2016). Linear variable filter based on a gradient grating period guided-mode resonance filter. *IEEE Photonics Technology Letters*, *28*(9), 1042–1045.

Lin, S.-F., Wang, C.-M., Ding, T.-J., Tsai, Y.-L., Yang, T.-H., Chen, W.-Y., & Chang, J.-Y. (2012). Sensitive metal layer assisted guided mode resonance biosensor with a spectrum inversed response and strong asymmetric resonance field distribution. *Optics Express*, *20*(13), 14584–14595.

Liu, F., & Zhang, X. (2016). Contrast-and intensity-enhancement of sensor signals based on Rayleigh anomaly in metal-coated gratings. *Optical Materials Express*, *6*(2), 682–690.

Liu, J.-N., Schulmerich, M. V., Bhargava, R., & Cunningham, B. T. (2011). Optimally designed narrowband guided-mode resonance reflectance filters for mid-infrared spectroscopy. *Optics Express*, *19*(24), 24182–24197.

Liu, L., Khan, H. A., Li, J., Hillier, A. C., & Lu, M. (2016). A strain-tunable nanoimprint lithography for linear variable photonic crystal filters. *Nanotechnology*, *27*(29), 295301.

Liu, Z. S., Tibuleac, S., Shin, D., Young, P. P., & Magnusson, R. (1998). High-efficiency guided-mode resonance filter. *Optics Letters*, *23*(19), 1556–1558.

Ma, J., & Zhang, D. (2012). Ultra-sensitive bio-sensor based on GMR in self-suspended-membrane-type germanium grating. *Journal of Optics*, *14*(8), 085002.

Magnusson, R., Lee, K. J., Hemmati, H., Ko, Y. H., Wenner, B. R., Allen, J. W., Allen, M. S., Gimlin, S., & Weidanz, D. W. (2018). The guided-mode

resonance biosensor: Principles, technology, and implementation. *Frontiers in Biological Detection: From Nanosensors to Systems X, 10510*, 105100G.

Magnusson, R., & Wang, S. S. (1992). New principle for optical filters. *Applied Physics Letters*, *61*(9), 1022–1024.

Magnusson, R., Wawro, D., Zimmerman, S., Ding, Y., Shokooh-Saremi, M., Lee, K. J., Ussery, D., Kim, S., & Song, S. H. (2010). Leaky-mode resonance photonics: Technology for biosensors, optical components, MEMS, and plasmonics. *Integrated Optics: Devices, Materials, and Technologies XIV*, *7604*, 76040M.

Maystre, D. (2012). Theory of Wood's anomalies. In *Plasmonics* (pp. 39–83). Springer.

Moghaddas, S. A. J., Shahabadi, M., & Mohammad-Taheri, M. (2013). Guided mode resonance sensor with enhanced surface sensitivity using coupled cross-stacked gratings. *IEEE Sensors Journal*, *14*(4), 1216–1222.

Moharam, M. G. (1988). Coupled-wave analysis of two-dimensional dielectric gratings. *Holographic Optics: Design and Applications*, *883*, 8–11.

Moharam, M. G., Grann, E. B., Pommet, D. A., & Gaylord, T. K. (1995). Formulation for stable and efficient implementation of the rigorous coupled-wave analysis of binary gratings. *JOSA a*, *12*(5), 1068–1076.

Moharam, M. G., Pommet, D. A., Grann, E. B., & Gaylord, T. K. (1995). Stable implementation of the rigorous coupled-wave analysis for surface-relief gratings: Enhanced transmittance matrix approach. *JOSA A*, *12*(5), 1077–1086.

Neviere, M., Vincent, P., Petit, R., & Cadilhac, M. (1973a). Systematic study of resonances of holographic thin film couplers. *Optics Communications*, *9*(1), 48–53.

Neviere, M., Vincent, P., Petit, R., & Cadilhac, M. (1973b). Systematic study of resonances of holographic thin film couplers. *Optics Communications*, *9*(1), 48–53.

Nguyen, T., Zoëga Andreasen, S., Wolff, A., & Duong Bang, D. (2018). From lab on a chip to point of care devices: The role of open source microcontrollers. *Micromachines*, *9*(8), 403.

Palmer, C. H. (1952). Parallel diffraction grating anomalies. *JOSA*, *42*(4), 269–276.

Peng, S., & Morris, G. M. (1996). Resonant scattering from two-dimensional gratings. *JOSA A*, *13*(5), 993–1005.

Piper, J. R., & Fan, S. (2014). Total absorption in a graphene monolayer in the optical regime by critical coupling with a photonic crystal guided resonance. *Acs Photonics*, *1*(4), 347–353.

Popov, E., Mashev, L., & Maystre, D. (1986). Theoretical study of the anomalies of coated dielectric gratings. *Optica Acta: International Journal of Optics*, *33*(5), 607–619.

Qian, L., Zhang, D., Huang, Y., Tao, C., Hong, R., & Zhuang, S. (2015). Performance of a double-layer guided mode resonance filter with non-subwavelength grating period at oblique incidence. *Optics & Laser Technology*, *72*, 42–47.

Qian, L., Zhang, D., Tao, C., Hong, R., & Zhuang, S. (2016). Tunable guided-mode resonant filter with wedged waveguide layer fabricated by masked ion beam etching. *Optics Letters*, *41*(5), 982–985.

Roda, A., Michelini, E., Zangheri, M., Di Fusco, M., Calabria, D., & Simoni, P. (2016). Smartphone-based biosensors: A critical review and perspectives. *TrAC Trends in Analytical Chemistry*, *79*, 317–325.

Sader, E., & Sayyed-Ahmad, A. (2013). Design of an optical water pollution sensor using a single-layer guided-mode resonance filter. *Photonic Sensors*, *3*(3), 224–230.

Savoia, S., Ricciardi, A., Crescitelli, A., Granata, C., Esposito, E., Galdi, V., & Cusano, A. (2013). Surface sensitivity of Rayleigh anomalies in metallic nanogratings. *Optics Express*, *21*(20), 23531–23542.

Sharon, A., Rosenblatt, D., & Friesem, A. A. (1997). Resonant grating–waveguide structures for visible and near-infrared radiation. *JOSA A*, *14*(11), 2985–2993.

Somarapalli, M., Jolivot, R., & Mohammed, W. (2018). Realization of Low-Cost Multichannel Surface Plasmon Resonance Based Optical Transducer. *Photonic Sensors*, *8*(4), 289–302.

Steele, J. M., Moran, C. E., Lee, A., Aguirre, C. M., & Halas, N. J. (2003). Metallodielectric gratings with subwavelength slots: Optical properties. *Physical Review B*, *68*(20), 205103.

Strutt, J. W. (1907). On the dynamical theory of gratings. *Proceedings of the Royal Society of London. Series A, Containing Papers of a Mathematical and Physical Character*, *79*(532), 399–416.

Su, Y., Geng, Z., Fan, Z., Wang, S., Lv, X., Fang, W., Pei, W., & Chen, H. (2019). Exploring surface sensitivity of Rayleigh anomaly in metal/dielectric multilayer gratings. *Optics Express*, *27*(10), 14152–14162.

Tabassum, S., Kumar, R., & Dong, L. (2017). Nanopatterned optical fiber tip for guided mode resonance and application to gas sensing. *IEEE Sensors Journal*, *17*(22), 7262–7272.

Wang, L., Sang, T., Li, J., Zhou, J., Wang, B., & Wang, Y. (2018). High-sensitive transmission type of gas sensor based on guided-mode resonance in coupled gratings. *Journal of Modern Optics*, *65*(13), 1601–1608.

Wang, Q., Zhang, D., Yang, H., Tao, C., Huang, Y., Zhuang, S., & Mei, T. (2012). Sensitivity of a label-free guided-mode resonant optical biosensor with different modes. *Sensors*, *12*(7), 9791–9799.

Wang, S. S., & Magnusson, R. (1993a). Theory and applications of guided-mode resonance filters. *Applied Optics*, *32*(14), 2606–2613.

Wang, S. S., Magnusson, R., Bagby, J. S., & Moharam, M. G. (1990). Guided-mode resonances in planar dielectric-layer diffraction gratings. *JOSA A*, *7*(8), 1470–1474.

Wang, Y.-C., & Huang, C.-S. (2018). Flexible linear and angular displacement sensor based on a gradient guided-mode resonance filter. *IEEE Sensors Journal*, *18*(24), 9925–9930.

Wawro, D. D., Tibuleac, S., Magnusson, R., & Liu, H. (2000). Optical fiber endface biosensor based on resonances in dielectric waveguide gratings. *Biomedical Diagnostic, Guidance, and Surgical-Assist Systems Ii*, *3911*, 86–94.

Wei, C., Liu, S., Deng, D., Shen, J., Shao, J., & Fan, Z. (2006). Electric field enhancement in guided-mode resonance filters. *Optics Letters, 31*(9), 1223–1225.

Wilkes, T. C., McGonigle, A. J., Pering, T. D., Taggart, A. J., White, B. S., Bryant, R. G., & Willmott, J. R. (2016). Ultraviolet imaging with low cost smartphone sensors: Development and application of a raspberry Pi-based UV camera. *Sensors, 16*(10), 1649.

Wilkes, T. C., McGonigle, A. J., Willmott, J. R., Pering, T. D., & Cook, J. M. (2017). Low-cost 3D printed 1 nm resolution smartphone sensor-based spectrometer: Instrument design and application in ultraviolet spectroscopy. *Optics Letters, 42*(21), 4323–4326.

Wood, R. W. (1902). XLII. On a remarkable case of uneven distribution of light in a diffraction grating spectrum. *The London, Edinburgh, and Dublin Philosophical Magazine and Journal of Science, 4*(21), 396–402.

Wood, R. W. (1912). XXVII. Diffraction gratings with controlled groove form and abnormal distribution of intensity. *The London, Edinburgh, and Dublin Philosophical Magazine and Journal of Science, 23*(134), 310–317.

Yariv, A. (1997). *Optical electronics in modern communications* (Vol. 1). Oxford University Press, USA.

Yariv, A., & Yeh, P. (1984). *Optical waves in crystals* (Vol. 5). Wiley New York.

Zhang, D., & Liu, Q. (2016). Biosensors and bioelectronics on smartphone for portable biochemical detection. *Biosensors and Bioelectronics, 75*, 273–284.

Zhang, W., Ganesh, N., Block, I. D., & Cunningham, B. T. (2008). High sensitivity photonic crystal biosensor incorporating nanorod structures for enhanced surface area. *Sensors and Actuators B: Chemical*, *131*(1), 279–284.

Zheng, G., Cong, J., Xu, L., & Su, W. (2014). Angle-insensitive and narrow band grating filter with a gradient-index layer. *Optics Letters*, *39*(20), 5929–5932.

Zhou, Y., Wang, B., Guo, Z., & Wu, X. (2019). Guided Mode Resonance Sensors with Optimized Figure of Merit. *Nanomaterials*, *9*(6), 837.

BIODATA

Name – Last name:	Hironmay Deb
Address:	Flat No: 2D, Pink House Apartment, A. K Azad Road, Rehabari, District- Kamrup (M), Assam, India, 781008.
Email:	deb.hironmay@gmail.com
Contact number:	+917896892766
Educational Background	Master of Technology in Optoelectronics and Optical Communication Department of Electronics and Communication Engineering, 2014 Assam Don Bosco University, Assam, India, 781017 Bachelor of Technology Department of Electrical and Electronics Engineering, 2008 Sikkim Manipal Institute of Technology, Sikkim Manipal University, Majitar, Rangpo, Sikkim-737136

Bangkok University

License Agreement of Dissertation/Thesis/ Report of Senior Project

Day__21__Month ___07__Year __2021_

Mr. Hironmay_ Deb now living at __Guwahati, Assam___

Soi Ward No 14 Street __A. K Azad

Sub-district Rehabari District __Kamrup (M)__

Province Assam Postal Code __781008__

being a Bangkok University student, student ID __9590900040

Degree level ☐ Bachelor ☐ Master ☑ Doctorate

Program Doctor of Engineering_ Department Electrical and Computer Engineering

School Graduate School hereafter referred to as "the licensor"

Bangkok University 119 Rama 4 Road, Klong-Toey, Bangkok 10110 hereafter referred to as "the licensee"

Both parties have agreed on the following terms and conditions:

1. The licensor certifies that he/she is the author and possesses the exclusive rights of dissertation/thesis/report of senior project entitled Guided Mode Resonance Based Spectroscopy for Sensing Applications submitted in partial fulfillment of the requirement for Doctor of Engineering in Electrical and Computer Engineering of Bangkok University (hereafter referred to as "dissertation/thesis/ report of senior project").
2. The licensor grants to the licensee an indefinite and royalty free license of his/her dissertation/thesis/report of senior project to reproduce, adapt, distribute, rent out the original or copy of the manuscript.
3. In case of any dispute in the copyright of the dissertation/thesis/report of senior project between the licensor and others, or between the licensee and others, or any other inconveniences in regard to the copyright that prevent the licensee from

reproducing, adapting or distributing the manuscript, the licensor agrees to indemnify the licensee against any damage incurred.

This agreement is prepared in duplicate identical wording for two copies. Both parties have read and fully understand its contents and agree to comply with the above terms and conditions. Each party shall retain one signed copy of the agreement.

_____ Licensor

(Hironmay Deb)

_____ Licensee

(Director, Library and Learning Center)

_____ Witness

(Dean, School of Engineering)

_____ Witness

(Program Director)